

# NUMERICAL MODELING OF FLUIDIZED BED

by

Hongbo Shi

A thesis submitted in partial fulfillment of the requirements for the degree of

**Master of Science**

Department of Mechanical Engineering  
University of Alberta

© Hongbo Shi, 2017

## Abstract

This work focuses on validation of a commercial computational fluid dynamics (CFD) software ANSYS Fluent 16.2 applied to multi-phase modeling of fluidized beds. A two-phase Eulerian-Eulerian based model is used to numerically reproduce experiments carried out by Taghipour, F. et al (Chem. Eng. Sci., 60(24), 2005, 6857-6867). The influence of the model dimension (2D & 3D), flow regimes models (laminar & turbulent), model parameters (specularity coefficient responsible for particle-wall interaction and restitution coefficient characterizing particle-particle interaction) and computational grids were investigated. The Syamlal-O'Brien and Gidaspow gas-solid drag submodels were tested. The comparison of numerical and experiment data showed that 2D simulations overpredict experimental data. 3D simulations showed good agreement between numerical calculations and experimentally measured void fraction profiles inside the bed. Results of 2D and 3D simulations revealed that the turbulence has a minor influence on the fluidized bed structure. However, it significantly affects the gas phase velocity in the upstream region of a reactor. At the same time, it was shown that a combination of E-E model parameters such as the specularity coefficient, numerical grid resolution and discretisation scheme for convective terms can lead to a good agreement between 2D CFD simulations and experimental data.

Additionally, the influence of heterogeneous reactions has been studied between gas phase and solid phase inside a fluidized bed using E-E model. It was shown that heterogeneous chemical reactions have significant impact on the fluidization regimes due to local increase in the gas flow rate. This effect should be taken into account by design of chemical reactors with heterogeneous chemical reactions, e.g. fluidized bed combustors, boilers and gasifiers.

## Acknowledgements

I would like to take this opportunity to express my gratitude to all the people who gave great help for my master studies in Department of Mechanical, and Chemical and Materials at University of Alberta.

Firstly, I would like to give my most sincere gratitude and appreciation to my two co-supervisors, **Dr. Petr A. Nikrityuk** and **Dr. Alexandra Komrakova** who gave me numerous kind and patient help not only on the academic and research areas, but also on my personal life and career development. Without their unconditional support and great guidance during the study and research period, I could not complete my master's degree. I will not forget the knowledge they taught me, the skills they helped me to develop the professional ethics and the enthusiasm of scientific researches they delivered. All of these will give me great help for my life and career as a mechanical science engineer.

Then, I would like to thank to Hemant Bansal and Philip Rößger for giving me valuable suggestions and assistance on the simulation validation and data analysis. Without their effort on my research, my work could not be smoothly proceeded.

Last but not least, I would like to express my deepest gratitude and appreciation to my parents, Fuqiang Shi and Jinying Yuan for their constant love, support and encouragement over the years.

# Table of Contents

<b>Abstract</b>	<b>ii</b>
<b>Acknowledgments</b>	<b>iii</b>
<b>1 Fluidized and Spouted Beds Gasifiers</b>	<b>1</b>
1.1 Introduction . . . . .	1
<b>2 Fluidized Bed Modeling: CFD Software Validation</b>	<b>11</b>
2.1 Modeling . . . . .	11
2.2 Benchmark-Experiments . . . . .	12
2.3 Model Formulation . . . . .	24
2.4 Results: Validation . . . . .	29
2.5 Minimum Fluidization Velocity . . . . .	47
2.6 Classification of Fluidization Regimes . . . . .	53
2.7 Conclusions . . . . .	54
<b>3 The Impact of Heterogeneous Reactions on Fluidized Bed Regimes</b>	<b>56</b>
3.1 Benchmark Experiments . . . . .	56
3.2 Model Formulation . . . . .	62
3.3 Results: The Influence of the Temperature on the Fluidized Bed Dynamics . . . . .	65
3.4 Conclusions . . . . .	74
<b>4 Conclusions and Future Work</b>	<b>75</b>
4.1 Conclusions . . . . .	75
4.2 Future Work . . . . .	76

# List of Tables

1.1	Characteristics of Fluid-bed process, adapted from [1], [2] . . . . .	3
2.1	Summary of literature works: $\Delta x/d$ , $\Delta y/d$ , and $\Delta z/d$ represent the number of particles in one grid; E-E = Eulerian-Eulerian; E-L = Eulerian-Lagrangian; E-L-S = Eulerian-Lagrangian-stochastic; E-L-D = Eulerian-Lagrangian-deterministic; E-E-E = Eulerian-Eulerian-Eulerian . . . . .	13
2.2	List of different grid resolutions used in simulations of fluidized beds.	26
2.3	Model equations available by ANSYS Fluent 16.2 which were used to model the fluidized bed from[3],[4]. . . . .	28
2.4	List of different models and schemes used in simulations of fluidized beds. . . . .	29
2.5	Correspondence of packing structure and voidage, adapted from [5] .	47
2.6	The relation between superficial gas velocity, $U$ and minimum fluidization velocity, $U_{mf}$ . . . . .	54
3.1	Simulation setups for gasification case . . . . .	62
3.2	Model equations available by ANSYS Fluent 16.2 which were used to model the fluidized bed from[3],[4]. . . . .	64

# List of Figures

1.1	Winkler atmospheric fluid-bed gasifier, adapted from [1] . . . . .	4
1.2	HTW Gasifier, adapted from [1] . . . . .	5
1.3	Gasification and dry section of HRL's process, adapted from [1] . . .	6
1.4	Lurgi circulating fluid-bed gasifier, adapted from [1] . . . . .	7
1.5	KBR transport gasifier, adapted from [6] . . . . .	8
1.6	U-Gas Gasifier, adapted from [1] . . . . .	9
2.1	Schematic of a spouted bed reactor, adapted from [7] . . . . .	14
2.2	Schematic of a fluidized bed reactor, adapted from [8] . . . . .	16
2.3	Schematic of a spout-fluid bed, adapted from [9] . . . . .	19
2.4	Schematic of a circulating fluidized bed riser, adapted from [10] . . .	20
2.5	Schematic of a interanlly circulating fluidized bed riser, adapted from [11] . . . . .	21
2.6	Schematic of a spout-fluid bed, adapted from [12] . . . . .	23
2.7	Schematic of a fluidized bed reactor, adapted from [8] . . . . .	24
2.8	Volume averaged solid velocity ( $U_s$ ) as a function of time for RANS models: drag function: Syamlal–O'Brien; Inlet Velocity: $U=0.38\text{m/s}$ ; Restitution coefficient: $e_{ss}=0.9$ . . . . .	30
2.9	3D-RANS: Simulated (a) solid volume fraction and (b) turbulent vis- cosity ratio: drag function: Syamlal–O'Brien; Inlet Velocity: $U=0.38\text{m/s}$ ; Specularity coefficient: $K=0.1$ ; Restitution coefficient: $e_{ss}=0.9$ . . . .	31
2.10	3D-RANS: Experimental[8] and simulated time-averaged void (gas phase) fraction profiles at $z = 0.2\text{m}$ calculated for $U = 0.38\text{m/s}$ . . .	32
2.11	2D: Solid volume fraction calculated using unsteady (a) Laminar and (b) RANS E-E model, Grid 1: $U = 0.38\text{m/s}$ , $K=0.1$ , $e_{ss}=0.9$ . . . .	34
2.12	2D: Solid volume fraction calculated using unsteady (a) Laminar and (b) RANS E-E model, Grid 2: $U = 0.38\text{m/s}$ , $K=0.1$ , $e_{ss}=0.9$ . . . .	35

2.13	2D-RANS: Turbulent viscosity ratio $\frac{\mu_t}{\mu_0}$ at $t = 1, 2.2, 9,$ and $16s$ : drag function: Syamlal O'Brien; Inlet Velocity: $U_{in} = 0.38m/s$ ; Specularity coefficient: $K = 0.1$ ; Restitution coefficient $e_{ss} = 0.9$ . (a) Grid 1 and (b) Grid 2. . . . .	36
2.14	2D-RANS: Time-averaged solid volume fraction: drag function: Syamlal O'Brien; Inlet Velocity: $U_{in} = 0.38m/s$ ; Specularity coefficient: $K = 0.1$ ; Restitution coefficient $e_{ss} = 0.9$ . (a) Laminar model-Grid 1, (b) RANS model-Grid 1, (c) Laminar model-Grid 2, (d) RANS model-Grid 2. . . . .	37
2.15	2D: Experimental[8] and simulated time-averaged void fraction profiles at $z = 0.2m$ for 2D, $U = 0.38m/s$ , $K = 0.1$ , $e_{ss} = 0.90$ , (a) Grid 1, (b) Grid 2. . . . .	39
2.16	2D: Experimental[8] and simulated time-averaged void fraction profiles at $z = 0.2m$ predicted for different specularity coefficients on RANS models: (S-O) $U = 0.38m/s$ , $e_{ss} = 0.90$ . . . . .	40
2.17	3D-RANS: Experimental and simulated time-averaged void (gas phase) fraction profiles at $z = 0.2m$ calculated for $U = 0.38m/s$ : (S-O) $K = 0.1$ . . . . .	41
2.18	3D-RANS: Experimental[8] and simulated time-averaged void (gas phase) fraction profiles at $z = 0.2m$ calculated for $U = 0.46m/s$ : (S-O) $e_{ss} = 0.90$ . . . . .	41
2.19	Volume averaged solid velocity ( $U_s$ ) as a function of time for 3D RANS models: Drag function: Syamlal-O'Brien; Restitution coefficient: $e_{ss}=0.9$ . . . . .	42
2.20	Volume averaged solid velocity ( $U_s$ ) as a function of time for 2D RANS models: $e_{ss}=0.9$ , (a) Grid 1, $U = 0.38m/s$ , (b) Grid 2 . . . . .	43
2.21	Simulation errors for 3D and 2D models at $U = 0.38m/s$ . . . . .	45
2.22	Simulation errors for 3D and 2D models at $U = 0.46m/s$ . . . . .	46
2.23	Volume averaged solid velocity as a function of time for (a) 2D-Grid 1 and (b) 3D models: (S-O) $K = 0.1$ , $e_{ss} = 0.90$ . . . . .	49
2.24	2D-RANS : Solid volume fraction calculated using unsteady E-E model: $K=0.1$ , $e_{ss}=0.9$ : (a1) $U=0.2m/s$ , $t=1.425s$ (a2) $U=0.2m/s$ , $t=7.8s$ (a3) $U=0.2m/s$ , $t=8.75s$ (b1) $U=0.15m/s$ , $t=1.45s$ (b2) $U=0.15m/s$ , $t=7.6s$ (b3) $U=0.15m/s$ , $t=8.45s$ (c1) $U=0.125m/s$ , $t=1.65s$ (c2) $U=0.125m/s$ , $t=7.8s$ (c3) $U=0.125m/s$ , $t=8.85s$ . . . . .	51

2.25	3D-RANS , Solid volume fraction calculated using unsteady E-E model: $K=0.1, e_{ss}=0.9$ : (a1) $U=0.2\text{m/s}, t=1.35\text{s}$ (a2) $U=0.2\text{m/s}, t=7.2\text{s}$ (a3) $U=0.2\text{m/s}, t=7.5\text{s}$ (b1) $U=0.15\text{m/s}, t=1.1\text{s}$ (b2) $U=0.15\text{m/s},$ $t=6.9\text{s}$ (b3) $U=0.15\text{m/s}, t=7.35\text{s}$ (c1) $U=0.125\text{m/s}, t=1.4\text{s}$ (c2) $U=0.125\text{m/s},$ $t=5.05\text{s}$ (c3) $U=0.125\text{m/s}, t=7.6\text{s}$ . . . . .	52
2.26	Snapshots of solid volume fraction in different regimes at $t=20$ s, $K = 0.1, e_{ss} = 0.8$ : (a) Minimum fluidization (b) Bubbling bed (c) Turbulent bed . . . . .	54
3.1	Schematic of a pressurized spout-fluid bed, adapted from [13] . . . . .	57
3.2	Schematic of a bubbling fluidized bed, adapted from [14] . . . . .	59
3.3	Schematic of a spout-fluid Bed, adapted from [15] . . . . .	61
3.4	2D-RANS: Solid volume fraction calculated using unsteady E-E model at different inflow velocities $U$ : Grid 1, (S-O), $K=0.1, e_{ss}=0.9$ , (a) Cold case, $t=20$ s, (b) Gasification case, $T=1100$ K, $t=20$ s, (c) Gasi- fication case, $T=1500$ K, $t=40$ s. . . . .	68
3.5	2D-RANS: Time averaged solid volume fraction calculated using un- steady E-E model at different inflow velocities $U$ : Grid 1, (S-O), $K=0.1, e_{ss}=0.9$ , (a) Cold case, (b) Gasification case, $T=1100$ K (c) Gasification case, $T=1500$ K . . . . .	69
3.6	2D-RANS: Time-averaged gas velocity vector calculated using un- steady E-E model at different inflow velocities $U$ : Grid 1, (S-O), $K=0.1, e_{ss}=0.9$ , (a) Cold case (b) Gasification case, $T=1100$ K (c) Gasification case, $T=1500$ K . . . . .	70
3.7	2D-RANS: Mass fraction of $CO$ calculated using unsteady E-E model at different inflow velocities $U$ : Grid 1, (S-O), $K=0.1, e_{ss}=0.9$ , (a) $T=1100$ K, $t=20$ s, (b) $T=1500$ K, $t=40$ s. . . . .	71
3.8	2D-RANS: Mass fraction of $CO_2$ calculated using unsteady E-E model at different inflow velocities $U$ : Grid 1, (S-O), $K=0.1, e_{ss}=0.9$ , (a) $T=1100$ K, $t=20$ s, (b) $T=1500$ K, $t=40$ s. . . . .	72
3.9	2D-RANS: Time averaged temperature calculated using unsteady E-E model at different inflow velocities $U$ : Grid 1, (S-O), $K=0.1,$ $e_{ss}=0.9$ , (a) $T=1100$ K, (b) $T=1500$ K. . . . .	73

# List of Symbols

$A$	pre-exponential factor for kinetic energy
$C_D$	drag function
$d_s, d_p$	diameter of solid particle
$E_A$	activation energy
$e_{ss}$	coefficient of restitution
$g$	gravitational acceleration
$g_{0,ss}$	radial distribution function
$K$	specularity coefficient
$k_g$	turbulence quantities of gas phase
$k_s$	turbulence quantities of solid phase
$K_{pq}$	interphase momentum exchange coefficient
$K_{gs}$	interphase momentum exchange coefficient between gas and solid phase
$k_{kin}$	kinetic rate
$n_t$	temperature exponent
$p$	pressure shared by all phases
$p_s$	solid pressure
$\vec{R}_{pq}$	interaction force between phases
$Re_s$	Reynolds number for solid particles
RNG	renormalization group method
$U$	superficial gas velocity
$U_{mf}$	minimum fluidization velocity
$\bar{U}_g$	volume averaged velocity for gas phase
$V_q$	volume of phase q
$V_{sb}$	volume of the spouted bed reactor
$\vec{v}_q$	velocity of phase q
$v_g$	velocity of gas phase
$v_s$	velocity of solid phase

$v_q$  particle velocity fluctuation

### Greek letters

$\alpha_q$  volume fraction of q phase

$\alpha_{s,max}$  maximum packing limit

$\alpha_s$  volume fraction of solid phase

$\alpha_g$  volume fraction of gas phase

$\kappa - \varepsilon$  Kappa-epsilon turbulence model

$\rho_q$  physical density of phase q

$\rho_g$  physical density of phase g

$\hat{\rho}_q$  effective density of phase q

$\bar{\bar{\tau}}_q$   $q^{th}$  phase stress-strain tensor

$\lambda_q$  bulk viscosity of phase q

$\gamma_{\theta_s}$  collisional energy dissipation

$\phi_{gs}$  kinetic energy transfer

$\theta_s$  granular temperature

$\beta$  fluid-particle interaction coefficient

$\mu_s$  solid shear viscosity

$\mu_{s,col}$  solid collisional viscosity

$\mu_{s,kin}$  solid kinetic viscosity

$\mu_{s,fr}$  frictional viscosity

$\mu_g$  viscosity of gas phase

$\phi_s$  volume fraction of solid phase

$\Theta_q$  granular temperature

$\mu_{t,g}$  turbulent viscosity

$\varepsilon_g$  turbulence dissipation rate of gas phase

$\sigma_k, \sigma_z$  adjustable constants

$\Pi_{k,g}, \Pi_{z,g}$  influence of dispersed phases on continuous phase

$\sigma_{est}$  standard error of the estimate

$\varepsilon$	voidage
$\varepsilon_{mf}$	voidage at the minimum fluidization

### **Subscripts**

$g$	gas phase
$p$	particle
$s$	solid phase

# Chapter 1

## Fluidized and Spouted Beds Gasifiers

### 1.1 Introduction

Nowadays, there is significant attention to the high level pollution and low efficiency of traditional fuel combustion. Gasification, as one of the clean fuel technologies, has been studied to tackle the gaseous pollution emission and low efficiency problems. In the gasification process, the solid carbonaceous materials (coal, biomass, or wastes) convert into a combustible or synthesis gas that provides the potential for chemical production and clean power [16]. Both combustion and gasification of coal have similar physical and chemical processes, but the pollutant formation are different. For combustion process, large quantity of sulfur is converted to  $SO_2$ , and  $N_2$  is converted to  $NO$ . Most  $SO_2$  and  $NO$  are released into air causing acid precipitation problem. However, most of sulfur reacts to form  $H_2S$ , and  $N_2$  reacts to form  $NH_3$  in the gasification process [17]. The produced harmful gas ( $H_2S$  and  $NH_3$ ) can be collected and removed from the gasifier easily. Consequently, the gasification technology produce more clean energy than the traditional combustion.

Moving-bed gasifiers, fluid-bed gasifiers and entrained-flow gasifiers are the three basic categories of gasification [1]. Fluid-bed gasifiers have been paid increasing attention over the last 20 years due to the advantages of intensely mixing feed and oxidant, high efficiency of heat and mass transfer, and the uniform and moderate operating reactor temperature [1]. In the fluid-bed gasifier, the coal with particle diameter ( $d_p$ )  $< 3mm$  is supplied as a powder feed. The gasifying agent maintains the coal in a suspended state with the continuous random motion [17]. As long as the coal is supplied into the gasifier, the temperature of the coal increases signif-

icantly to the operation reactor temperature which generally is less than  $1050^{\circ}C$  [18]. Consequently, the heated coal reacts with an oxidizer (air, oxygen, steam, or carbon dioxide) to produce a fuel-rich gaseous product (carbon monoxide, hydrogen, or methane) [19]. The products can be directly used as synthesis gas for production of gasoline, or as gaseous fuel for production of industrial steam, heat or electrical power [19].

There are many parameters that determine the hydrodynamic characteristics of the gas-solid flow in a fluidized bed gasifier, including superficial gas velocity, gas-solid drag force, specularity and restitution coefficients, and frictional viscosity. The superficial gas velocity represents the inlet velocity of gas through a packed bed in the gasifier. The fluid regime can be changed with the increase of upward superficial gas velocity from zero to the point of fluidization (upward drag force exceeds the downward body force of gravity) and further. The gas-solid drag force is the resistance force caused by the motion of a particle through a fluid [3]. The drag submodel is the main reason contributing the high bed expansion and intensified mixing between particles and gas. Both specularity coefficient which is responsible for particle-wall interaction and restitution coefficient responsible for particle-particle interaction, play an important role in the bed behavior. A value of zero represents the inelastic collision and the value of unity relates the perfect elastic collision between particle-wall or particle-particle [20] [21]. After collision between the particle and particle, the stress is generated due to the enduring contact and momentum transfer through friction between particles which is called as frictional viscosity [22].

The fluid-bed gasifiers provide competitive advantages at gasification processes. However, some common issues follow the advancement of the technology. Operating reactor temperature is the most significant issue in the gasification process. If the temperature is higher than  $1050^{\circ}C$ , the individual particles in the bed will begin to aggregate together due to the intensified particle softening [1]. Consequently, the high quantity of reformed particles precipitate at the bottom of the bed decreasing the efficiency of production. Based on this reason, the operating temperature in the fluidized bed gasifier is restricted below the softening point of the ash. If the operating temperature is too low, substantial proportion of hydrocarbons will be formed in the produced synthesis gas [1].

Feed quality is another considerable challenge. In the fluid-bed processes, low-rank coals (lignite, peat or biomass, etc.) are favorable feedstocks due to their high reactivity and non-cracking character [17]. The coal particle size ( $d_p$ ) is restricted to the range [0.5-3] mm. For  $d_p < 0.5mm$ , particles are easily entrained in the

synthesis gas and block the system, while large particles ( $d_p > 3mm$ ) might deposit in the bed resulting in the defluidization [1]. Moreover, low carbon conversion is the common phenomenon in the existing fluid-bed gasifiers. The highest value of carbon conversion in the fluid-bed processes is 97%, while both moving-bed and entrained-flow bed can reach 99% in the process [23]. Low carbon conversion leads the lower rate of gas production and the high carbon content in the discharged ash. The discharged ash might contain unconverted lime since limestone is added to react with sulfur in the gas [1]. These situations should be avoided from the disposal of ash.

The fluid-bed gasification process can be divided into two main categories in accordance with the solid residue conditions - Dry ash and agglomerating types (see Table 1.1). The first category includes Winkler process, High-Temperature Winkler (HTW) process, HRL process, Bharat Heavy Electricals Limited (BHEL) gasifier, Circulating fluidized-bed (CFB) process and Kellogg Brown and Root (KBR) transport gasifier. Another category consists of Kellogg Rust Westinghous (KRW) process and U-Gas technology[1]. Each process or gasifier owns its particular characteristics and advantages.

Table 1.1: Characteristics of Fluid-bed process, adapted from [1], [2]

<b>Solid residue conditions</b>	Dry ash	Agglomerating
Typocal Processes	Winkler, HTW, KBR, CFB, HRL	KRW, U-Gas
<b>Feed characteristics</b>		
Particle diameter ( $d_p$ )	0.5 – 3 mm	0.5 – 3 mm
Accpetability of fines	Good	Better
Acceptability of caking coal	Possibly	Yes
Preferred coal rank	Low	Any
<b>Operating characteristics</b>		
Outlet gas temperature	900 – 1050°C	900 – 1050°C
Oxidant demand	0.4 – 0.7m <sup>3</sup> /kg	0.4 – 0.7m <sup>3</sup> /kg
Steam demand	0.2 – 0.6kg/kg	0.2 – 0.6kg/kg
Carbon conversion	80 – 95%	80 – 95%
Residence time	Minutes	Minutes
Specific capacity	Moderate/high	Moderate/high

The first modern continuous gasification process is the Winkler atmospheric fluid-bed process (see Fig.1.1). Instead of using air as blast, oxygen is taken in the Winkler process with the inlet velocity of 5m/s [1].There are two inlets of blast, one is located in the base and another one is above the bed surface. This design

can enhance the gasification of small coal particle and reduce the content of the hydrocarbons inside of the gaseous product [1]. Any fuel can be used in the Winkler process. However, brown coal, coke, sub-bituminous and bituminous coals are preferred in commercial plants [1]. The discharged ash containing over 20% amount of unreacted carbon will be burnt in an accessory boiler [24] (not shown in Fig.1.1).

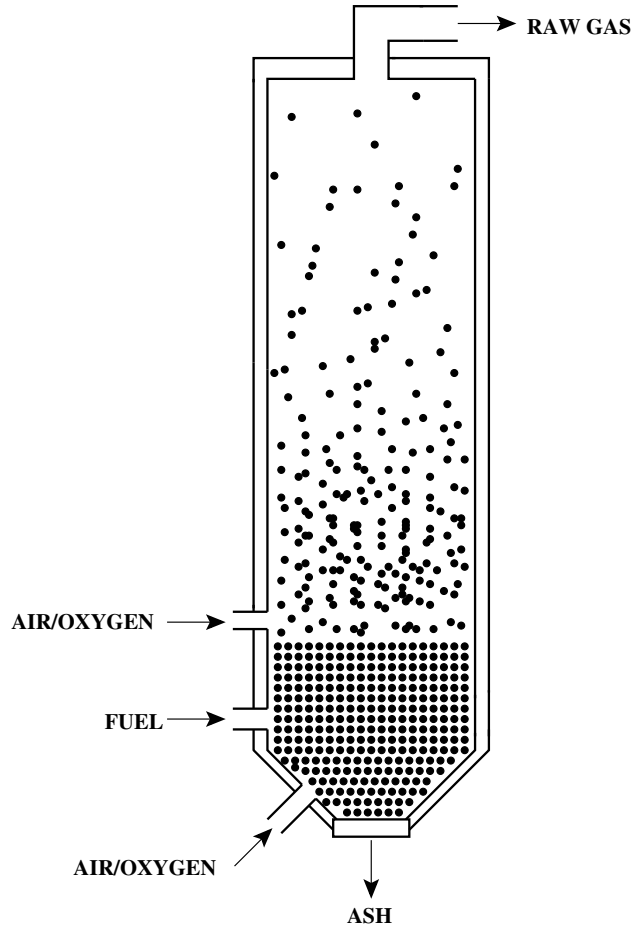


Figure 1.1: Winkler atmospheric fluid-bed gasifier, adapted from [1]

The High-Temperature Winkler (HTW) process for lignite gasification is developed based on the Winkler atmospheric fluid-bed process (see Fig.1.2). The most significant improvement of HTW process is the increase of operating pressure from the ambient pressure to 30 bar [1]. With the elevated pressure, the specific capacity can be improved resulting the better quality of the produced raw gas [25]. The unreacted particle can recycle from gas phase to the bed through a cyclone. Consequently the carbon conversion increases [26].

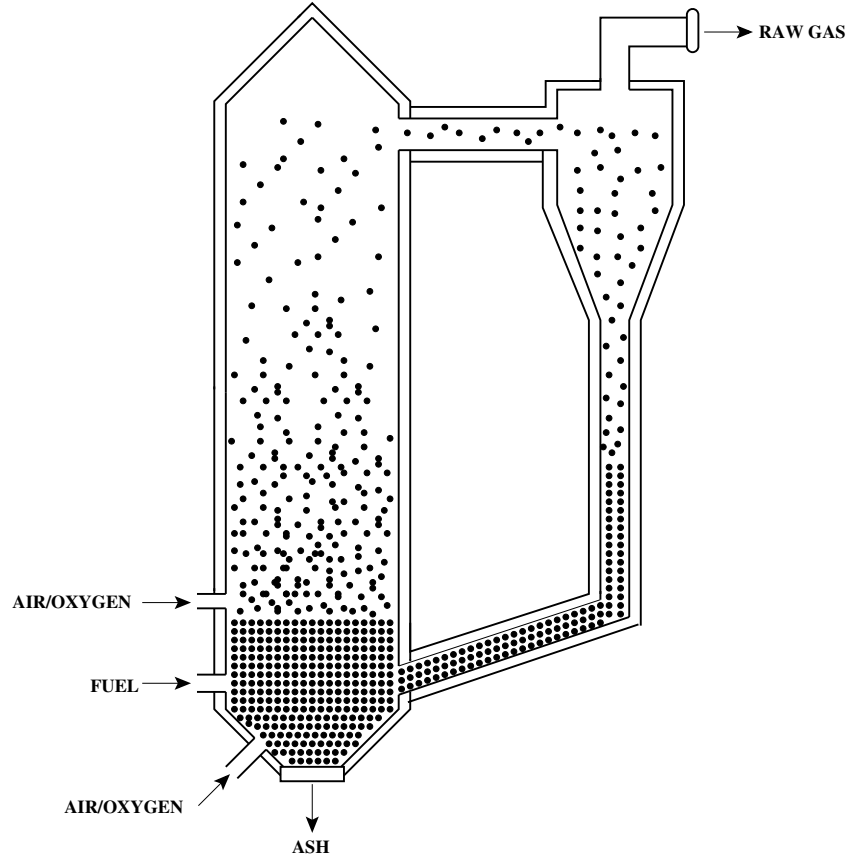


Figure 1.2: HTW Gasifier, adapted from [1]

HRL process (see Fig.1.3) is a special technology that uses moisture-rich ( $\leq 62wt\%(ar)$ ) brown coal [6]. The unique feature of this process is that the feed coal is dried by the sensible heat of hot syngas from an air-brown CFB gasifier [1]. The dried coal is supplied to the gasifier and reacts with gasification air to produce the syngas. Both operating temperature and pressure are similar to the HTW process ( $T_r = 900^\circ C$ ,  $P=30$  bar) [6]. The energy efficiency of this process is 38-41% (HHV) when Latrobe valley brown coal (moisture-rich) is used as a feed [1].

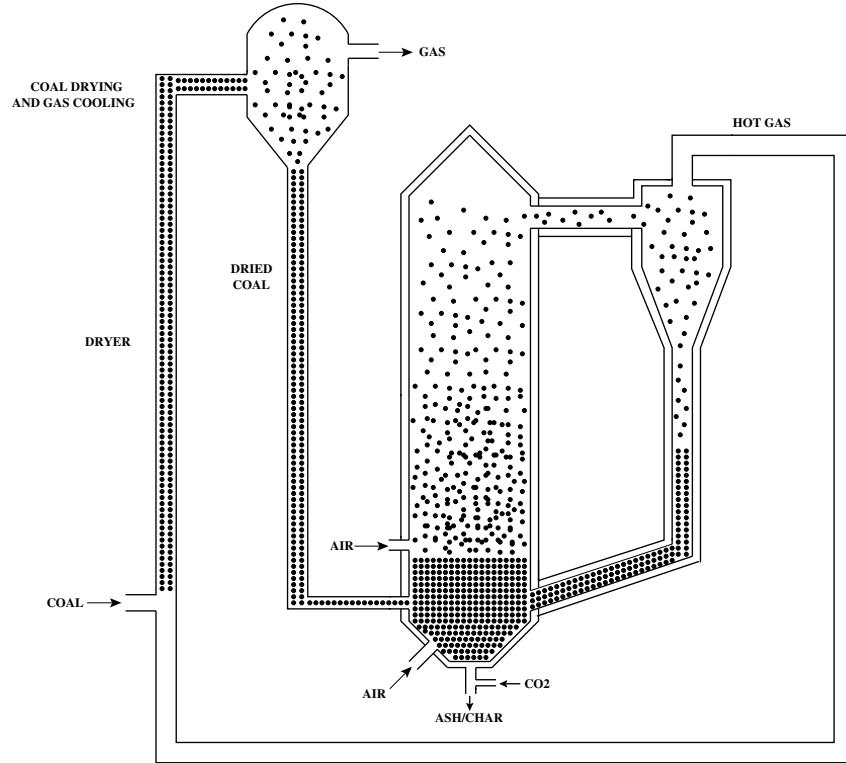


Figure 1.3: Gasification and dry section of HRL's process, adapted from [1]

Bharat Heavy Electricals Limited (BHEL) gasifier is a non-slugging system which is applied to high-ash (40wt%(dry)) coal reserves [6]. By using this gasifier, significant oxygen can be saved due to the high ash content coal [1]. BHEL developed a air-blown fluid-bed gasifier with Integrated Gasification Combined Cycle (IGCC) applications at Auraiy in Uttar Pradesh [1].

The circulating fluidized-bed (CFB) (see Fig.1.4) is the combination of the advantage of the stationary fluidized bed processes and the transport reactor gasification [6]. This bed has the slip velocity that is the largest differential velocity between gas and solids in the intermediate velocity regime [1]. Consequently, the mixing of gas and feed is enhanced and the advanced heat and mass transfer is promoted [1]. The requirement for the size of the particle is not strict in the CFB process. Fine particles are carried by the gasification agent to the cyclone and then returned through an external recycle. The heavier particles with low consumption rate are required to be recycled internally with high gas velocities (5-8m/s) first, and then switch to external recycle when the particles size small enough [1]. CFB gasifiers can use a wide range of fuels even low rank and waste coals at lower economical pricing [27]. The combustion efficiency of CFB gasifier can reach 99.5% resulting higher heating

rate from the feedstock and better particle-gas mixing [27]. The higher circulation rate and heat process of CFB gasifier decrease the formation of tar [1].

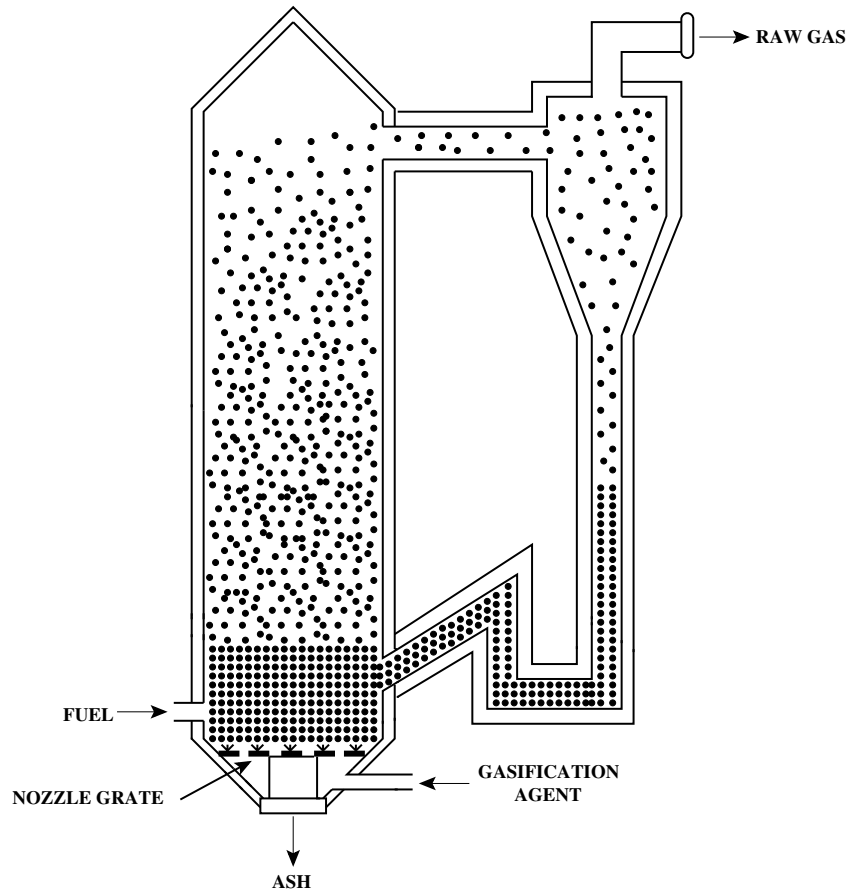


Figure 1.4: Lurgi circulating fluid-bed gasifier, adapted from [1]

The Kellogg Brown and Root (KBR) transport gasifier (see Fig.1.5) is developed based on the CFB gasifier. In contrast to the CFB gasifier, the KBR transport gasifier can contribute higher velocities ( $11-18m/s$ ), circulation rates, and increased densities of particles. Consequently, the mixing and heat transfer rate can be improved and the production of syngas increases [1]. In the KBR transport gasifier, the primary feedstock is low-rank coals with diameter of  $[250 - 600]\mu m$  [28]. Most gasification processes use air as feed since air-blown is used for power generation and the oxygen-blown is used for liquid fuels and chemicals [29]. The average carbon conversion rates are around 95% and the maximum value of 98% can be reached [1].

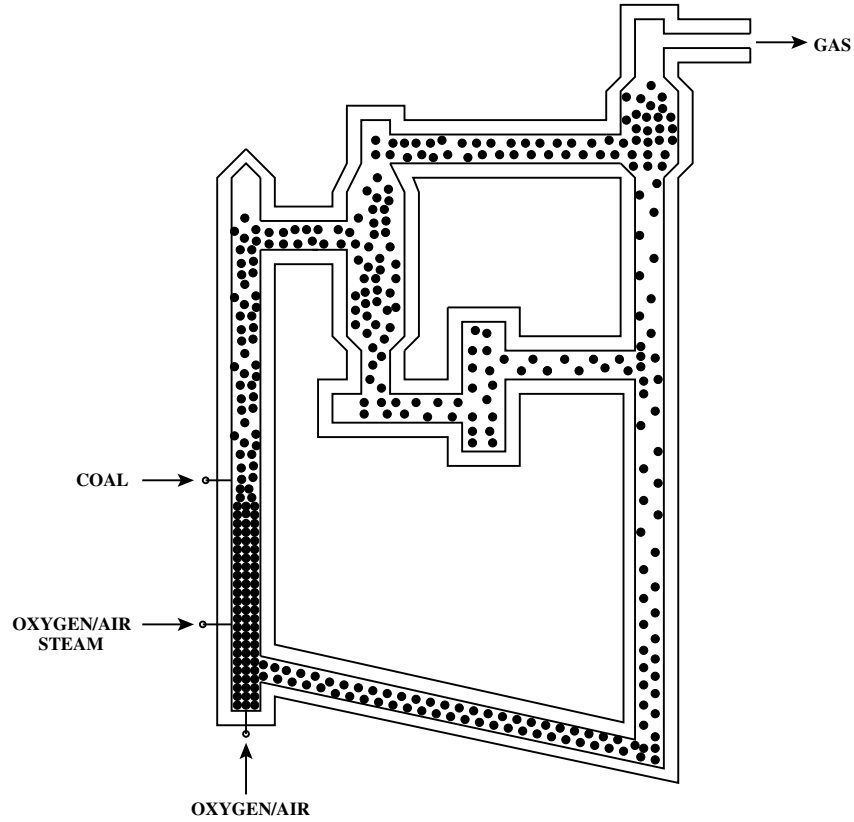


Figure 1.5: KBR transport gasifier, adapted from [6]

The agglomerating fluid-bed processes is designed based on the idea that ash start to fuse at its softening point in a high temperature regional area [1]. The objective of this development is to restrict the quality of agglomerate ash fall down to the bottom [1]. This process can achieve higher carbon conversion than conventional fluid-bed processes since fully separated low-carbon ash particles [1]. The Kellogg Rust Westinghouse (KRW) and the U-Gas technology are two gasifier developed from the agglomerating fluid-bed processes. The 100 MW(e) IGCC Clean coal Technology project cannot operate successful in USA due to the hot gas cleanup system issue [30]. The U-Gas technology (see Fig.1.6) developed by Gas Technology Institute (GTI) has been successfully applied in USA, China, and Europe [28]. The feedstocks of the U-gas gasifier are all rank coal and mixture of coal and biomass [29]. Both air and oxygen-blown can contribute high efficiency of production [29]. The U-gas technology attracts people's attention significantly since the capital construction costs for this gasifier are lower most other commercial gasifiers [28].

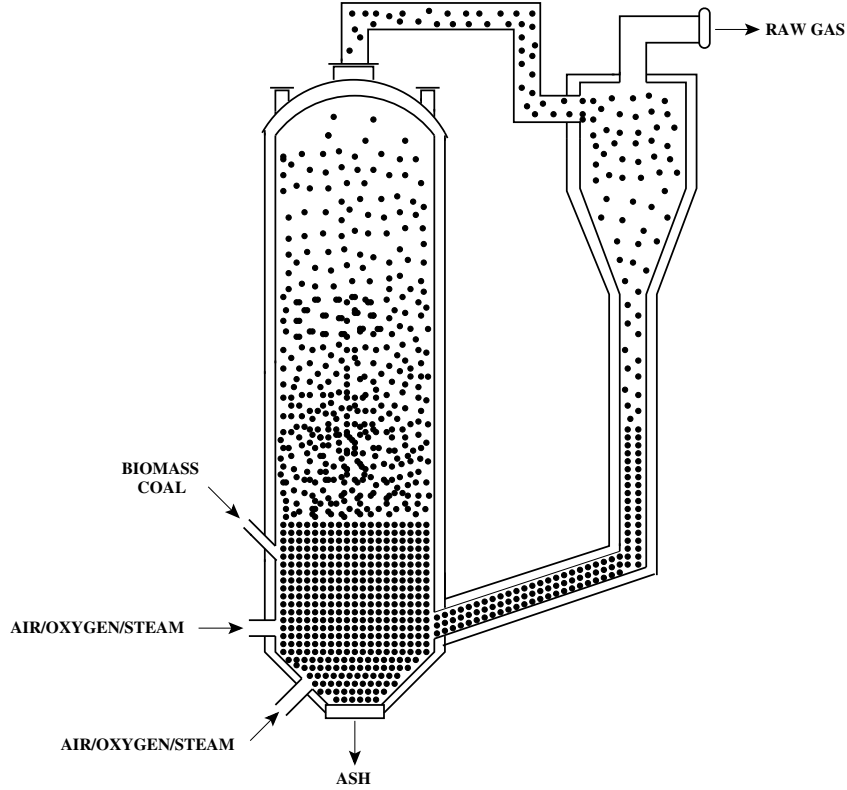


Figure 1.6: U-Gas Gasifier, adapted from [1]

Analysis of different types of fluidized beds and their applications in industry shows that the next challenging task for engineers is to increase the efficiency of fluidized beds. This can be done using computational fluid dynamics (CFD) based modeling of processes occurring inside fluidized beds. It should be emphasized that recently computer modeling became one of the most crucial elements in the design and optimization of novel technologies in the field of industrial engineering. One of the advantages of computer modeling is that the behavior and characteristics of the fluidized bed reactor may be investigated without actual fabricating a prototype. Thus, the total costs of product development can be reduced significantly. However, the numerical simulations of multiphase flows in fluidized beds often include complex physical and chemical phenomena which have to be modeled using advance mathematical models implemented into a CFD software. Recently, impressive development in commercial CFD software, e.g., ANSYS Fluent, ANSYS CFX, STAR-CCM+, Flow 3D, and in new multi-phase flow models made it possible to simulate 3D fluidized beds without oversimplifications.

The main goal of the present work is to sketch out the role of basic parameters used in Euler-Euler based multiphase model available in ANSYS Fluent to model

adequately fluidized beds. The illustrative experiments from the literature are used to validate the commercial software ANSYS Fluent. It should be noted that no attempt has been made in this work to explore all the aspects of fluidized-bed-fluid-mechanics.

## Chapter 2

# Fluidized Bed Modeling: CFD Software Validation

### 2.1 Modeling

Computational fluid dynamics (CFD) modeling is a powerful tool for design and optimization of gasification process, which is widely used in industry and academia. The most crucial issue for gasification process is the proper prediction of the fundamental characteristics of gasifiers, such as solids recycling pattern, operating temperature, and produced gas compositions, etc. Unfortunately, the experimental studies cannot predict such elementary features appropriately due to the complexity of the physical and chemical processes in the gasifiers. The CFD platform, which considers the numerical solution of mass, momentum, energy and chemical species conservation equations, is developed and applied to resolve such difficulties during the gasification processes [2]. The CFD-based models applied to simulations of fluidized bed can reveal the physical and chemical processes inside the gasifier with mathematical and numerical heat and mass transfer theories [2]. To guarantee adequacy and reliability of any model or software, verification and validation processes are required. Verification is the process of determining the accuracy of the numerical models in comparison with the exact solution based on the concepts and equations [31]. Validation addresses the comparison between numerical results with experiment data. Verification can be considered as the prerequisite for the validation but the reverse is wrong [31]. The good agreement between numerical results and experiment measurements can arouse the interest of industry and academia.

The numerical simulations are competitive over experiment studies. The dominant advantage of the numerical simulations is the less expense on modeling com-

pared to the experiments. In addition, the numerical simulations are able to show some processes that are difficult or impossible to implement in the experiments (e.g. heterogeneous reactions inside the gasifier) [2]. The numerical simulation can be used to control and optimize the parameters of the existing engineering solutions. Moreover, the numerical simulations are flexible to consider a wide range of engineering problems. On the other hand, some main challenges, such as multiscale character, coal kinetic reaction data, thorough particle models and blending feedstocks, have to be addressed by modeling development of gasification as well [2].

A good way to understand modeling and simulation is to look at the life cycle of the modelling process. There are five stages in this process. The first phase is the problem statement. The created and gathered information should be put together and analyzed. The second step is the development of a mathematical model of the stated engineering problem. The third step is the construction of an proper numerical model from the developed mathematical model. The fourth step is the solution of the numerical model. The final step is the verification and validation of the model and simulation [2]. The process of verification and validation is of significant importantly for the success if a simulation study.

## 2.2 Benchmark-Experiments

Eulerian-Eulerian (E-E) and Eulerian-Lagrangian (E-L) are the two main approaches used in CFD-based fluidized bed models. In E-E approach, the fluid and solid phase are considered as interpenetrating continuum phases, and both time and the volume position are independent variables [7]. The transport equations are used to write momentum and energy conversion. E-L approach treats the fluid phase as continuum and the solid particles as individual dispersed particles, and the only independent variable is time [7]. The Newton law of motion is applied in this approach.

Many researchers studied the characteristics of gas-solid fluidized bed reactor by applying the E-E and E-L models in the CFD software, ANSYS Fluent. Loha [20] [21] carried out a 2D E-E model to investigate the effect of coefficient of restitution and specularly coefficient. The influences of gas and solid properties was studied with a 3D E-L model by Luo [11]. A 3D E-L model developed by Link [9] was applied to investigate the impact of various flow regimes, computational grid resolution, and drag closure on the numerical prediction. Both E-E and E-L approaches were used by Almohammed [32] to study the effects of flow rate of the injected gas in a 3D model. Stroh [7] developed a 3D numerical model to investigate and compare three different numerical methods, including E-E, E-L-S (Eulerian-Lagrangian-stochastic),

and E-L-D(Eulerian-Lagrangian-deterministic).

Table 2.1: Summary of literature works:  $\Delta x/d$ ,  $\Delta y/d$ , and  $\Delta z/d$  represent the number of particles in one grid; E-E = Eulerian-Eulerian; E-L = Eulerian-Lagrangian; E-L-S = Eulerian-Lagrangian-stochastic; E-L-D = Eulerian-Lagrangian-deterministic; E-E-E = Eulerian-Eulerian-Eulerian

Authors	Model	$\Delta x/d, \Delta y/d, \Delta z/d$
Stroh et al. [7]	E-E, E-L-S, E-L-D	0.75, 0.93, 0.36
Almohammed et al.[32]	E-E, E-L	0.75, 1.85, 0.36
Cornelissen et al.[33]	E-E	0.94, 1.77
Ehsani et al.[34]	E-E	0.33, 0.33
Almuttahir et al.[35]	E-E	14.5, 229
Loha et al.[21]	E-E	3.66, 24.3
Bakshi et al. [36]	E-E	25.1, 17.3 8.30, 5.0 20.6, 17.3
hamidipour et al.[37]	E-E-E	1.67, 3.13 5.52, 6.79
Hua et al.[10]	E-E	65.5, 65.5, 453
Li et al. [38]	E-E	45.7, 94.1 11.4, 23.5 22.8, 47.1 10, 20 7.04, 14.1 5, 9.98
Luo et al.[11]	E-L	2.5, 2.8, 2.5
Luo et al.[39]	E-L	2.5, 2.8, 2.5
Muller et al.[40]	E-L	3.1, 0.3
Muller et al.[41]	E-L	3.1, 0.3
Nguyen et al.[42]	E-E	20, 20
Yang et al.[12]	E-L	1.82, 1.49, 24.8

The number of particles in each grid are important for different numerical CFD methods. E-E model requires at least two particle in one grid ( $\Delta x, \Delta y, \Delta z \geq 2d_p$ ). E-L (DPM) model requires at least 3 particle in one grid ( $\Delta x, \Delta y, \Delta z \geq 3d_p$ ). Table 2.1 shows the total number of particles in each grid for several works. Based on the calculations, there are some works do not reach the requirement from E-E or E-L, which are indicated with red color [7],[32],[33], [34]. The numerical results from these works are far away from reality. The Syamlal -O'Brien and Gidaspow drag forces cannot be applied in models due to less quantity of particles ( $< 10$ ) in each cell.

Stroh [7] studied and compared three different numerical methods, Euler-Euler

(E-E), Euler-Lagrange-stochastic (E-L-S), and Euler-Lagrange-deterministic (E-L-D), to replicate an experiment of a spouted bed reactor (see Fig.2.1). All three approaches can predict the bubble development for inlet air mass flow rates of 0.005 and 0.006  $kg/s$ . The numerical results are in good agreement for the mass flow rate of 0.005  $kg/s$ . The largest deviation of of bed height and equivalent bubble diameter between experiment data and numerical predictions are 12% and 10% for the inlet mass flow rate of 0.005  $kg/s$ . Whereas a higher deviations, 30% and 42%, are obtained for 0.006  $kg/s$ . More accurate modeling of collisional and frictional forces improve prediction of the flow patterns by E-E and E-L-D approaches.

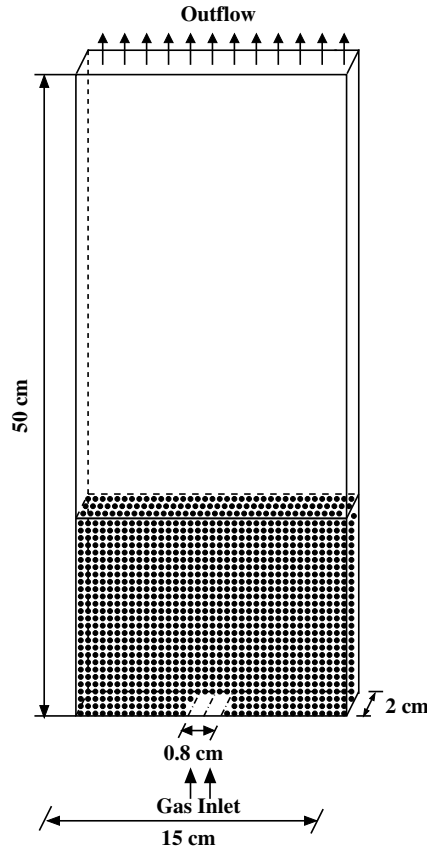


Figure 2.1: Schematic of a spouted bed reactor, adapted from [7]

Almohammed [32] studied the hydrodynamics of gas-solid flows in a 3D spouted fluidized bed with E-E and E-L approaches. The main purpose was to investigate the influence of the injected gas flow rate on the numerical results. From the numerical predictions, the Syamlal-O'Brien drag submodel is suitable to predict flow pattern in the bed. The particle-particle restitution coefficient of 0.6 and specularity coefficient of 0.5 gives the best agreement between numerical results and experimental

data. The algebraic granular temperature submodel is more suitable than partial differential submodel on both mass flow rates (0.005 and 0.006  $kg/s$ ) since this model contribute less deviation on bed height and equivalent bubble diameter and lower computational effort is required. The E-E approach can successfully predict the flow pattern at a mass flow rate of 0.005  $kg/s$ , while large deviation is produced as the flow rate increases from 0.005  $kg/s$  to 0.006  $kg/s$ . For E-L approach, perfect prediction of bed expansion and bubble formation can be obtained on both mass flow rates.

Taghipour [8] used the E-E model to simulate a two-dimensional gas-solid flow in a fluidized bed reactor (see Fig.2.2). The simulation results were compared to an experiment, where 250-300  $\mu m$  diameter spherical glass beads were used in a fluidized bed. Syamlal -O'Brien [43], Gidaspow [44], and Wen-Yu [45] drag functions were used to calculate momentum exchange coefficients. The restitution coefficient values that varied from 0.9 to 0.99, were used to characterize the solid-phase kinetic energy fluctuation. The CFD predictions of bed expansion ratio, qualitative gas-solid flow pattern, instantaneous and time-average local voidage profiles were in line with experiment measurements. The estimated time-averaged bed pressure drops (from 6000 kPa to 4600 Kpa) make reasonable agreement with experiments when superficial gas velocities exceed the minimum fluidization velocity (i.e.,  $U_{mf}=0.20$  m/s)

Almutterah [35] used the 2D E-E model to predict the gas-solid flow in a high density circulating fluidized bed riser. The simulation evaluation was investigated under different superficial gas velocity and solid mass flux conditions. The simulation model is validated by the experiment from Liu [46]. The numerical results showed that the E-E approach can predict the complex gas-solids flow in the high density fast fluidization regime. A core-annular flow structure and the cluster formation of the solid phase are presented for all cases. The prediction of axial particle velocities and solid volume fractions shows a small deviation from experimental data in the central region, while large deviation of solid volume fraction is observed close to the wall. The current models are unable to explain such deviation well.

To study the influence of the restitution coefficient,  $e_{ss}$ , on the hydrodynamics behavior of the gas-solid flow, Loha [21] used the E-E approach in a 2D bubbling fluidized bed framework. The simulation showed that the increasing bed height, quantity and size bubbles can be formed with decreasing restitution coefficient. Large fluctuation in the pressure drop within the bed is affected by the large amount of big bubbles. The time-averaged particle volume fraction for  $e_{ss}$  in the range [0.85-1] were similar for both no-slip and limited-slip boundary conditions. The simulation

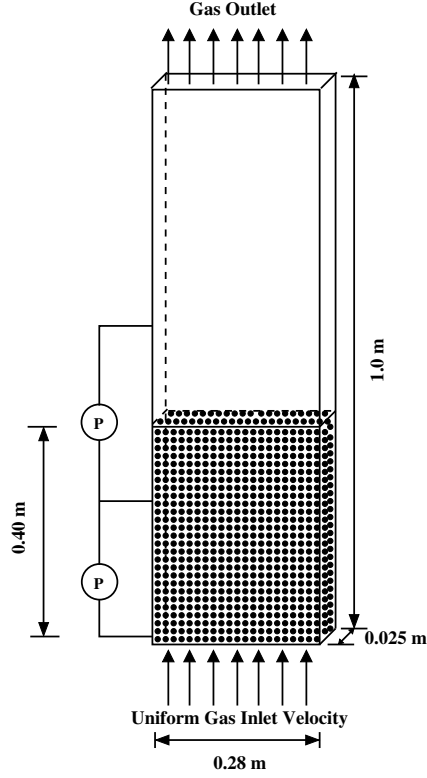


Figure 2.2: Schematic of a fluidized bed reactor, adapted from [8]

results of time-averaged axial particle velocity and granular temperature were in line with experimental measurements for coefficients of restitution of 0.95 and 0.99. The deviation increases with a decrease in the  $e_{ss}$  beyond 0.95.

The E-E approach was used by Cornelissen [33] to simulate a 2D liquid-solid fluidized bed model. The 60 x 500 grid resolution provides a small deviation of 4% against experiment data on overall bed voidage. The influence of variation of restitution coefficient in the range [0.5-1.0] on numerical results is negligible. Both first and second order discretization schemes contributed a high voidage band. The second order discretization scheme led to sharper boundaries. A higher voidage can be predicted with Gidaspow drag submodel. A realistic result can be achieved with a Courant number in the range [0.03-0.3].

Ehsani [34] studied the effect of particle properties on the heat transfer behavior of a 2D liquid-solid fluidized bed heat exchanger with E-L approach. From the simulation predictions, the bed voidage and the Nusselt number increased with the increase of liquid velocity at the fluidized bed regime. The density of particles leads to hydrodynamic effects and thermal effects on the heat transfer process. The variation of specific heat capacity can change the quantity of absorbed energy by

solid. The highest heat absorption capacity (130 KJ) is produced by stainless steel, which reveals that this material is suitable for heat absorbing and regeneration in the bed. The maximum value of  $t_{90}$  (the time required to reach 90% of final temperature of liquid stream) and the minimum value of  $Q_{max}/t_{90}$  can be obtained when particle diameter is 2 mm.

Jin [47] used E-E approach to investigate the hydrodynamic behaviors of a 3D high-flux circulating fluidized bed (HFCFB) model. From the simulation results, large particle ( $d_p > 100 \mu\text{m}$ ) leads to High sensitivity of particle-particle restitution coefficient, while small particle ( $d_p < 100 \mu\text{m}$ ) contributes a low sensitivity. The sensitive of particle-particle restitution coefficient on the variable particle density was not explained. The particle-wall restitution coefficient has negligible effect on the time-averaged solid volume fraction, axial particle and gas velocity. The solids volume fraction declined from [14-4]% near the wall with the increasing of specular coefficient from [0-0.01]. With the increase of solid volume fraction, the solid viscosity increases and granular pseudo-temperature decreases.

To study the effects of specular coefficient and drag submodel on hydrodynamics of dense-solid gas flows, Bakshi [36] used the E-E approach to model a 3D cylindrical bubbling fluidized bed. The numerical results suggested that the faster fluidization with less formed bubbles in the bed center as the bed diameter increased from 14.5cm to 30cm. The values of specular coefficient in the range [0.01-0.3] were workable for most dense solid-gas flows. As the decrease of specular coefficient from 0.0005 to 0.3, the wall resistance decreases resulting a increases of circulation flux. Syamla-O'Brien drag submodel is suitable for  $U/U_{mf} < 4$  while Gidaspow model is appropriate to model homogeneous bubbling fluidization with  $U/U_{mf} > 4$ .

A Gas-liquid-solid fluidized bed framework with a three-dimensional triple-Eulerian approach was used by Hamidipour [37] to study the effect of turbulence regime. The numerical results indicate that the third-order monotone upstream-centered schemes for conservation laws (MUSCL) scheme applies to predicting complex flow patterns in three-phase fluidized beds, while the first-order and second-order upwind schemes should not be chose to avoid large numerical diffusion error. Furthermore, Laminar regime presents a minimum deviation from experiment data, 21.8% for axial solid velocity and 11.4% for gas holdup.  $k - \varepsilon$  formulations that includes Standard dispersed, standard per-phase, standard mixture, RNG dispersed, RNG per-phase, RNG mixture, and realizable dispersed models shows a deviation that within 28.1-161% range and 17.5-52.2% range for axial solid velocity and gas holdup. Better predictions of axial solid velocity near the wall can be achieved by the solid parti-

cles with free-slip wall boundary condition. The increasing of gas holdup and the decreasing of the concentration of solid phase, which were attributed by smaller bubbles, result in lower solid viscosity. A strong circulation close to the wall can be explained as the particle velocity is higher around the wall region than the bed center region.

Link [9] used E-L method to study the various flow regimes on the 3D spout-fluid bed model (see Fig.2.3). By comparing with simulate prediction and experiment measurements, the simulation can predict suitable regime for all regimes except slugging bed regime. The frequency spectra of predicted pressure drop is higher than the experiment measurement for all regime cases. For intermediate/spouting with aeration, intermediate, spout-fluidization, jet in fluidized bed regimes, the fluctuations from prediction were more regular than that from experiment. The E-L approach did not predict large slugs resulting a less regular computed fluctuations in the slugging be regime. The discrepancy between numerical prediction and experiment is attributed by the fluid-particle interaction rater than particle-particle to particle-wall interaction. Both Ergun equation [48] for low porosities and Wen and Yu relation [45] for high porosities developed unsuitable simulation results with stable high velocity inlet in spout-fluid bed. However, the simulation results can be improved with minimum of the drag given by the relations of Koch and Hill [49], Ergun [48], and Wen and Yu [45] .

To study the important influence of the particle clusters on gas-solids flows and on solids residence time distribution in a 3D circulating fluidized bed riser (see Fig.2.4), a E-E approach was used by Hua [10]. To analysis the influence of particle clusters, the minimization multi-scale (EMMS) drag model was applied. From the simulation results, the convective velocity had significant effect on solids RTD, whereas the diffusion coefficient of particles had less influence on solids RTD. The solids RTD showed a plug flow in the riser if there is no effect of particle clusters in the convective velocity. The amplitude and frequency of the fluctuations in the RTD curve were affected by the resolution of the sampling duration. The RTD curve can be changed by an improper valuation of the tracer injection time to a large extent.

Li [38] used the E-E approach to investigate the grid refinement in 2D circulating fluidized bed systems. A good grid convergence can be obtained with a 20-particle-diameter rather than from 10-particle-diameter. The inlet and outlet configurations had influence on the grid convergence behavior of the 2D simulation. Reasonable flow patterns and faster grid convergence can be achieved by symmetric arrangement. The grid independent results cannot be assured by 10-particle rule in

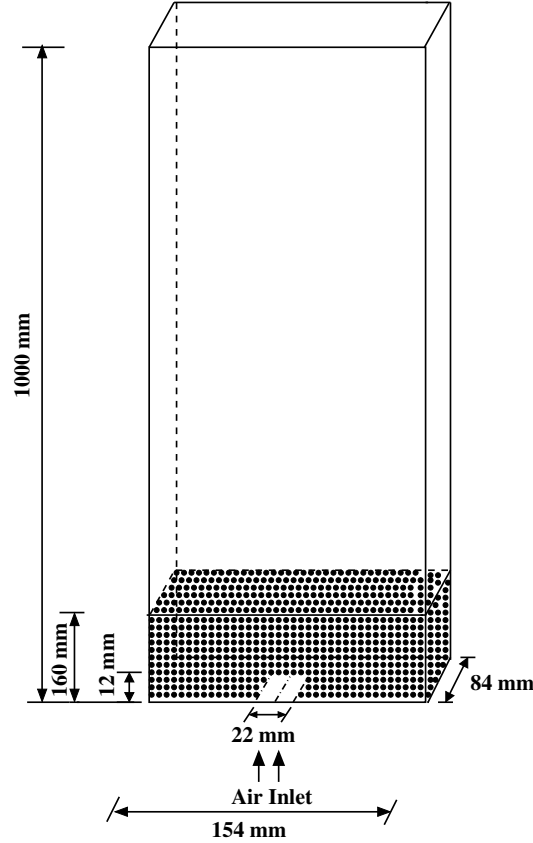


Figure 2.3: Schematic of a spout-fluid bed, adapted from [9]

the complicated asymmetric flow. 3D simulations can give better grid convergent behavior than 2D simulations.

To evaluate the difference between 2D and 3D gas-solids flow simulations, three different circulating fluidized bed risers (CFB riser with a square cross-section, NETL B22 CFB riser and Malcus et al.'s CFB riser) were developed by Li [50] with E-E approach. The simulation predictions showed that the pressure gradient predicted from 3D models close to experiment data, while 2D models predicted lower pressure gradient across the riser. The 3D models make good agreement with experiment data at solids concentration profile. The 3D model can be used to predict the quantitative numerical results while 2D model can only be used for qualitative studies.

Luo [11] studied the effects of gas-solids flow dynamics in an internally circulating fluidized bed (see Fig.2.5) with E-L method. The effects of bed pressure, solid friction coefficient, restitution coefficient, young modulus, diameter and density were investigated in this study. The simulation results showed that the gas bypassing flux

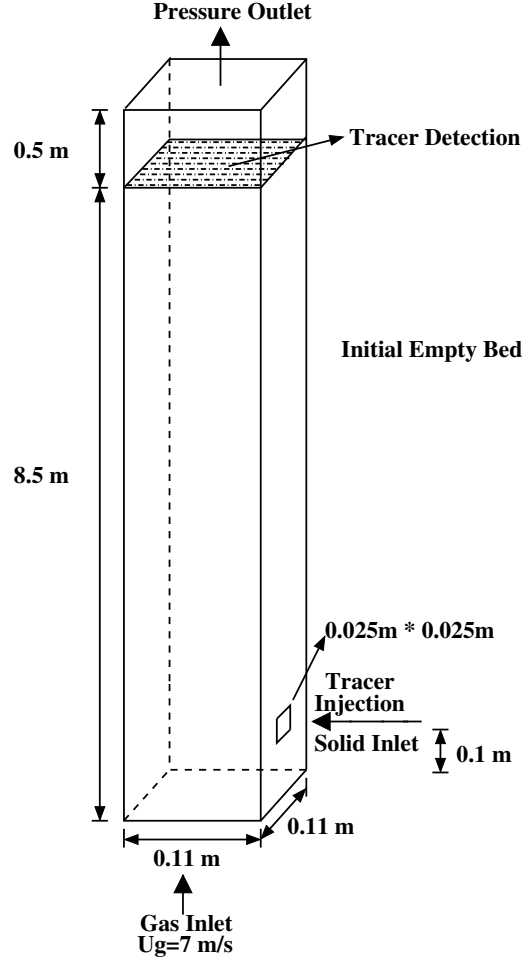


Figure 2.4: Schematic of a circulating fluidized bed riser, adapted from [10]

were significantly affected by the gas property, bed pressure, rather than solid properties. The regulation range of the unit aeration was limited significantly. The gas and solid circulation were affected by the solid properties and plentiful similarities occurred between SCF and GBF. The enlarged solid friction coefficient and diameter can reduce the solid circulation, while the increased solid density, restitution coefficient and gas pressure can improve the solid circulation. The solid behaviors were affected by solid Young modulus slightly. The bed performance was significantly affected by the important parameter,  $U_{mf}$ .

The E-L approach was applied by Luo [39] to investigate the dense gas-solid motions in the 3D internally circulating fluidized bed (ICFB) and circulating fluidized bed. In the ICFB, the component of gas or solid flux was certainly greater from vertical direction than lateral direction. In the right component of two chambers, large gas flux can be concentrated, while transportation of solid phase were developed

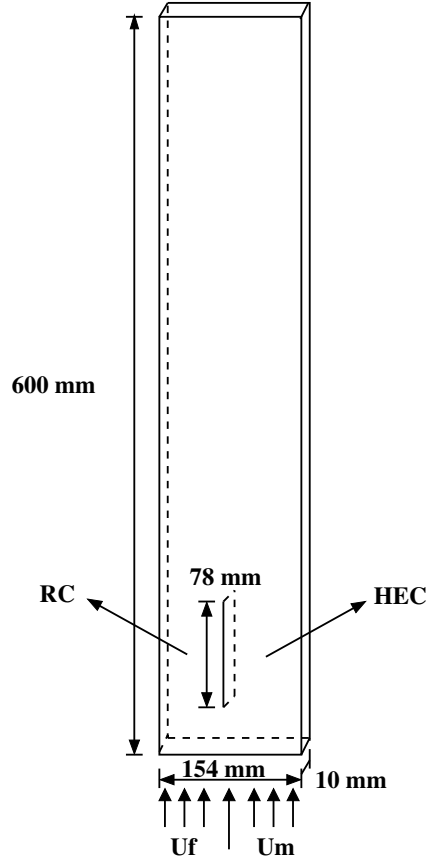


Figure 2.5: Schematic of a interannally circulating fluidized bed riser, adapted from [11]

at the two sides of reactor chamber and under the baffle. Internal solid circulation was formed between two chambers as well. In the region close to the wall of heat exchange chamber, the falling intensity of solid motion increased along the bed height. In the CFB, with bed elevation along the axial direction, the radial gas flow direction was changed. The vertical component of solid velocity is around one order larger than the radial component. The radial component of solid velocity reduced dramatically along the riser height. In the bottom part of the riser, the non-uniform distributions of gas-solid motion can be noticed as well. Strong back-mixing of solid phases can be developed around the wall.

From the research of Muller [40], a 2D gas-fluidized bed was simulated with E-L approach to investigate the effect of the coefficient of restitution, drag laws and the bed transverse thickness. From the simulation predictions, the particle velocities did not affect by the variation of the restitution coefficient between 0.49 and 0.97, whereas the granular temperatures were affected by the restitution coefficient in this

region. The bed thickness affected the particle velocity and granular temperature. Ergun [48] and Wen and Yu [45], DiFelice [51] and Beetstra et al. [52] are three different drag forces that had slightly effect on the simulation prediction. The simulation with Beetstra et al. [52] drag force was in line with the experiment results.

Muller [41] used E-L approach to validate the discrete element model by magnetic resonance (MR) measurements of the time-averaged voidage in a 2D gas-fluidized bed. From the validation results, Ergun [48] and Wen and Yu [45] drag forces were consistent with the experimental measurements, but the most accurate prediction can be achieved by Beetstra et al. [52] drag force. The coefficient of restitution and the coefficient of friction had slight influence on the simulation results. The simulation results were not affected by varying the gas boundary condition from the zero-slip to full-slip at the side-walls. Varying the inlet boundary condition from porous to frit distributor cannot affect the results. However, the most accurate simulation results can be obtained with a non-zero friction coefficient.

To study the gas-solids hydrodynamic behaviors, a 2D cold-mode dual fluidized bed gasifier were applied with E-E approach by Ngyuen [42]. The simulation prediction showed that the solid circulation rate were predicted well at all six different experiments. The cold flow model can be used to predict the solid circulation rate for the hot flow case. The solid holdup of hot rig is less than that of the cold rig at the bottom of riser.

From the research of Shi [53], the solids residence time distribution (RTD) and back-mixing behavior were investigated in a 3D circulating fluidized bed (CFB) riser with a computational Particle Fluid Dynamics (CPFD) approach. From the simulation results, the solids RTD and back-mixing behavior in the riser can be predicted well with CPFD approach from the successful prediction of hydrodynamics and solids mean residence time. There was a non-uniform distribution of particles residence time in the riser. Some particles travel through the riser with a high velocity but some particles with a low velocity. A long residence time from some particles will occur in the basis of the riser. Solids back-mixing usually occurred in the under section of the riser, and stronger solids back-mixing can be achieved with particles down-flow in this section. However, the solids back-mixing degree reduced with the altitude of the riser. The successful CFB products in the industry can be achieved and improved by minimizing the back-mixing of solids in the under section of the riser.

A spout-fluid bed (see Fig.2.6) was performed to investigate gas-solid flow by Yang [12] with E-L model. In this research, the local and overall dispersion behaviors of solid phase, solid circulating, and resident behaviors were studied. The

modeling results indicated that mightily vertical solid dispersion passed out through the central part of the bed while the energetically lateral solid dispersion occurred in the spout section. The distribution of lateral dispersion was significantly influenced by the inlet bed configuration, whereas the affected distribution of vertical dispersion appeared in the fountain section. Large anisotropy of solid dispersion can be achieved along the three directions (X, Y, and Z). Two circulation patterns, gross circulation and local circulation, can attribute internal circulation of solid phase in the bed margin. The maximum solid residence time was developed in the basis corner while the minimum time was in the spout section.

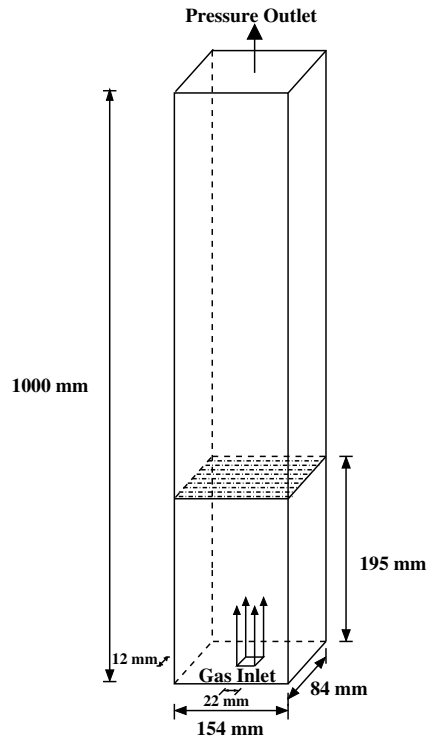


Figure 2.6: Schematic of a spout-fluid bed, adapted from [12]

In spite of numerous works on validation of CFD-based models (E-E or E-L) applied to simulations of fluidized bed, there is a lack of comparison of 2D and 3D simulations. The main objective of present study is to validate the CFD commercial software, Fluent 16.2, applied to a multi-phase modeling of fluidized beds filled with Geldart Group B particles using 2D and 3D approaches. It is necessary to analyze the effects of the Laminar and RANS models on numerical results. Together with the influence of a grid resolution, the sensitivity of key model parameters (the specular coefficient, the restitution coefficient, and the drag submodel) will be evaluated.

## 2.3 Model Formulation

To validate the CFD model and study the sensitivity of parameters of a fluidized bed, the experiment of Taghipour [8] is numerically replicated using 2D and 3D approaches. The principal scheme of the simulation is shown in Fig. 2.7. According to the experimental setup, the Plexiglas column has a height of 1 m, a width of 0.28 m, and a thickness of 0.025 m. Spherical glass particles with a diameter of 250-300  $\mu\text{m}$ , density 2500  $\text{kg}/\text{m}^3$  are fluidized with air at ambient conditions. The static bed height is 0.4 m with a solid volume fraction of 0.6. The overall pressure drop and bed expansion were monitored at superficial gas velocities of  $U=0.38$  m/s and  $U=0.46$  m/s. The measurements of time average pressure drop were recorded at 10 Hz for 20 s intervals once the steady-state conditions were achieved. The voidage measurements were conducted at the height 0.20 m above the distributor plate across the width of the column.

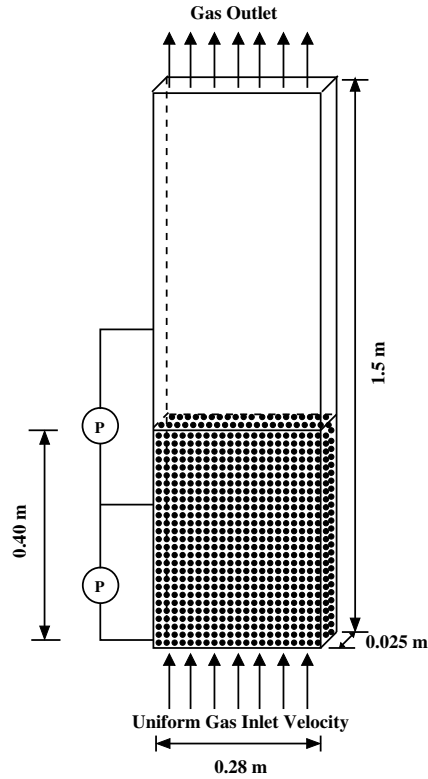


Figure 2.7: Schematic of a fluidized bed reactor, adapted from [8]

On the basis of the E-E approach, the unsteady laminar and turbulent (URANS) formulations for mass and momentum are solved for gas and solid phase separately. The gas phase is modeled using the standard  $k-\varepsilon$  turbulence model with a standard

wall function. The solid phase is modeled with the kinetic theory of granular flows (KTGF) that describes the fluctuations and collisions between the particles. The momentum equation for the gas and solid phases is given by the modified Navier-Stokes equations that include the inter-phase momentum transfer terms. In particular, the frictional viscosity, the drag coefficient submodel, the granular temperature, the bulk viscosities, and the granular temperature are additional terms that depict the momentum exchange. Both turbulence interaction and turbulent dispersion between the gas and solid phases are estimated by the Simoning & Viollet theory [54]. The Tchen theory [55] of dispersion of discrete particles is utilized to estimate turbulent quantities for the particle phase.

In this study, Syamlal-O'Brien [43] and Gidaspow [44] drag submodels are used. The Syamlal-O'Brien drag submodel is based on the terminal particle velocities in fluidized beds [56]. The Gidaspow drag model is an integration of Wen-Yu model and Ergun model that can be applied for the flow where viscous forces are dominant [57]. The Syamlal-O'Brien granular viscosity and solid pressure are investigated. The effect of frictional viscosity is examined.

The boundary conditions in terms of specular coefficients (0.01, 0.1, 0.5, and 0.9) and the particle-particle restitution coefficients (0.90, 0.95, and 0.99) are applied in the simulation and their effects are studied in detail. The maximum packing limit for the solid phase is  $\alpha_{max}=0.63$ . The governing equations are presented in Table 2.3.

The simulation was performed using the CFD commercial software, ANSYS Fluent 16.2. The computational geometry is discretized with three block-structured grids using a finite volume method with 56 x 300, 112 x 600, and 56 x 300 x 5 cells (see Table 2.2). The pressured-based coupled scheme [3] is used to solve mass and momentum conservation equations corresponding to the behavior of the fluidized bed. To fulfill the coupling algorithms, the implicit discretization of both pressure gradient terms and face mass flux are included in the equation. Quadratic Upwind Interpolation for Convection Kinematics (QUICK) scheme [58] is activated to discretize the convection terms in momentum equations. The modified type of the High Resolution Interface Capturing (HRIC) scheme [59] is utilized for estimate the volume fraction of gas or solid. In comparison with QUICK and First Order Upwind schemes, the accuracy of numerical solution can be improved significantly by modified HRIC scheme since the non-linear blend of upwind and downwind differencing are included in this scheme [59]. The 2nd order upwind scheme for the discretizing of convective terms is used in the RANS model. Detailed models and schemes used in the numerical simulation of fluidized beds are given in Table 2.4.

Total physical simulation time of 20 seconds is completed for each simulation, and time-averaged values are obtained from the last 18 seconds after a dynamic steady state converged solution is reached. To avoid instability, a small uniform time step of  $10^{-4}$  s is used for each case, and the number of inner iterations on each time step is set to 50.

<i>Grid</i>	<i>Number of cells</i>
2D-Grid1	56 x 300 = 16800
2D-Grid2	112 x 600 = 67200
3D	56 x 300 x 5 = 84000

Table 2.2: List of different grid resolutions used in simulations of fluidized beds.

Name	Equation
Volume of phase	$V_q = \int_v \alpha_q dv$
Volume fraction balance	$\sum_{q=1}^n \alpha_q = 1$
Effective density	$\hat{\rho}_q = \alpha_q \rho_q$
Continuity equation	$\frac{\partial}{\partial t} (\alpha_q \rho_q) + \nabla \cdot (\alpha_q \rho_q \vec{v}_q) = 0$
Momentum balance	$\frac{\partial}{\partial t} (\alpha_q \rho_q \vec{v}_q) + \nabla \cdot (\alpha_q \rho_q \vec{v}_q \vec{v}_q) = -\alpha_q \nabla p + \nabla \cdot \vec{\tau}_q + \alpha_q \rho_q \vec{g} + \sum_{p=1}^n \vec{R}_{pq}$
Solid phase stress tensor	$\vec{\tau}_q = \alpha_q \mu_q (\nabla \vec{v}_q^T) + \alpha_q (\lambda_q - \frac{2}{3} \mu_q) \nabla \cdot \vec{v}_q \vec{I}$
Interphase force	$\sum_{p=1}^n \vec{R}_{pq} = \sum_{p=1}^n K_{pq} (\vec{v}_p - \vec{v}_q) = \sum_{p=1}^n K_{gs} (\vec{v}_s - \vec{v}_q)$
Richardson and Zaki drag model	$f_{drag} = \frac{3}{4} C_D \frac{\alpha_s \hat{\rho}_s}{d_p}  \vec{v} - u  f(\alpha_g) (\vec{v} - u) = \beta (\vec{v} - u)$
Syamlal-O'Brien drag model (switch function)	$\varphi_{gs} = \frac{\arctan[150 \times 1.75(0.2 - \alpha_s)]}{\pi} + 0.5$
Gidaspow drag model	When $(\alpha_g > 0.8)$ , $K_{gs} = \frac{3}{4} C_D \frac{\alpha_s \alpha_g \rho_g  \vec{v}_s - \vec{v}_g }{d_s} \alpha_g^{-2.65}$ , $C_D = \frac{24}{\alpha_g Re_s} [1 + 0.15 (\alpha_g Re_s)^{0.687}]$ When $(\alpha_g \leq 0.8)$ , $K_{gs} = 150 \frac{\alpha_s (1 - \alpha_g) \mu_g}{\alpha_g d_s^2} + 1.75 \frac{\alpha_s \rho_g  \vec{v}_s - \vec{v}_g }{d_s}$
Transport equation (algebraic)	$(-p_s \vec{I} + \vec{\tau}_s) : \nabla \vec{v}_s + \gamma \theta_s + \phi_{gs} = 0$
Solid pressure	$p_s = \alpha_s \rho_s \theta_s + 2 \rho_s (1 + e_{ss}) \alpha_s^2 g_{0,ss} \theta_s$
Radial distribution function	$g_{0,ss} = \left[ 1 - \left( \frac{\alpha_s}{\alpha_{s,max}} \right)^{\frac{1}{3}} \right]^{-1}$
Collisional energy dissipation	$\gamma \theta_s = \frac{12(1 - e_{ss}^2) g_{0,ss}}{d_s \pi^{0.5}} \rho_s \alpha_s^2 \theta_s^{1.5}$
Kinetic energy transfer	$\phi_{gs} = -3 \cdot K_{g,s} \theta_s$
Solid shear viscosity	$\mu_s = \mu_{s,col} + \mu_{s,kin} + \mu_{s,fr}$
Collisional viscosity	$\mu_{s,col} = \frac{4}{3} \alpha_s \rho_s d_s g_{0,ss} (1 + e_{ss}) \left( \frac{\theta_s}{\pi} \right)^{1/2}$
Kinetic viscosity	$\mu_{s,kin} = \frac{10 \rho_s d_s \sqrt{\theta_s \pi}}{96 \alpha_s (1 + e_{ss}) g_{0,ss}} \left[ 1 + \frac{5}{4} g_{0,ss} \alpha_s (1 + e_{ss}) \right]^2$
Frictional viscosity	$\mu_{s,fr} = \frac{p_s \sin \phi}{2 \sqrt{I_{2D}}}$
Bulk viscosity	$\lambda_s = \frac{4}{3} \alpha_s \rho_s d_s g_{0,ss} (1 + e_{ss}) \left( \frac{\theta_s}{\pi} \right)^{1/2}$

Name	Equation
Grandual temperature	$\Theta_q = \frac{1}{3}(\bar{v}_q'^2)$
Reynolds stress tensor	$\bar{\tau}_q'' = \frac{2}{3}(\rho_g k_g + \rho_g \mu_{t,g} \nabla \cdot \bar{U}_g) \bar{I} + \rho_g \mu_{t,g} (\nabla \cdot \bar{U}_g + \nabla \cdot \bar{U}_g^T)$
$\kappa - \varepsilon$ model	$\frac{\partial}{\partial t} (\alpha_g \rho_g k_g) + \nabla \cdot (\alpha_g \rho_g \bar{U}_g k_g) = \nabla \cdot (\alpha_g \frac{\mu_{t,g}}{\sigma_k} k_g) + \alpha_g G_{k,g} - \alpha_g \rho_g \varepsilon_g + \alpha_g \rho_g \Pi_{k,g}$ $\frac{\partial}{\partial t} (\alpha_g \rho_g \varepsilon_g) + \nabla \cdot (\alpha_g \rho_g \bar{U}_g \varepsilon_g) = \nabla \cdot (\alpha_g \frac{\mu_{t,g}}{\sigma_\varepsilon} \varepsilon_g) + \alpha_g \frac{\varepsilon_g}{k_g} (C_1 G_{k,g} - C_2 \rho_g \varepsilon_g) + \alpha_g \rho_g \Pi_{\varepsilon,g}$
Turbulence equations for dispersed phase	$k_s = k_g (b^2 + \eta_{sg}) / (1 + \eta_{sg})$ $k_{sg} = 2k_g (b + \eta_{sg}) / (1 + \eta_{sg})$ $D_{t,sg} = \frac{1}{3} k_{sg} \tau_{t,sg}$ $D_s = D_{t,sg} + (\frac{2}{3} k_s - b \frac{1}{3} k_{sg}) \tau_{F,sg}$ $b = (1 + C_v) (\frac{\rho_s}{\rho_g} + C_v)^{-1}$
Momentum transfer coefficient	$\beta = \frac{3}{4} C_D \frac{\alpha_s \rho_g}{d_p}  \bar{v} - u  f(\alpha_s)$

Table 2.3: Model equations available by ANSYS Fluent 16.2 which were used to model the fluidized bed from[3],[4].

<i>Name</i>	<i>Model/ Scheme Name</i>
Multiphase Flow	Euler-Euler [3]
Volume Fraction Parameters	Implicit Scheme [3]
Viscous Model	Laminar & RANS- $k-\varepsilon$ model [3]
Drag Model	Syamlal-O'Brien & Gidaspow [43], [44], [3]
Granular Temperature	Algebraic [3]
Granular Viscosity	Syamlal-O'Brien [43], [3]
Granular Bulk Viscosity	Lun et al. [60], [3]
Frictional Viscosity	Johnson et al. [61], [3]
Frictional Pressure (pascal)	Based-ktgf [62], [3]
Solid Pressure	Syamlal-O'Brien [43], [3]
Radial Distribution	Syamlal-O'Brien [43], [3]
Pressure-Velocity Coupling	Coupled Scheme [3]
Spatial Discretization-Gradient	Least Squares Cell Based [3]
Spatial Discretization-Momentum	QUICK [58]
Spatial Discretization-Volume Fraction	Modified HRIC [59]
Spatial Discretization-Turbulence	$k-\varepsilon$ 2nd order Upwind [3]
Transient Formulation	First Order Implicit

Table 2.4: List of different models and schemes used in simulations of fluidized beds.

## 2.4 Results: Validation

To study transient dynamics of the gas and solid flows in a fluidized bed, we use volume-averaged or global velocity of the solid phase in the entire cavity. For this purpose we introduce the volume-averaged solid flow velocity  $U_s$  [63]:

$$U_s = \frac{2\pi}{V_{sb}} \int_0^R \int_0^H \left( \sqrt{u_{s,r}^2 + u_{s,z}^2} \right) r dr dz \quad (2.1)$$

where  $V_{sb}$  is the volume of the whole fluidized bed reactor and  $u_s$  is the velocities of the solid phase. This global velocity is used to calculate a spin-up or start up time for volume-force driven flows [63]. Time histories of  $U_s$  calculated using different values of specular coefficient for 2D and 3D approaches are depicted in Fig. 2.8. It can be seen that the fluidized bed reaches dynamic steady state after 2.5 sec. Analysis of  $U_s$  time history reveals that the solid velocities predicted using 2D model are higher than velocity obtained from the 3D model. Dominant velocity between 0.2-0.3 m/s and 0.1-0.2 m/s are found for 2D and 3D, respectively. The lower solid velocity from 3D models is explained by the loss of extra friction as the increasing of contact area between fluid and walls. 2D models produce similar trend of volume-averaged solid velocity. A remarkable narrow peak in the volume-averaged velocity profile is

capture well by all models after 1-1.5 seconds. This peak corresponds approximately to the start up time. After this time, the fluctuation is leveling out apparently except for 2D models.

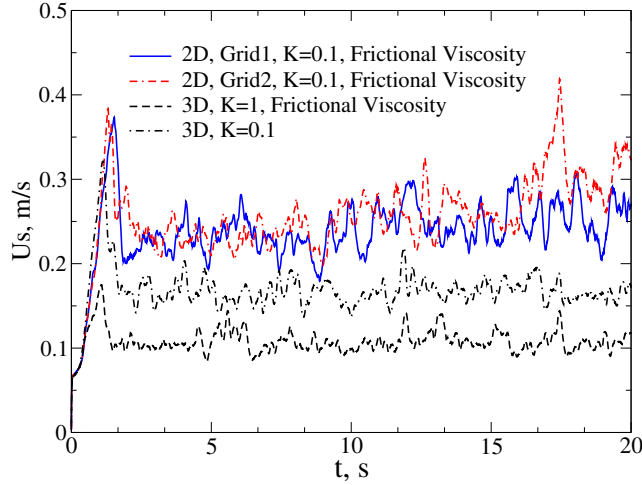


Figure 2.8: Volume averaged solid velocity ( $U_s$ ) as a function of time for RANS models: drag function: Syamlal–O’Brien; Inlet Velocity:  $U=0.38\text{m/s}$ ; Restitution coefficient:  $e_{ss}=0.9$

To illustrate the fluidized bed behavior, Fig.2.9 shows snapshots of the slice of 3D contour plot of solids fraction and turbulent viscosity ratio evolution through the time. The red color represents the maximum solid volume fraction and turbulent viscosity ratio, whereas the blue color denotes the minimum value. As can be seen from Fig.2.9a, bubbles formed at the bottom of the bed move up to the bed surface with the increasing bubble size. The structure of bubbles ceases to remain spherical because of the intensive breaking and coalescing of bubbles. Upon reaching the bed surface, the solid particles were forced towards the wall with the burst of big bubbles and then fall downward by the side walls due to the gravitational force. A dynamic steady state is reached after the start up time ( $t=1$  s). Steady fluctuation can be observed in the bed surface that might be caused by continuous formation, rise, coalescence, and burst of bubbles. This can be attributed more straightforward from the time snapshots for the turbulent viscosity ratio as depicted in Fig.2.9b. The distribution of turbulence is consistent with the gas flow patterns. High turbulent ratio exists inside the big bubble space at start up phase. After reaching the dynamic steady state, weak turbulent viscosity ratio in the range of [0-10] can be observed inside the bed, while strong turbulence in the range of [15-110] are distributed above the bed surface. The reason of this phenomenon is the less amount of gas (bubbles)

is trapped inside the bed, whereas gas is filled completely above bed surface by releasing trapped gas from the bubbles.

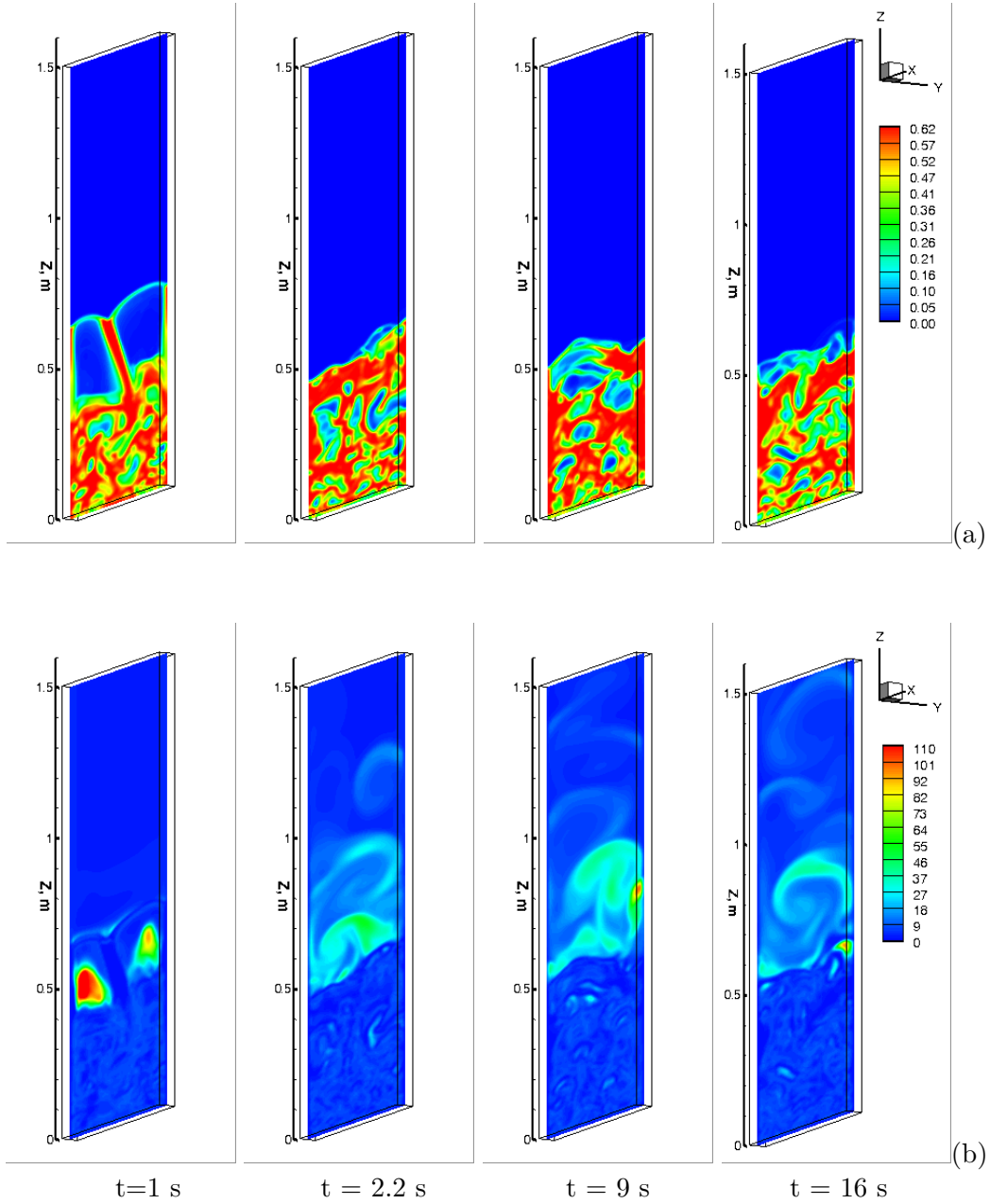


Figure 2.9: 3D-RANS: Simulated (a) solid volume fraction and (b) turbulent viscosity ratio: drag function: Syamlal–O’Brien; Inlet Velocity:  $U=0.38\text{m/s}$ ; Specularity coefficient:  $K=0.1$ ; Restitution coefficient:  $e_{ss}=0.9$ .

To validate the numerical results obtained in the framework of the E-E model,

simulations were carried out of the 3D fluidized bed. Fig. 2.10 compares the predicted void fraction values against the experiment data along  $x$ -coordinate at  $z = 0.2$  m. The experimental data is adapted from the experiment carried out by Taghipour [8]. The averaged deviation from experimental values for all three numerical calculations is 5.36% suggesting that the 3D approach produces a good agreement with the experimentally measured void fraction profiles. It can be seen that there is a flat distribution with high gas volume fraction in the central region and sharp distribution with low gas volume fraction close to the wall. The axial variations in gas volume fraction are similar for coefficient of restitution 0.9 and 0.95 without the activation of the fictional viscosity submodel. The deviations are 4.86% and 4.71% for each of them. It confirms that there is no qualitative change in the nature of variation of the results by varying the coefficient of restitution within a range of [0.9-0.95]. However, an relatively large deviation (6.50%) against experiment data is presented by increasing of specularity coefficient,  $K$ , from 0.1 to 1. This overestimated prediction is caused by perfectly diffuse collision between particle and walls when  $K = 1$ .

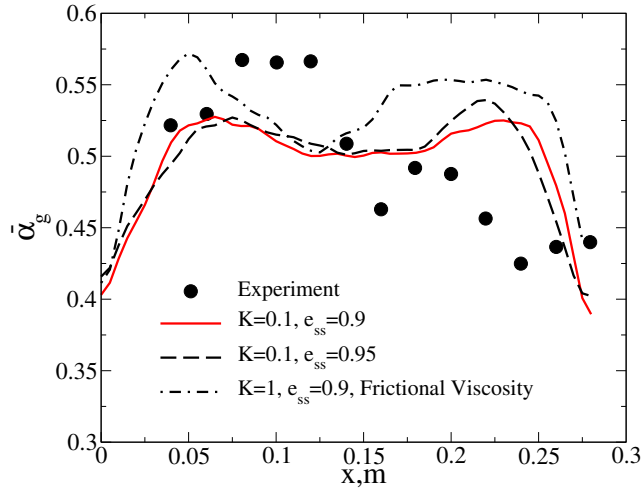


Figure 2.10: 3D-RANS: Experimental[8] and simulated time-averaged void (gas phase) fraction profiles at  $z = 0.2m$  calculated for  $U = 0.38m/s$ .

The 2D approach of unsteady Laminar E-E and RANS E-E models and its sensitivity to the grid resolution was assessed. In this case, 2D fluidized bed configuration was simulated on two different grid size (56 x 300 and 112 x 600). The particle concentration distributions inside the fluidized bed for Laminar and RANS viscous models is shown in Fig. 2.11. Same as in 3D simulation, the bubbles undergo the formation, rise, coalescence, and burst. By comparing the flow pattern in

Fig. 2.11a and Fig. 2.11b, it is noticed that the solid flow pattern in the bed are symmetrical for Laminar model at the beginning of simulation, which in contrast to the asymmetric pattern for RANS model. This can be explained by the unsteady state of the fluid at initial state. The solid volume fraction in the bed predicted with the fine grid resolution is represented in Fig. 2.12. More small bubbles with sharp bubble interfaces can be observed from the refined grid resolution. This can be explained that the refined mesh results in the decrease of grid space. Consequently, small bubbles can be observed from the unit cell of a reduced size. In contrast to the asymmetric pattern at the start up state in coarse grid, both Laminar and RANS models presented a relatively symmetrical distribution of particles in the refined grid resolution. After reaching the dynamic steady state, similar bubble size and expanded bed height can be observed for both Laminar and RANS models on each grid resolution.

Fig. 2.13 displays the contour plots of the turbulent viscosity ratio in 2D model with  $56 \times 300$  and  $112 \times 600$  cell resolutions. Similar with 3D model: weak turbulence distributed in the bed, and high turbulence exists above the bed surface. In the start up state, we barely can see the turbulence in the whole domain for both grid resolutions. After reaching the dynamic steady state, the turbulent viscosity ratio in the packed bed is in the region  $[0-37]$  and  $[0-52]$ , while in the gas phase is in between  $[112-450]$  and  $[103-310]$  for grid 1 and grid 2 model, respectively. The possible reason is discussed in the 3D simulation.

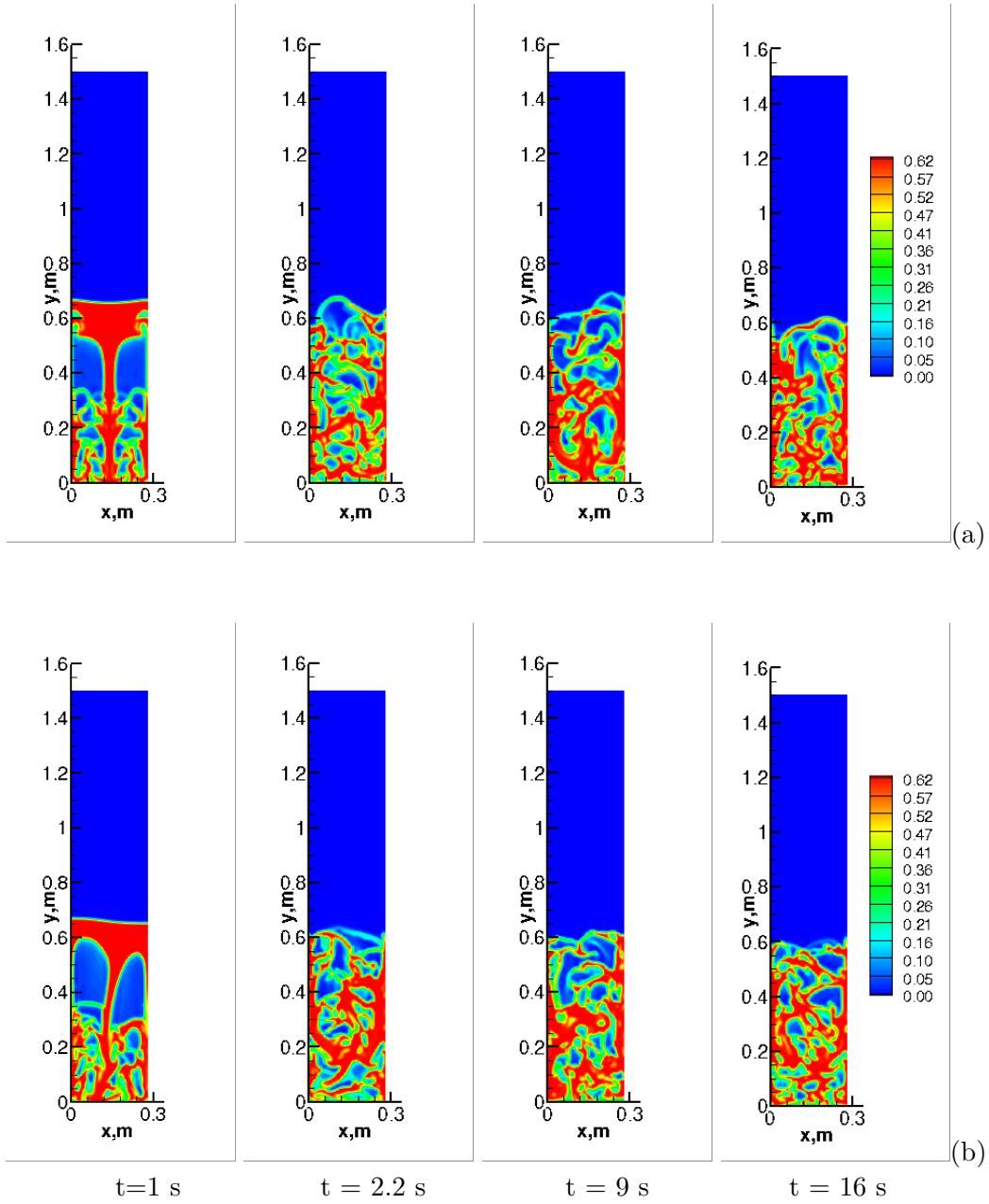


Figure 2.11: 2D: Solid volume fraction calculated using unsteady (a) Laminar and (b) RANS E-E model, Grid 1:  $U = 0.38m/s$ ,  $K=0.1$ ,  $e_{ss}=0.9$ .

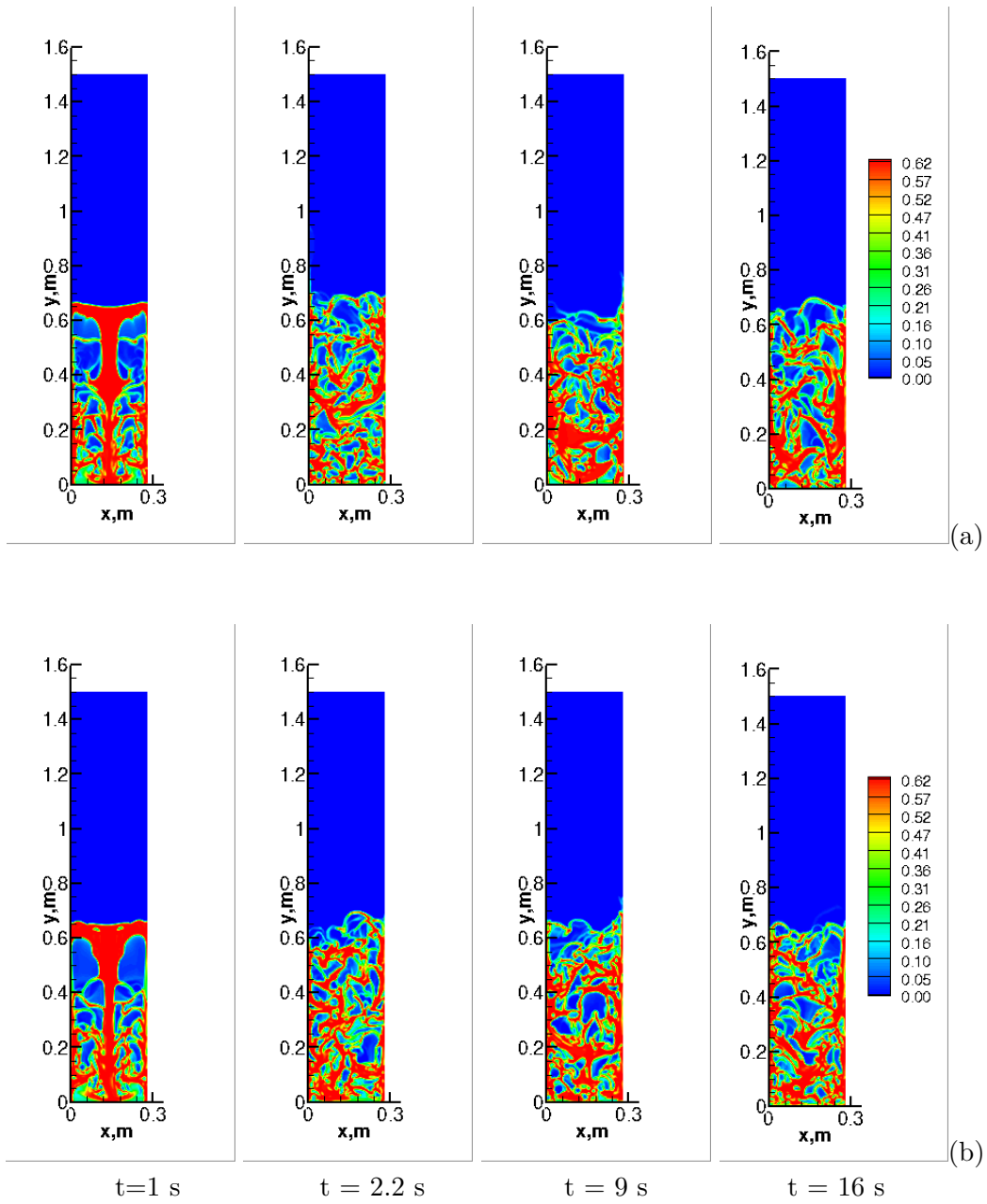


Figure 2.12: 2D: Solid volume fraction calculated using unsteady (a) Laminar and (b) RANS E-E model, Grid 2:  $U = 0.38m/s$ ,  $K=0.1$ ,  $e_{ss}=0.9$ .

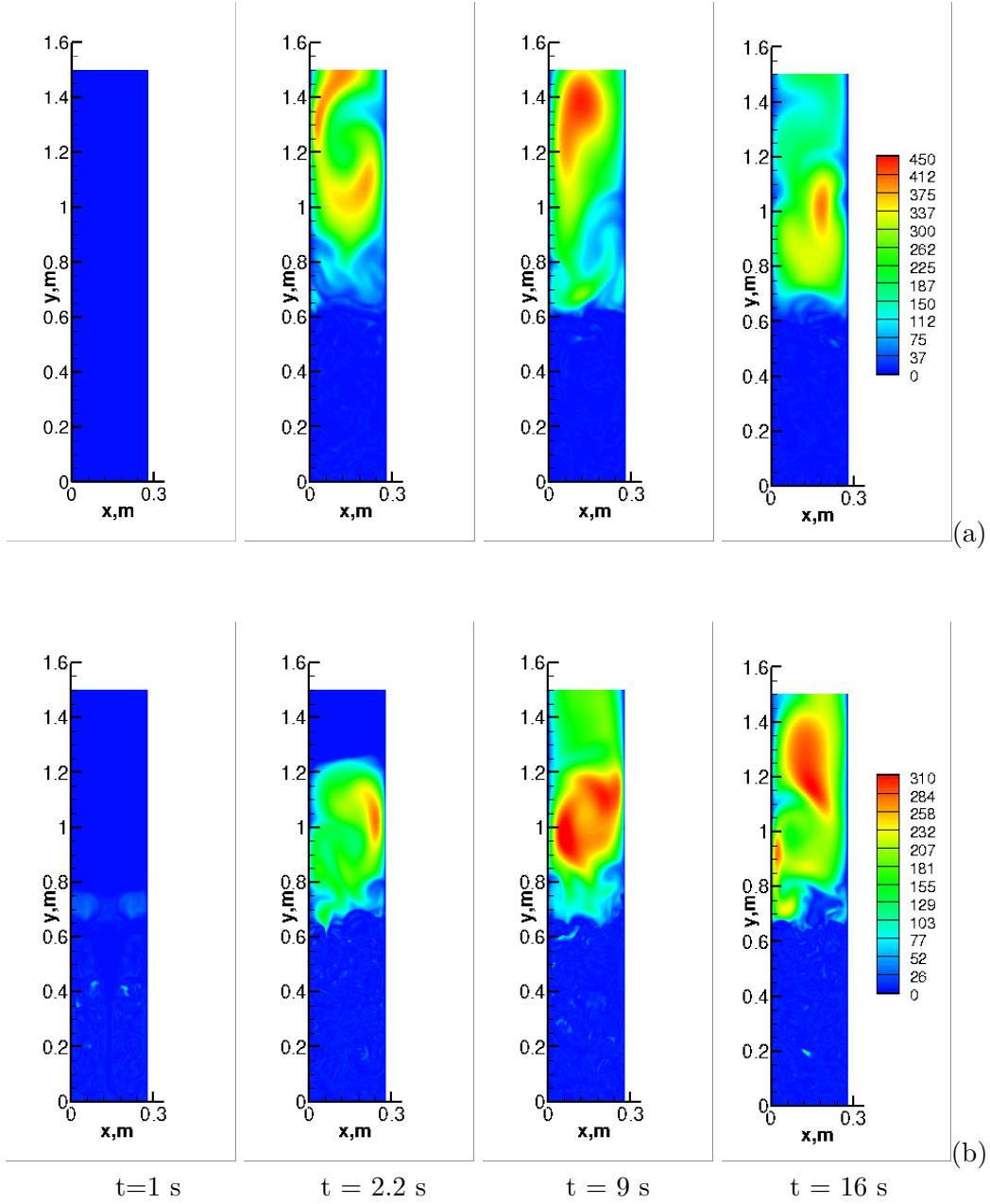


Figure 2.13: 2D-RANS: Turbulent viscosity ratio  $\frac{\mu_t}{\mu_0}$  at  $t = 1, 2.2, 9,$  and  $16\text{s}$ : drag function: Syamlal O'Brien; Inlet Velocity:  $U_{in} = 0.38\text{m/s}$ ; Specularity coefficient:  $K = 0.1$ ; Restitution coefficient  $e_{ss} = 0.9$ . (a) Grid 1 and (b) Grid 2.

In order to study the overall behavior of the fluidized bed, 2D time-averaged solid fraction contour plots for case of Laminar and RANS models on different grid resolutions are depicted in Fig 2.14. The symmetry in the flow is achieved in all the

cases. The solid-phase distribution is similar for both Laminar and RANS models suggesting that fluidization hydrodynamics are not sensitive to the choice of Laminar or RANS model. It shows a higher solid volume fraction close to the wall (0.6) and at the bottom of the bed (0.45). A lower solid volume fraction (0.3) is observed in the center of the bed. This distribution of solid volume fraction reveals that more bubbles are formed at the center region rather than the bottom. 15% solid volume fraction can be observed from the bed surface demonstrating the bursting of the bubbles when approaching the surface region.

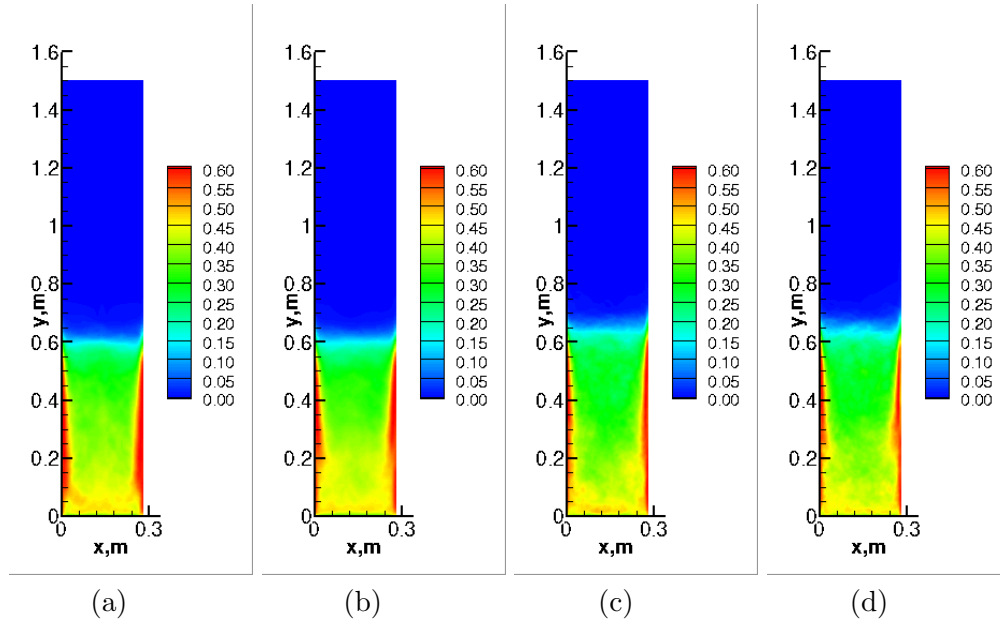


Figure 2.14: 2D-RANS: Time-averaged solid volume fraction: drag function: Syamlal O'Brien; Inlet Velocity:  $U_{in} = 0.38m/s$ ; Specularity coefficient:  $K = 0.1$ ; Restitution coefficient  $e_{ss} = 0.9$ . (a) Laminar model-Grid 1, (b) RANS model-Grid 1, (c) Laminar model-Grid 2, (d) RANS model-Grid 2.

A grid independence study shows that a further grid refinement in 2D models has significant influence on numerical solutions. Fig. 2.15a presents a comparison of the predicted time averaged gas volume fraction with experimental results by different models and drag submodels with the  $56 \times 300$  grid framework. A better numerical result with a deviation of 4.50% is contributed from RANSmodel by taking into account the Syamlal-Obrien drag submodel and Johnson-et-al frictional viscosity. Whereas the Laminar model gives largest discrepancy, 9.30%, with experiment measurements. The simulation using Syamlal-Obrien drag submodel gives 6.17% deviation, while that using Gidaspow submodel shows a deviation of 8.78%.

This reveals that use of the Syamlal-Obrien drag submodel to predict the gas flow pattern in this fluidized bed gives more accurate results. The RANS model with a Syamlal-Obrien drag submodel presents a relatively fully developed bubbly flow pattern while the Laminar model shows an annular flow pattern from the profile. This can be explained by irregular fluid flow from turbulent regime and uncrossed orderly fluid flow produced by the laminar regime. The velocity of fluid is not constant at any point of fluid for turbulent regime, but constant velocity can be represented by laminar regime. Consequently, the distribution of void fraction pattern is consistent with the fluid velocity profile.

Fig. 2.15b shows the numerical results based on the 112 x 600 grid. The profile depicts that the simulation with the frictional viscosity can provide better agreement with experiment data. The deviation for the frictional viscosity submodel is 6.19%, while the deviation for RANS model without applying frictional viscosity is 10.15%. Similar trend of time-averaged void fraction profile can be predicted by different models without taking into account the frictional viscosity. The RANS model with Syamlal-Obrien drag submodel is 1.64% accurate than in comparison to both Laminar model and RANS model with Gidaspow drag submodel. The largest difference between predicted gas volume fractions and experimental measurement appeared in the distance interval between 0.15 and 0.28 meters. This can be attributed to the fact that the choice of appropriate multiphase model or drag submodel along might probably not improve the numerical results. Some other parameters such as frictional viscosity submodel, specular coefficient and wall roughness are not properly modeled in the bed.

The influence of frictional viscosity is depicted using both grids. The RANS model without frictional viscosity demonstrates an averaged excessive prediction, 8.16% across the full cross-section, whereas the model with frictional viscosity shows an averaged deviation of 5.35%. The stress that is generated by friction between the particles can be contributed to the solids shear viscosity. Consequently, higher energy loss and lower gas volume fraction appeared due to the high viscous solid particles.

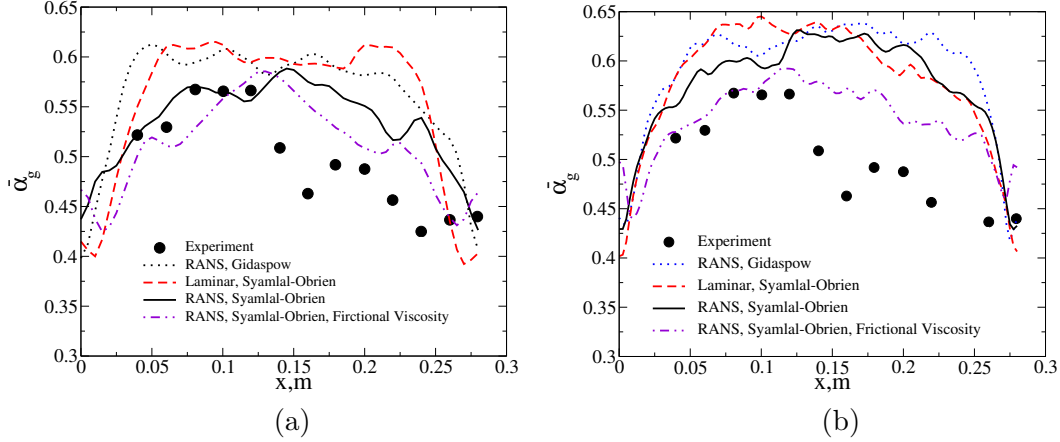


Figure 2.15: 2D: Experimental[8] and simulated time-averaged void fraction profiles at  $z = 0.2m$  for 2D,  $U = 0.38m/s$ ,  $K = 0.1$ ,  $e_{ss} = 0.90$ , (a) Grid 1, (b) Grid 2.

Four different values of specularity coefficients ( $K$ ) in the range  $[0.01-0.9]$  are considered in 2D numerical models. The comparison of experimental and numerical data is presented in the Fig. 2.16a. The differences in the numerical results using various specularity coefficients are more distinct while studying the time-averaged void fraction distribution. With the decrease of specularity coefficient from 0.9 to 0.1, the trend of void fraction with deviation in the range  $[7.57-7.99]\%$  can be observed. This suggests that the influence of  $K$  in the range  $[0.1-0.9]$  is negligible on the numerical prediction of void fraction pattern. The existence of a core-annular structure of the flow predicted gas volume fraction are presented for  $K$  between 0.1 and 0.9. When the specularity coefficient decreases to 0.01, a different gas volume fraction pattern is observed with down flow of gas near the wall and at the center with the deviation of 9.68%. Two maximum gas volume fraction values, around 0.64, can be found at  $x=0.05$  and  $0.225$  m. The lower value of specularity coefficient means the resistance between particle and wall is small. Consequently, more concentrated particles are distributed close to the wall, resulting two peaks of void fraction located each side between the center and the wall.

Frictional viscosity significantly affects the particle behavior close to the wall. Fig.2.16b shows that we have different value of gas volume fraction on the wall by the same value of  $K = 0.1$ . Activation of frictional viscosity models by the small value of  $K$  increases of 6.42% void fraction on the wall. In the near wall region, void fraction decreases thickness of  $54.5 \mu m$  diameter of particles. A further investigation should be approached on a refined grid model to explain this phenomenon. We have local minimum of void fraction when frictional viscosity is activated. For  $K=1$ , minimum value of void fraction, 41.6%, can be observed on the wall. This is due

to the fact that the large wall shear stress resulting fluid velocity at wall point is 0. Consequently, large number of particles forms a layer of particles stick to the wall.

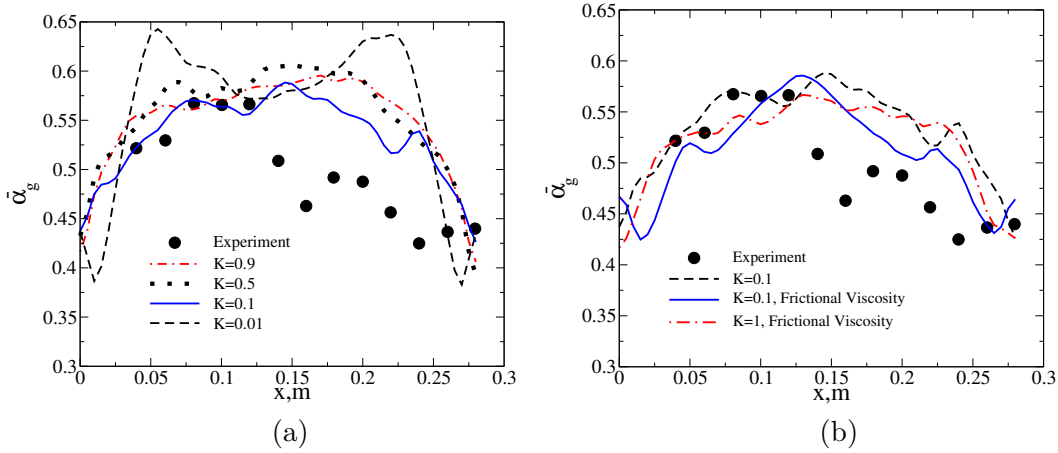


Figure 2.16: 2D: Experimental[8] and simulated time-averaged void fraction profiles at  $z = 0.2m$  predicted for different specularity coefficients on RANS models: (S-O)  $U = 0.38m/s$ ,  $e_{ss} = 0.90$ .

Fig. 2.17 presents the axial distributions of time-averaged void fraction as a function of the coefficient of restitution ( $e_{ss} = 0.90, 0.95$ , and  $0.99$ ) with 3D approach. It was observed that the core-annular structure of the flow are predicted for all inelastic collisions. The void fraction was larger in the central region and less in the near wall region. A higher void fraction with a value of 46% is observed on the wall for  $e_{ss} = 0.90$ . This can be explained by formation of many larger bubbles at a lower coefficient of restitution. The deviation of numerical results against experiment data are 6.17%, 7.60%, and 7.72% for  $e_{ss} = 0.90, 0.95$ , and  $0.99$ , respectively. This suggests that the void fraction is not sensitive to the choice of  $e_{ss}$  in the range  $[0.90-0.99]$ .

Fig. 2.18 depicts 3D simulated time-averaged void fraction profile with the inlet gas velocity of  $0.46m/s$ . By comparing the numerical results with the experiment points, both models give small deviation, 4.71% and 4.01%. With the increase of specularity coefficient from 0.1 to 0.5, the minimum value of void fraction (40.5%) can be observed on the wall, the main possible reason are explained in the previous discussion.

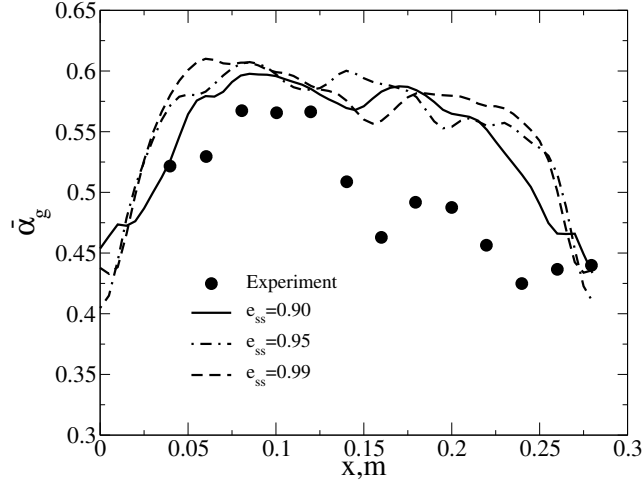


Figure 2.17: 3D-RANS: Experimental and simulated time-averaged void (gas phase) fraction profiles at  $z = 0.2m$  calculated for  $U = 0.38m/s$ : (S-O)  $K = 0.1$ .

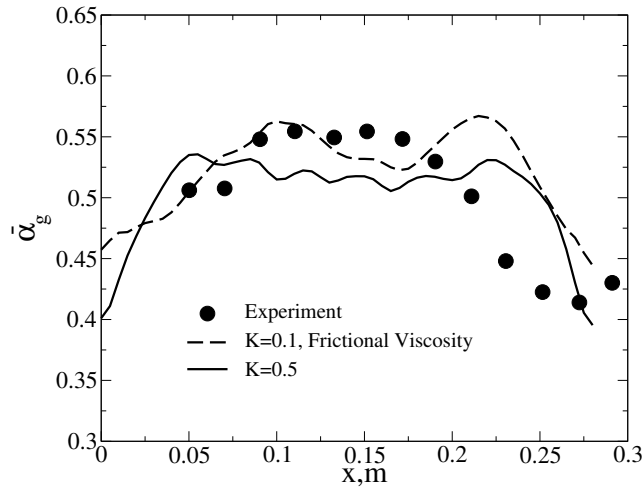


Figure 2.18: 3D-RANS: Experimental[8] and simulated time-averaged void (gas phase) fraction profiles at  $z = 0.2m$  calculated for  $U = 0.46m/s$ : (S-O)  $e_{ss} = 0.90$ .

Fig.2.19 and Fig.2.20 show the change of volume-averaged solid velocity over time for 3D and 2D simulations, respectively. Fig.2.19 reveals that the solid velocity is significantly affected by the variation of specular coefficient in the range [0.1-1]. For the inlet gas velocity of 0.38 m/s, the solid velocity pattern of  $K = 1$  model is lower than that of  $K = 0.1$  model. The dominant solid velocity is around 0.1 m/s and 0.15 m/s for each of them. The unity value of specular coefficient leads to zero fluid velocity on the wall resulting in such lower value of time-averaged solid

velocity. The effect of inlet gas velocity is more pronounced for the solid velocity profile. With the increase of superficial gas velocity from 0.38 m/s to 0.46 m/s, the higher solid velocity pattern with an averaged value of 0.2 m/s is observed. Particles are carried up in the central region and fall down in the near wall region by the inlet gas. Thus, a positive relation between superficial gas velocity and particle velocity results in this phenomenon.

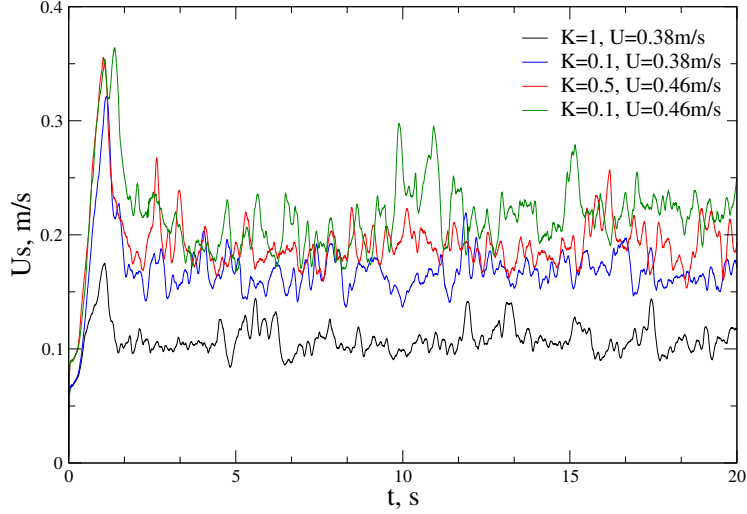


Figure 2.19: Volume averaged solid velocity ( $U_s$ ) as a function of time for 3D RANS models: Drag function: Syamlal–O’Brien; Restitution coefficient:  $e_{ss}=0.9$

For the 2D simulations, the computed volume-averaged solid velocity fluctuations were studied using  $56 \times 300$  and  $600 \times 112$  grids shown in Fig.2.20a and b, respectively. On both grids, the cases when the specular coefficient  $K=1$  give a lowest averaged solid velocity of 0.2 m/s. The main possible reason is the large number of particles forms a layer of particles stick to the wall when  $K=1$ . From Fig.2.20a, we have different value of solid velocity for the same value of  $K$ . Activation of frictional viscosity submodel keeping the same value of  $K$  contributes 17.2% decrease of volume-averaged solid velocity. This can be explained by the more energy lose contributed from the frictional viscosity. There is no distinct discrepancy of velocity profile relative to  $K$  between 0.01 to 0.5. The dominant solid velocity for  $K$  in this range is [0.28-0.3] m/s. In Fig.2.20b, we refine the grid resolution from  $56 \times 300$  to  $600 \times 112$  to present detail information of variation of volume-averaged solid velocity. Same as 3D model, with the increase of superficial velocity to 0.46 m/s, the higher solid velocity with average value of 0.4 m/s can be observed. The variation of drag submodel affect the solid velocity pattern. For the same value of

$K$ , Syamlal-Obrien submodel leads to higher value of solid velocity, 0.35 m/s, while Gidaspow submodel contributes a lower velocity, 0.3 m/s.

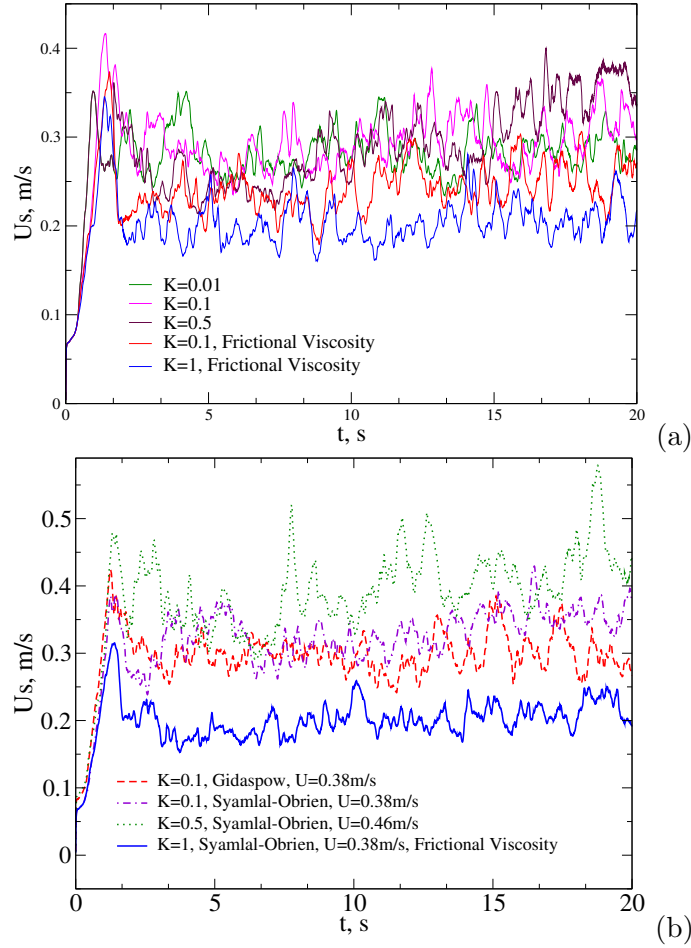


Figure 2.20: Volume averaged solid velocity ( $U_s$ ) as a function of time for 2D RANS models:  $e_{ss}=0.9$ , (a) Grid 1,  $U = 0.38$  m/s, (b) Grid 2

To gain insight into the accuracy of numerical predictions, the standard error profiles of the 3D and 2D models at  $U = 0.38$  m/s and  $U = 0.46$  m/s are shown in Fig.2.21 and Fig.2.22, respectively. As can be seen from both profiles, the standard deviation of 3D and 2D models is in the range [4.01-6.5]% and [4.48-13.08]%, respectively. The difference for the maximum and minimum deviations on 3D and 2D models was found 2.49% and 8.60%. This reveals that the 3D model is suitable in the modeling of fluidized bed as compared to the 2D model. The standard error can provide more accurate measures as compared to other functions (e.g weight standard error) since this method comes from Linear Least Squares Regression. The

standard error of the estimate is defined below:

$$\sigma_{est}\% = \sqrt{\frac{\sum(Y_{simulation} - Y_{experiment})^2}{N}} * 100 \quad (2.2)$$

Where  $\sigma_{est}$  is the standard error of the estimate,  $Y_{experiment}$  is the experiment measurements,  $Y_{simulation}$  is a predicted value, and  $N$  is the number of points.

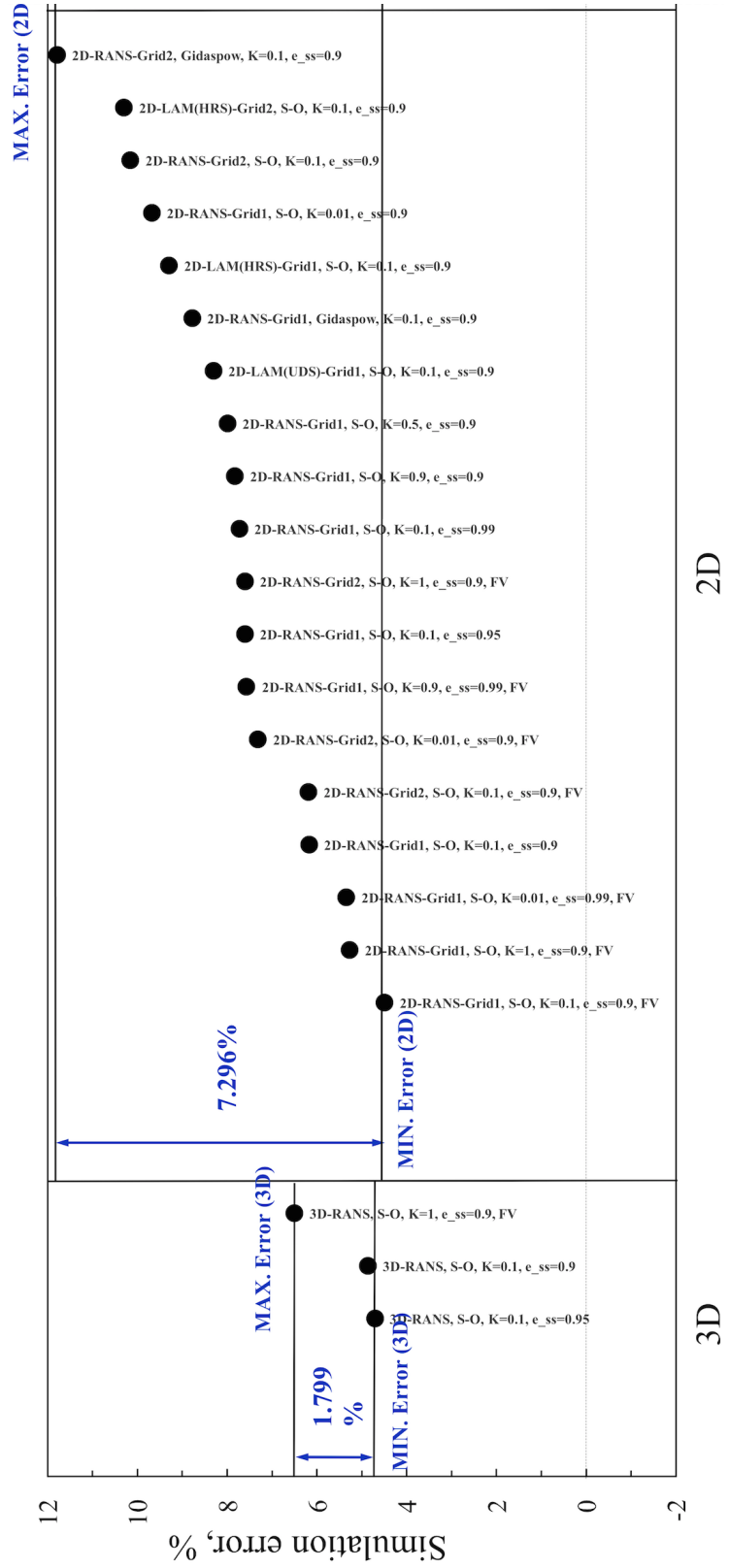


Figure 2.21: Simulation errors for 3D and 2D models at  $U = 0.38m/s$

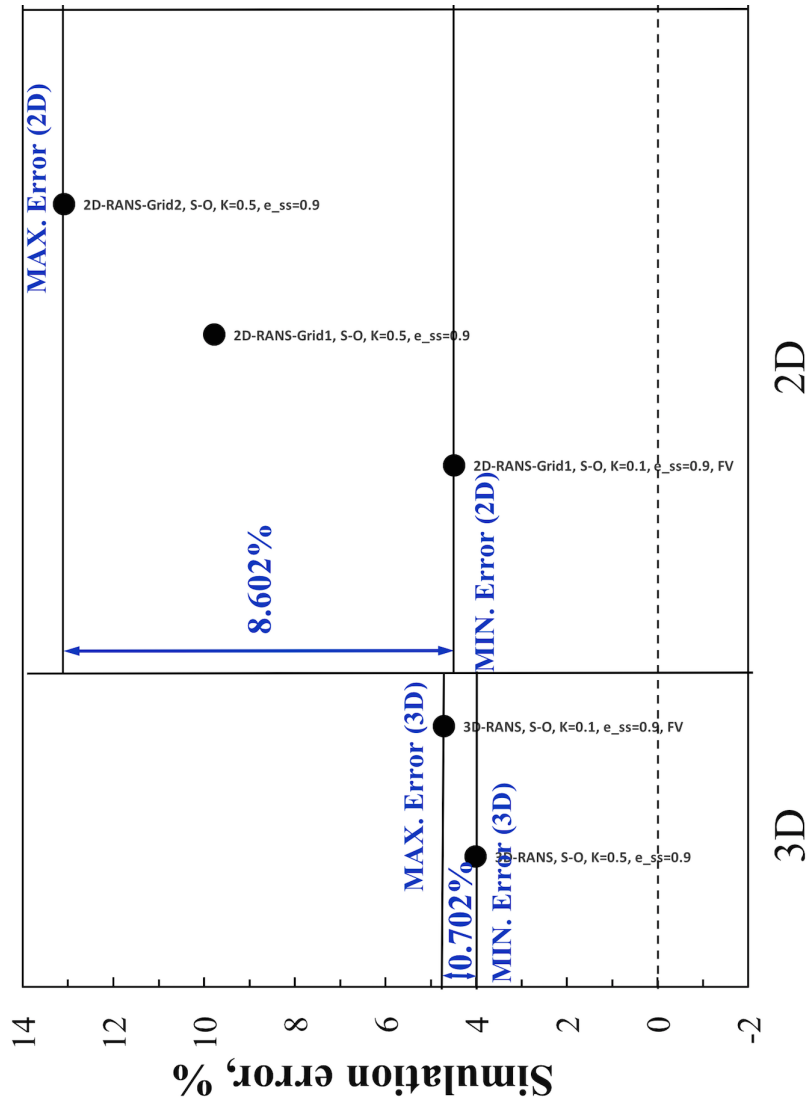


Figure 2.22: Simulation errors for 3D and 2D models at  $U = 0.46m/s$

## 2.5 Minimum Fluidization Velocity

According to the Geldart classification of powders[64], the particle contained in the fluidized bed with diameter between 250-300  $\mu m$  can be classified as Group B. For Geldart group B particles, gas bubbles appear as the minimum fluidization velocity is reached[5]. When the superficial gas velocity exceeds the minimum fluidization velocity of the system, all the particles are supported by the gas phase, and consequently the fluidization regime is formed[5]. Therefore, the measurement of the minimum fluidization velocity is important.

The minimum fluidization velocity of the bed can be determined either by experiment measurements or by employing the theoretical equations[5]. The experimental investigations are expensive and time-consuming, some necessary equipment might not readily available as well. In comparison, the theoretical prediction of minimum fluidization velocity is more convenient and adaptable. For this purpose, we use equations to estimate the value of minimum fluidization velocity[5]. The physical properties of the fluidized bed system are required for the theoretical equations. In this case, all necessary parameters are adapted from the experiment carried out by Taghipour [8].

There are four different packing structures of uniformly packed spheres in the fluidized bed: cubic, orthohombic, tetragonal-spheroidal, and rhombohedral [5]. The voidage of packing ( $\varepsilon$ ) is corresponding to the packing structure and shown in Table 2.5.

Packing	Voidage, $\varepsilon$
Cubic	0.4764
Orthohombic	0.3955
Tetragonal-Spheroidal	0.3019
Rhombohedral	0.2595

Table 2.5: Correspondence of packing structure and voidage, adapted from [5]

Consequently, the voidage at the minimum fluidization is [5]

$$\varepsilon_{mf} = \frac{6 - \pi}{6} = 0.476 \quad (2.3)$$

Based on the Carmon equation [5],

$$\frac{\Delta P}{L} = \frac{180(1 - \varepsilon)^2 \mu U}{g \varepsilon^3 d_p^2} = \frac{5(1 - \varepsilon)^2 \mu U}{g \varepsilon^3 (V_p/S_p)^2} \quad (2.4)$$

Where  $\Delta P$  represents the pressure drop in cake,  $L$  represents the thickness of

cake. we have [5],

$$\frac{\Delta P}{L} = 459 \frac{\mu U_{mf}}{d_p^2} \quad (2.5)$$

The pressure drop can support the particles weight when minimum fluidization achieved. Consequently [5]:

$$\frac{\Delta P}{L} = (\rho_p - \rho_f)(1 - \varepsilon_{mf}) \quad (2.6)$$

By combining Eqs.2.5 and 2.6, we obtain the minimum fluidization velocity

$$U_{mf} = 0.00114 \frac{gd_p^2(\rho_p - \rho_f)}{\mu} \quad (2.7)$$

Where  $g$  is the gravitational acceleration,  $d_p$  is the diameter of solid particle, and  $\mu$  is the fluid viscosity.  $\rho_p$  and  $\rho_f$  represent the density of particle and fluid, respectively. The minimum fluidization velocity for our case is calculated as  $U_{mf} = 0.1181m/s$ .

To confirm the the minimum fluidization velocity calculated by the theoretical equations, the numerical prediction of minimum fluidization velocity is comprehensively investigated. The computed volume averaged solid velocity based on 2D and 3D models as the function of time are displayed in Fig.2.23 a and b, respectively. With the increase of the superficial gas velocity from 0.125 m/s to 0.2 m/s, the increase of solid velocity can be observed from both 2D and 3D models. Overall, the 3D models give lower value of solid velocity as compared to the 2D models. For 2D models, the averaged solid velocity are 0.03, 0.075, and 0.125  $m/s$  for  $U_{gas}=0.125$ , 0.15, and 0.2  $m/s$ . For the 3D models, the averaged solid velocity are 0.02, 0.07, and 0.085  $m/s$  for  $U_{gas}=0.125$ , 0.15, and 0.2  $m/s$ . The main possible reason is the loss of extra friction as the increasing of contact area between fluid and walls. The solid velocity displays sharp fluctuations for  $U_{gas} = 0.15m/s$  and  $U_{gas} = 0.2m/s$ , while a smooth trend is depicted by  $U_{gas} = 0.125m/s$ . The mixing rate of particles is promoted as intensified gas bubbles coalescence and moving up through the solid packing. Consequently, the volume-averaged solid velocity trend shows an unstable fluctuation for high superficial gas velocity. However, if the superficial velocity does not reach the minimum fluidized bed velocity, no bubbles can be observed and particles keep resting state in the bed. Consequently, a relatively constant trend of solid velocity appears.

To gain insight into the hydrodynamics of the fluidized bed model at specific time, snapshots of the solid volume fraction in 2D and 3D models are shown in

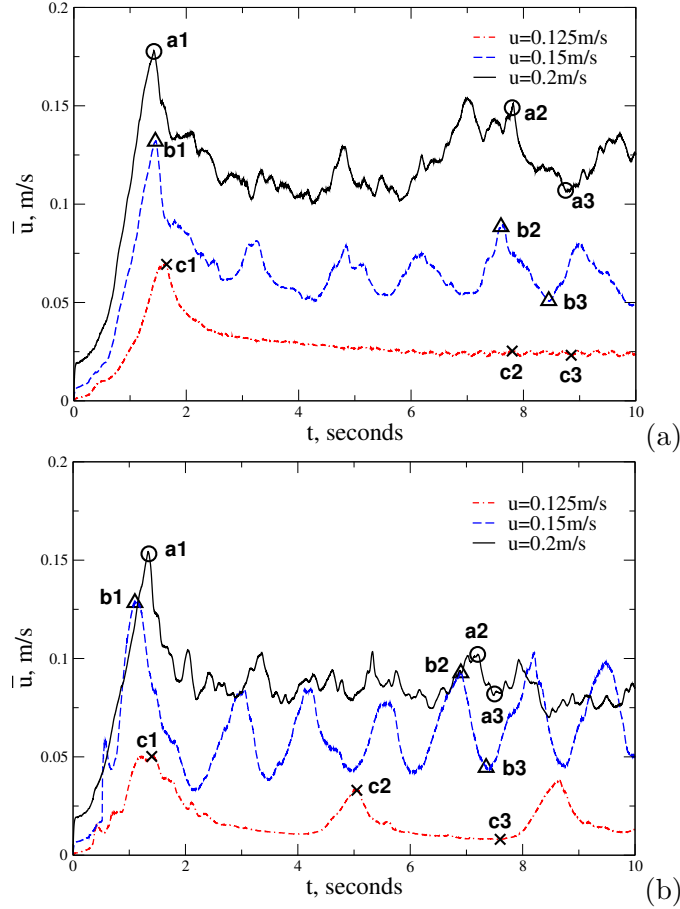


Figure 2.23: Volume averaged solid velocity as a function of time for (a) 2D-Grid 1 and (b) 3D models: (S-O)  $K = 0.1$ ,  $e_{ss} = 0.90$ .

Fig. 2.24 and 2.25, respectively. The solid volume fraction is present by slice in 2D model, while it presents both in slice and iso-surface in 3D model. We chose three specific points at each superficial gas velocity in Fig.2.23. Point 1 represents the maximum solid velocity at start up phase. Points 2 and 3 represent the maximum and minimum solid velocity at dynamic steady state. For both 2D and 3D models, more gas bubbles appear at maximum solid velocity (see a2, b2, and c2), while the minimum value of solid velocity is shown with less or even no bubbles (see a3, b3, and c3). This confirms that the increase of solid velocity leads to the increase of bubble quantity in the fluidized bed. With the decrease of superficial gas velocity from 0.2 to 0.15  $m/s$ , less bubbles can be observed (see b(1-3)). When the superficial gas velocity continuously decreases to 0.125  $m/s$ , there are no bubbles generated in the dynamic steady state for the 2D model, and negligible quantity of bubbles for the 3D model (see c(1-3)). Therefore, based on the numerical results from 2D and 3D

models, the minimum fluidization velocity is predicted as 0.125 m/s. The deviation of the numerical prediction against the theoretical prediction is 5.52%, which is within the acceptable range.

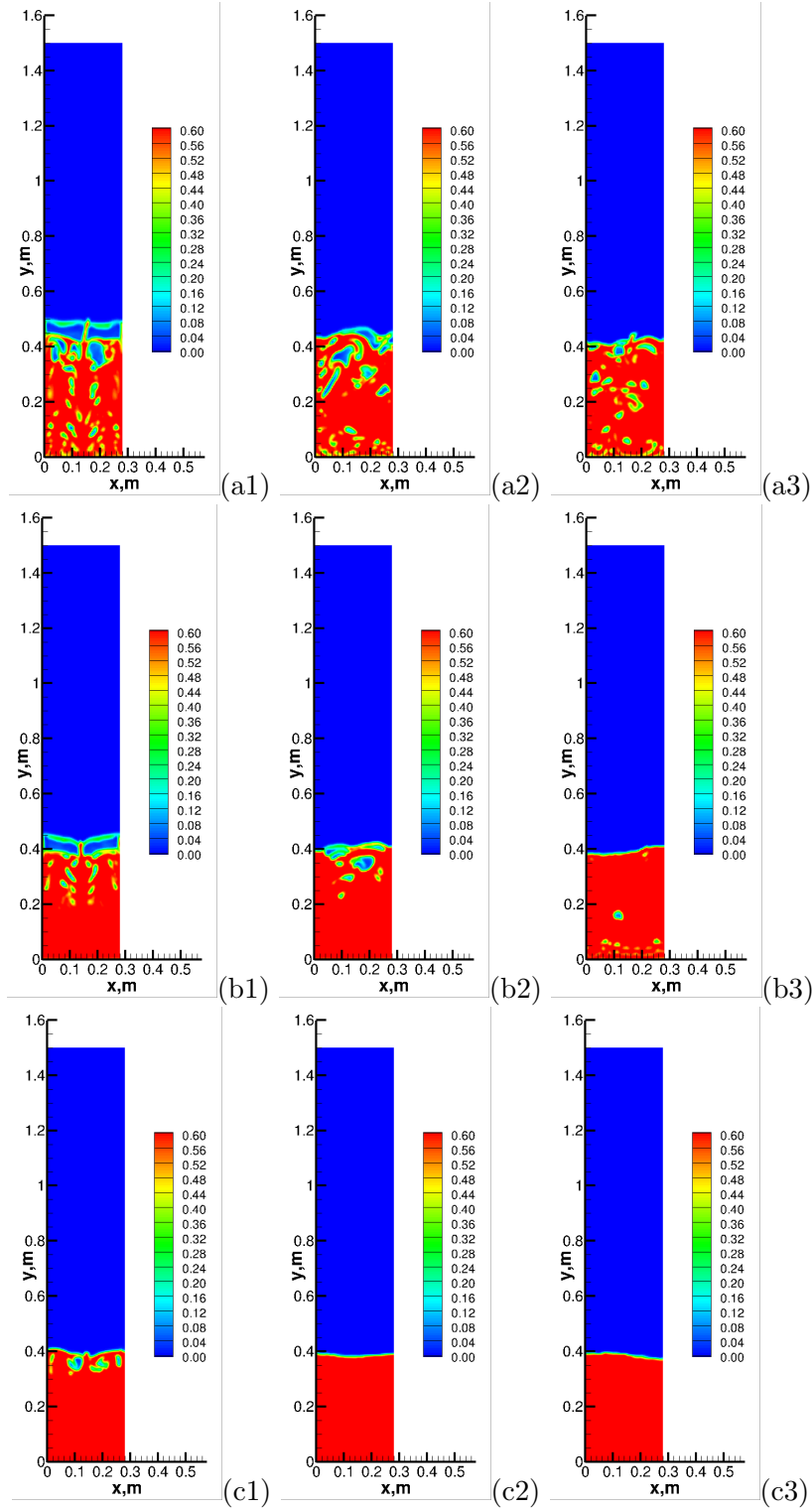


Figure 2.24: 2D-RANS : Solid volume fraction calculated using unsteady E-E model:  $K=0.1$ ,  $e_{ss}=0.9$ : (a1)  $U=0.2\text{m/s}$ ,  $t=1.425\text{s}$  (a2)  $U=0.2\text{m/s}$ ,  $t=7.8\text{s}$  (a3)  $U=0.2\text{m/s}$ ,  $t=8.75\text{s}$  (b1)  $U=0.15\text{m/s}$ ,  $t=1.45\text{s}$  (b2)  $U=0.15\text{m/s}$ ,  $t=7.6\text{s}$  (b3)  $U=0.15\text{m/s}$ ,  $t=8.45\text{s}$  (c1)  $U=0.125\text{m/s}$ ,  $t=1.65\text{s}$  (c2)  $U=0.125\text{m/s}$ ,  $t=7.8\text{s}$  (c3)  $U=0.125\text{m/s}$ ,  $t=8.85\text{s}$

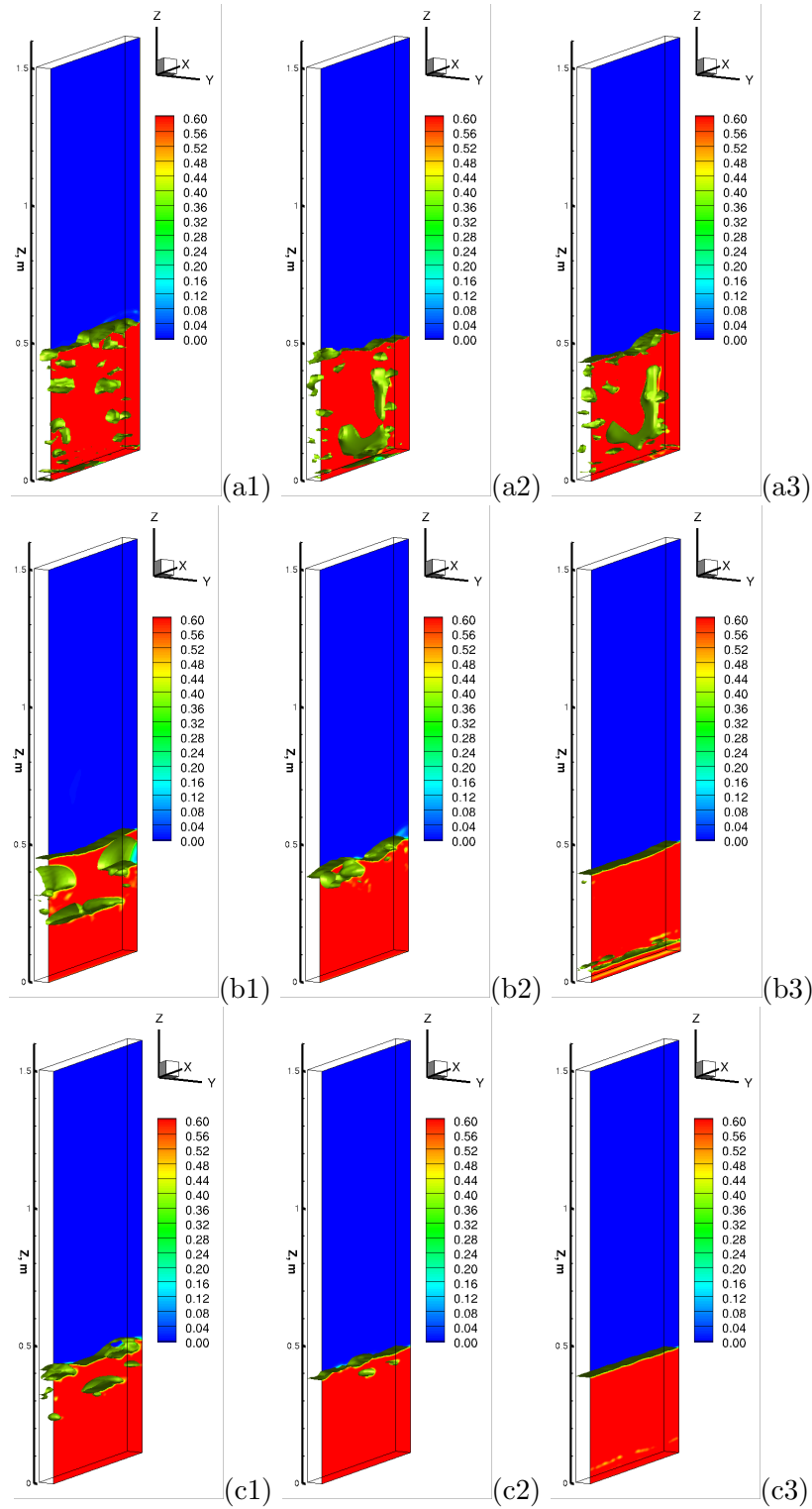


Figure 2.25: 3D-RANS , Solid volume fraction calculated using unsteady E-E model:  $K=0.1$ ,  $e_{ss}=0.9$ : (a1)  $U=0.2\text{m/s}$ ,  $t=1.35\text{s}$  (a2)  $U=0.2\text{m/s}$ ,  $t=7.2\text{s}$  (a3)  $U=0.2\text{m/s}$ ,  $t=7.5\text{s}$  (b1)  $U=0.15\text{m/s}$ ,  $t=1.1\text{s}$  (b2)  $U=0.15\text{m/s}$ ,  $t=6.9\text{s}$  (b3)  $U=0.15\text{m/s}$ ,  $t=7.35\text{s}$  (c1)  $U=0.125\text{m/s}$ ,  $t=1.4\text{s}$  (c2)  $U=0.125\text{m/s}$ ,  $t=5.05\text{s}$  (c3)  $U=0.125\text{m/s}$ ,  $t=7.6\text{s}$

## 2.6 Classification of Fluidization Regimes

As long as solid particles are fluidized, different fluidized bed behaviors can be observed with varied superficial gas velocity. Fig.2.26 shows three distinguishable regimes of fluidization observed numerically: minimum fluidization, bubbling fluidization, and turbulent fluidization. When the superficial gas velocity reaches the minimum fluidization velocity, no bubbles can be observed, instead the bed surface fluctuates slightly. This is called minimum fluidization (Fig.2.26a). The readily identifiable bubbles appears when the gas velocity is increased beyond the minimum fluidized velocity. The gas bubbles undergo the formation, rise, coalescence, and burst promotes the solid mixing and increase the bed expansion. At this point, a bubbling fluidization is formed as shown in Fig.2.26b. When the gas velocity increases further, the intensified coalescence and breakup of bubbles contribute to the continuously increase of bubble size and bed expansion. Consequently, the bed surface is considerably diffused. Such regime is referred to as turbulent fluidization (Fig.2.26c).

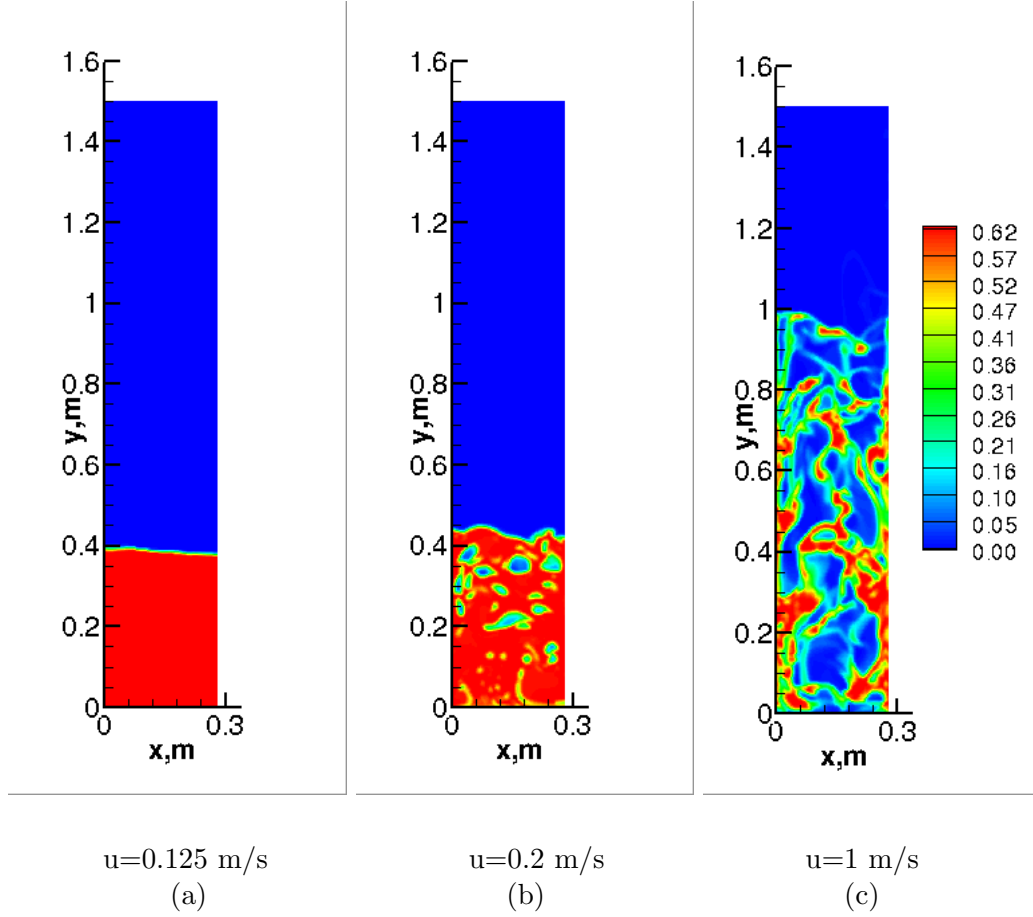


Figure 2.26: Snapshots of solid volume fraction in different regimes at  $t=20 \text{ s}$ ,  $K = 0.1$ ,  $e_{ss} = 0.8$ : (a) Minimum fluidization (b) Bubbling bed (c) Turbulent bed

$U, \text{m/s}$	$U/U_{mf}$
0.125	1.058
0.15	1.270
0.2	1.693
1	8.467

Table 2.6: The relation between superficial gas velocity,  $U$  and minimum fluidization velocity,  $U_{mf}$

## 2.7 Conclusions

The numerical simulations of fluidized bed filled with Geldart Group B particles using 2D and 3D approaches were validated by the CFD commercial software, Fluent 16.2. The comparison of numerical and experimental data available in the

literature by Taghipour [8] showed that 3D and 2D approaches give a deviation of time-averaged void fraction within [4.01-6.50]% and [4.48-13.08]%, respectively. The combination of E-E model parameters such as specular coefficient characterising particle-wall interaction, numerical grid resolution and discretisation scheme for convective terms can give results close to experimental data. Results of 2D and 3D simulation revealed that the turbulence has less influence on the fluidized bed structure but significant influence on the gas phase velocity in the upstream region of a reactor. The use of RANS model provides slightly better agreement with experimental data in comparison with results given by a Laminar model. The voidage distribution inside the bed is sensitive to the specular coefficient in comparison to the restitution coefficient. The minimum fluidization velocity was predicted as 0.125 m/s by 2D and 3D approach, which in good agreement with theoretical calculation, 0.118 m/s. Finally, our model used in this work presented three different fluidization regimes: minimum fluidization, bubbling fluidization, and turbulent fluidization.

## Chapter 3

# The Impact of Heterogeneous Reactions on Fluidized Bed Regimes

This chapter is devoted to numerical studies of the influence of heterogeneous reactions, e.g.  $C + CO_2$ , on the dynamics of the fluidized bed considered in previous section. In particular, coal or biomass gasification in a fluidized bed is considered as an example.

### 3.1 Benchmark Experiments

Before we proceed with the model description we want to highlight the basic experimental works on coal/biomass gasification.

The 3D CFD model was applied to simulate the coal gasification in a pressurized spout-fluid bed (see Fig.3.1) by Deng[13]. The combination of Arrhenius rate and diffusion rate were used to determine the rate of heterogeneous reactions. The homogeneous reactions were considered as secondary reactions. The modeling results show that the maximum temperature of 1510 °C is distributed in the central jet close to the outlet of nozzle. Endothermic gasification reactions caused gradual temperature drop along the reactor. Carbon dioxide reached maximum concentration in the range [13.97-25.6]% at the basis of the reactor. The gasification reaction rates decrease with the decrease of solids concentration and temperature. Consequently, the variation of molar fraction of gas compositions in freeboard were not obvious. Both pressure and temperature had significant influence on the coal gasification performance. With the increase of the operating pressure from atmospheric pressure

to 0.3 MPa, the outlet molar fractions of  $CO$ ,  $H_2$ , and  $CH_4$  increased [1-2.45]%. The increase of bed temperature from 884 to 912°C led to a decline of 2.79% for  $H_2$ , 1.27% for  $CH_4$  and 0.97% for  $CO$ .

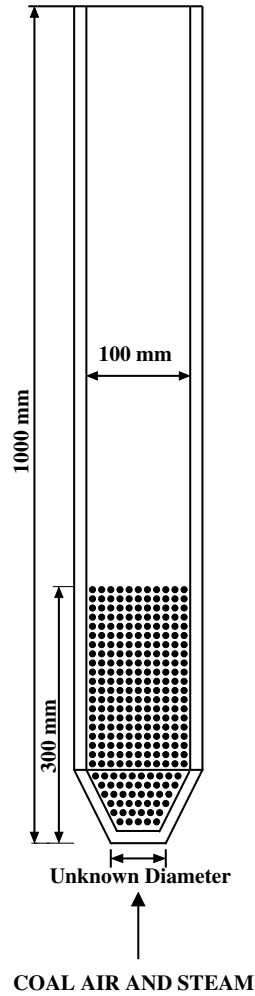


Figure 3.1: Schematic of a pressurized spout-fluid bed, adapted from [13]

Xie [65] used E-L model based on the multiphase particle-in-cell (MP-PIC) method to simulate the coal gasification in a 3D fluidized bed gasifier at atmospheric pressure. The numerical prediction shows a good agreement with experiment with a average relative error of 15%. From the numerical results, the overall trend of  $CO_2$ ,  $CO$ ,  $H_2$ ,  $CH_4$ , and  $N_2$  molar fraction distributions is consistent under different operation conditions. The concentration distribution of  $CO$  and  $CO_2$  are opposite in the reactor. The consumption of carbon particle increase with 0.0098 kg/s within 32.5 seconds. Higher temperature in the range [1030-1070]C can be observe in the dense phase region, while the lower temperature between 949 to 990 exists in the

freeboard region. This can be explained by the direct contact between gasifying agent and coal.

From the research of [66], a 3D model was developed to simulate the coal gasification in a fluidized bed gasifier. Arrhenius-Eddy dissipation reaction rate and Arrhenius-diffusion reaction rate were used to determine the homogeneous and heterogeneous reaction rates, respectively. The 3D model shows a good agreement with experiment data with the deviation in the range [1-25]%. The obvious fluctuations of solid and gas phase in the range [0-1.75] m/s and [0-3.5] m/s can be observed below  $z=0.75$  m. The lower concentration of  $CO_2$  in the range [0.62-5.73]% is distributed at the bottom of the reactor due to the existence of high quantity of solid. The higher concentration of  $CH_4$  in the range [2-3.38]% exists in the low region of the reactor due to the devolatilization.

Based on an E-E method, Li[67] developed a 3D CFD model to simulate the coal gasification in a pressurized spouted-fluid bed. The influences of bed temperature and operating pressure on numerical results were investigated. The simulation prediction shows that the volume fraction of  $CO_2$  increases 1% while the decrease trend of volume fraction of  $CO$  is less than 1% as the air/coal ratio increases from 1.65 to 1.82. With the increase of bed pressure from 0.1 to 0.5 MPa, the improved quantity of  $CO$ ,  $CO_2$ ,  $H_2$ , and  $CH_4$  in the gasifier in the range [1-3]% can be observed. The errors between the predicted volume fraction of  $CO$ ,  $CO_2$ , and  $H_2$  and experiment measurement are within the range of 10%. Whereas a large deviation between 14.8 and 25.8% is shown by volume fraction of  $CH_4$ .

Ku [68] used E-L approach to simulate the biomass gasification in a 2D fluidized bed reactor model. The gasification performance were analyzed based on the effect of different reactor temperature, steam/biomass mass ratio and biomass injection position. The results shows that the concentration of  $CO$  and  $H_2$  increases 3% and 1% with the increase of reactor temperature from 820 C to 920 C. With the increase of steam/biomass ratio from 0.8 to 1.4, the gas volume fraction of  $H_2$  increases 3% while that of  $CO$  decreases 5%. The carbon conversion rate decreases from 95.3% to 86.7% with the increase height of biomass injection position from bottom feed point to  $Z=0.6$  m point.

To investigate the biomass gasification process in a fluidized be system, Loha [14] used E-L approach to simulate a bubbling fluidized bed biomass gasifier (see Fig.3.2). The influence of gasification temperature, equivalence ratio and steam-to-biomass ratio on gas composition are discussed in this study. The modeling prediction indicated that with the increase of temperature from 800 C to 900 C, the mole fraction of  $CO$  and  $H_2$  increaese 5.2% and 4.8%, respectively. The concentrations of  $CO$  and

$H_2$  decrease 2.8% and 3.1% with the increase of equivalence ratio from 0.30 to 0.40.  $H_2$  is more sensitive to the choice of steam/biomass ratio as compared to the  $CO_2$ ,  $CO$ ,  $CO_2$ ,  $CH_4$ , and  $N_2$ . The mole fraction of  $H_2$  increase 5.5% with the increase of steam/biomass ratio from 0.2 to 0.8.

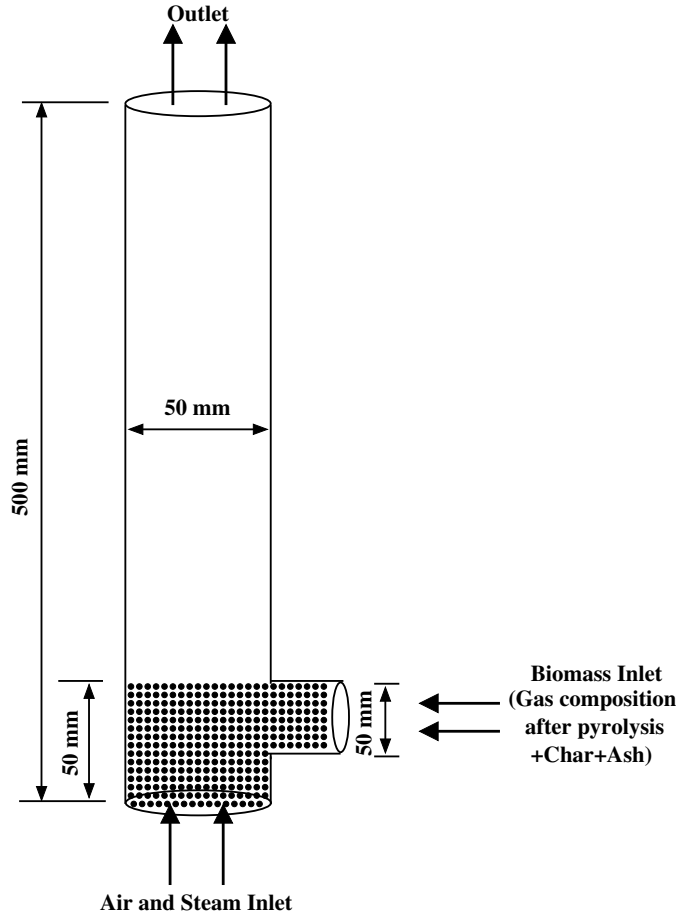


Figure 3.2: Schematic of a bubbling fluidized bed, adapted from [14]

Xue [69] established a 2D model to simulate the biomass gasification with E-E approach in a fluidized bed reactor. The effects of air/biomass mass flow ratio, reactor temperature and biomass moisture content, were investigated in this study. The simulation prediction showed that the biomass particles transformed into char and gas species rapidly. With the increase of air/biomass mass flow ratio from 0.4 to 2.1, the 10% decrease of concentration of  $CO$  can be observed. This can be explained by the high  $CO$  oxidation contributed by rich oxygen as increase of gas flow rate. With the increase of the temperature from 1000 to 1200 K, both  $CO$  and  $CO_2$  increase 4% and 1%, respectively. The concentration of tar decreases from 4%

to 2.5% suggesting that most char are converted in the high reactor temperature. The three product (Tar, char, and gas) shows a constant trend of mass fraction with the increase of moisture content from 15% to 25%.

Xie [15] used E-L approach to simulate combustible solid waste gasification in a 3D cylindrical spout bed (see Fig.3.3). The model shows a 15% mean relative error against experiment. The development of gas-solids flow regimes can be observed at high operating temperature ( $T_r = 700C$ ). The chemical reaction at high temperature leads to an unstable regime after dynamic steady state is achieved. With the increase of equivalence ratio from 0.20 to 0.24, the decrease of combustible gas can be observed due to the high oxidation reaction rate. The combustion and heat transfer lead to an increase of temperature from  $573K$  to  $900K$  in the spout zone. The mixing of wood and sand particles contributes to a uniform distribution of temperature in the annulus and foundation regions. Higher concentration of  $CO$  can be found in the annulus zone with intensified combustion and gasification reactions. The combustion reactions contribute to a high concentration of  $CO_2$  in the upper part of the freeboard zone.

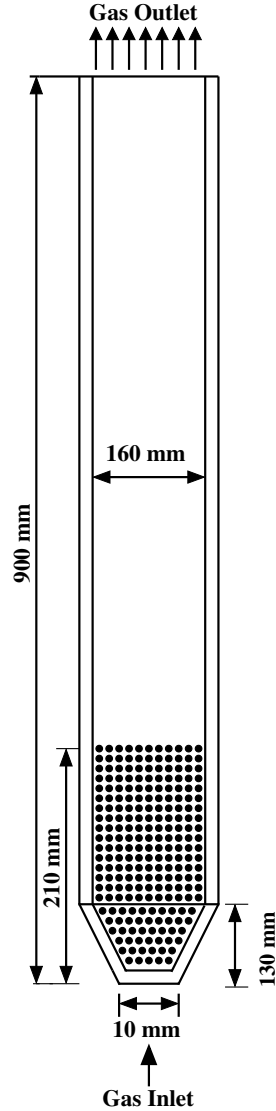


Figure 3.3: Schematic of a spout-fluid Bed, adapted from [15]

The gasification performance of forestry residues was studied by [70] in a 3D fluidized bed reactor with the E-L approach. The effects of reactor temperature, equivalence ratio and steam to biomass ratio on product gas composition and carbon conversion efficiency were investigated. From the numerical results, increasing temperature from 700 to 900 C leads the 5% decrease of volume fraction of  $CH_4$  and 2% decrease of  $CO$ . The carbon conversion efficiency increases from 86% at 700 C to 93% at 900 C. The volume fraction of  $CH_4$  and  $CO$  decreases slightly with the increase of equivalence ratio from 0.21 to 0.25 and steam biomass ratio from 1.3 to 2.7. However, the carbon carbon conversion efficiency increases 3% with the

increase of equivalence ratio but decreases 2% when steam to biomass ratio increase. The molar fraction distributions of each gas compositions is relatively consistent in various operation conditions. The existence of large amount of carbon contribute a highest molar fractions of  $CO$ , 33.9%, distributed at the inlet region.

## 3.2 Model Formulation

The computational geometry of fluidized bed is adapted from a validation case in last chapter [8]. After establishment of the basic gas-solid flow model without chemical reaction, the existing model was adjusted to account for gasification conditions. The adjusted numerical setups are illustrated in Table 3.1. The governing equations are presented in Table 3.2.

Table 3.1: Simulation setups for gasification case

Multiphase flow model	k- $\varepsilon$ model
Drag submodel	Syamlal-O'Brien
Granular viscosity	Syamlal-O'Brien
Frictional viscosity	Johnson et. al.
Solid pressure	Syamlal-O'Brien
Restitution coefficient	$e_{ss} = 0.9$
Specularity coefficient	$K = 0.1$
Maximum packing limit	$\alpha_{max} = 0.61$

The inflow velocity and operating reactor temperature are two important operating parameters affecting the performance of the coal gasification. In this research, the numerical model is enhanced for the investigated coal. The inlet velocity is set to  $0.38m/s$ ,  $0.46m/s$ , and  $0.9m/s$  for each case. Initially, the operating reactor temperature is set as  $1100K$  for the beginning 20 seconds. After that, the simulation continuous runs 20 seconds with increased temperature of  $1500K$ . The gas phase is initially filled with 99% of  $CO_2$  and 1%  $N_2$ . The packed bed is composed of coal particle with a average diameter of  $275 \mu m$ . As long as the mixture gas is injected into the reactor, coal will react with carbon dioxide and converted into carbon monoxide. This reaction is endothermic heterogeneous reaction and it is assumed and modeled using Fluent phase interaction reaction panel:



At first, the heterogeneous reaction rate is estimated based on a simple Arrhenius model implemented in Fluent. However, that low carbon conversion rates and un-

derestimated surface of the reaction particles were caused by the Arrhenius model. Consequently, a surface-based user-defined function (UDF) was used to program the heterogeneous reaction rate equations of coal gasification. The surface-based reaction model assumes that the heterogeneous reaction takes part at the particle surface. The gases ( $CO_2, H_2O, O_2$ ) cannot penetrate into the particle. The UDF is adapted from ANSYS Fluent database. The overall particle reaction is controlled by kinetic rate that is based on an Arrhenius rate model:

$$k_{kin} = AT_s^{n_t} \exp(-E_A/R_u T_s) \quad (3.2)$$

where  $A$  is the pre-exponential factor,  $E_A$  is the activation energy, and  $n_t$  represents the temperature exponent of the reaction. The values of  $A$ ,  $E_A$ , and  $n_t$  are 3.92,  $2.239 * 10^8 J/kmol$ , and 0 that are adapted from Deng[13].

Name	Equation
Continuity equation	$\frac{\partial}{\partial t}(\alpha_g \rho_g) + \nabla \cdot (\alpha_g \rho_g \vec{v}_g) = S_{gs}$ $\frac{\partial}{\partial t}(\alpha_s \rho_s) + \nabla \cdot (\alpha_s \rho_s \vec{v}_s) = S_{gs}$ $S_{gs} = -S_{gs} = M_c \sum \gamma_c R_c$
Gas density	$\frac{1}{\rho_g} = \frac{RT}{p} \sum_{i=1}^n \frac{Y_i}{M_i}$
Solid mixture density	$\rho_s = \sum_{i=1}^m \frac{Y_i}{\rho_i}$
Momentum equations for gas phase	$\frac{\partial}{\partial t}(\alpha_g \rho_g \vec{v}_g) + \nabla \cdot (\alpha_g \rho_g \vec{v}_g \vec{v}_g) = -\alpha_g \nabla p_g + \nabla \cdot \overline{\overline{\tau}}_g + \alpha_g \rho_g \vec{g} - \beta(\vec{v}_g - \vec{v}_s) + S_{gs} U_s$ $Re_s = \frac{\rho_g \alpha_g \bar{v}_g - \bar{v}_s  d_s }{\mu_g}$ $\tau_g = \mu_g [\nabla \nu_g + \nabla \nu_g^T] - \frac{2}{3} \mu_g (\nabla \cdot \nu_g) I$ $\mu_g = \mu_{gl} + \mu_{gt}$ $\mu_{gt} = \rho_g C_{\mu} \frac{k^2}{\varepsilon}$ $C_{\mu} = 0.09$
Momentum equations for solid phase	$\frac{\partial}{\partial t}(\alpha_s \rho_s \vec{v}_s) + \nabla \cdot (\alpha_s \rho_s \vec{v}_s \vec{v}_s) = -\alpha_s \nabla p_s + \nabla \cdot \overline{\overline{\tau}}_s + \alpha_s \rho_s \vec{g} - \beta(\vec{v}_g - \vec{v}_s) + S_{sg} U_s$ $g_0 = [1 - (\frac{\alpha_s}{\alpha_{s,max}})]^{1/3} - 1$ $\frac{\partial}{\partial t}(\alpha_s \rho_s \Theta) + \nabla \cdot (\alpha_s \rho_s \Theta \vec{v}_s) = \frac{2}{3} [(-p_s I + \tau_s) : \nabla \nu_s + \nabla \cdot (\Gamma \Theta \nabla \Theta)] - \gamma_s + \phi_s + D_{gs}$ $\gamma_s = 3(1 - e^2) \alpha_s^2 \rho_s g_0 \Theta (\frac{4}{d_s} \sqrt{\frac{\Theta}{\pi}} - \nabla \cdot \nu_s)$ $\phi_s = -3\beta \Theta$ $\tau_s = [(-p_s + \xi_s \nabla \cdot \nu_s) + \mu_s [\nabla \nu_s + (\nabla \nu_s)^T] - \frac{1}{3} (\nabla \cdot \nu_s) I]$ $\mu_s = \frac{4}{5} \alpha_s^2 \rho_s d_s g_0 (1 + e) \sqrt{\frac{\Theta}{\pi}} + \frac{10 \rho_s d_s \sqrt{\pi \Theta}}{96(1+e) \alpha_s g_0} [1 + \frac{4}{5} \alpha_s g_0 (1 + e)]^2 - \frac{p_s \sin \theta}{2\sqrt{I_2 D}}$
Energy balance equations	$\frac{\partial}{\partial t}(\alpha_g \rho_g H_g) + \nabla \cdot (\alpha_g \rho_g \vec{v}_g H_g) = \nabla \cdot (\lambda_g \nabla T_g) + h_{gs}(T_g - T_s) + S_{gs} H_s$ $\frac{\partial}{\partial t}(\alpha_s \rho_s H_s) + \nabla \cdot (\alpha_s \rho_s \vec{v}_s H_s) = \nabla \cdot (\lambda_s \nabla T_s) + h_{sg}(T_s - T_g) + S_{sg} H_s$ $H = \sum_j Y_j H_j$ $\lambda_g = \sum_j \frac{X_j \lambda_j}{\sum_j X_j \bar{O}_{ij}}$ $\bar{O}_{ij} = \frac{[1 + (\frac{\mu_i}{\mu_j})^{0.5} (\frac{M_j}{M_i})^{0.25}]^2}{[8(1 + (\frac{M_i}{M_j}))]^{0.5}}$ $h_{sg} = \frac{6 \lambda_g \alpha_g \alpha_s N u_s}{d_s^2}$ $N u_s = (7 - 10 \alpha_g + 5 \alpha_s^2)(1 + 0.7 Re_s^{0.2} Pr^{1/3} + (1.33 - 2.4 \varepsilon_g + 1.2 \alpha_g^2) Re_s^{0.7} Pr^{1/3})$
Species transport equations	$\frac{\partial}{\partial t}(\rho \alpha Y_i) + \nabla \cdot (\rho \alpha Y_i \nu) = -\nabla \cdot \alpha J_i + R_i$ $J_{g,i} = -(\rho_g D_{i,m} + \frac{\mu_t}{Sc_t}) \nabla Y_{g,i}$ $Sc_t = 0.7$

Table 3.2: Model equations available by ANSYS Fluent 16.2 which were used to model the fluidized bed from [3],[4].

### 3.3 Results: The Influence of the Temperature on the Fluidized Bed Dynamics

To investigate the effect of the superficial gas velocity on the fluidization behavior, three different 2D fluidized bed models were run at the inflow velocity of 0.38 m/s, 0.46 m/s, and 0.9 m/s. Fig.3.4 shows the snapshots of solid volume fraction for cold flow model (a), gasification model with  $T=1100$  K (b) at  $t=20$  sec, and gasification model with  $T=1500$  K (c) at  $t=40$  sec. From the solid volume fraction shown in Fig. 3.4, the distribution of fluid regime is affected by the increasing superficial gas velocity. With the increase of the gas velocity, the increasing of bubble size and the thinner solid phase can be observed. For example, the biggest bubble size is  $d_p = 0.14m$  at  $U = 0.38m/s$  while the bubble diameter increased to  $0.28m$  at  $U = 0.9m/s$  for gasification model with  $T=1100$  K. The main possible reasons for this phenomenon is the intensified bubble formation, growth, and coalescence with increases of superficial velocity. In addition to the increased overall voidage, the bed height is raising with the increase of inlet velocity. This can be explained by the formation of higher drag force. As long as the inlet velocity increases, the fast motion of each particle through the fluid leads to less resistance between particle and fluid. Consequently, a higher bed height is achieved. The distribution of solid volume fraction is affected by the variation of operating reactor temperature ( $T_r$ ). The gasification reaction affects the fluid regime significantly. By comparing the solid volume fraction of cold case and gasification case with  $T= 1100$  K, an increase of bubbles quantity inside the bed can be observed. Such difference is more distinct with the superficial gas velocity increases from 0.38 to 0.9 m/s. With the increase of temperature from 1100 K to 1500 K, the further decrease of solid volume fraction and increase of bubble quantity are observed. This can be explained by the increased chemical reaction rate by the high temperature, resulting more particles convert to gas.

Fig.3.5 shows the time-averaged solid volume fraction for the cold case and gasification cases at different inlet velocities. The solid-phase distribution is affected when inlet velocity increases from  $0.38m/s$  to  $0.9m/s$  revealing that fluidization hydrodynamic is sensitive to the choice of  $U$ . With the increase of inlet velocity from  $0.38m/s$  to  $0.9m/s$ , the decrease of solid volume fraction is observed in the bed domain. For all models, the occupation of solid phase in the central region decreases from [20-45]% at  $U = 0.38m/s$  to [10-35]% at  $U = 0.9m/s$ . However, the concentration of solid phase on the wall is constant with the increase of superficial gas velocity among cold case and gasification cases. This because no matter how

fast the downward velocity near the wall region, particles fall down along the wall and form a solid layer on the wall.

To confirm the influence of gas velocity on the distribution of solid pattern, Fig. 3.6 shows the time-averaged gas velocity vector inside the entire geometry for each case with different inlet velocities. The results shows a symmetrical distribution of gas velocity in the domain. The magnitude of vector increases with the increase of inlet gas velocity from  $0.38\text{m/s}$  to  $0.9\text{m/s}$ . For  $U = 0.38\text{m/s}$  and  $U = 0.46\text{m/s}$ , the fluidizing gas velocity in the center is high and gradually decreased above the bed surface. When the fluidizing gas flows down to the bottom, it changes direction after encountering the inlet gas and the magnitude of vector decreases. Consequently, the mixture of fluidizing gas and inlet gas forms a vortex flow of gas in both sides between the center and the wall. The vortex contributes the intensely mixing of coal and carbon dioxide and enhance heat and mass transfer.

Fig3.7 and Fig3.8 shows the  $CO$  and  $CO_2$  mass fraction distributions in the reactor under operation conditions ( $U = 0.38, 0.46, 0.9\text{m/s}$ ,  $T_r = 1100, 1500\text{K}$ ). The concentration distribution of  $CO$  and  $CO_2$  are opposite in the reactor. The high value of  $CO$  and low value of  $CO_2$  can be observed from the reactor suggesting that the operation temperatures ( $T_r = 1100$  and  $1500\text{K}$ ) are high enough to produce gas product. The concentration of  $CO_2$  increase but  $CO$  decreases in the reactor when the inlet gas velocity increase from  $0.38\text{ m/s}$  to  $0.9\text{ m/s}$ . The short reaction time leads to a uncompleted chemical reaction between particle and gas. Consequently, the quantity of reactant ( $CO_2$ ) increases and production ( $CO$ ) decreases with the increases of superficial gas velocity. The concentration of gas compositions are affected by the operating reactor temperature. With the increase of the temperature from  $1100\text{ K}$  to  $1500\text{ K}$ , increase in the mass fraction of  $CO$  from the range of [5-50]% to 99% in the gas phase can be observed. The rate of gasification reaction ( $C + CO_2 \rightarrow 2CO$ ) become faster with in increase of reactor temperature, resulting the accelerated consumption of  $CO_2$  and enhanced formation of  $CO$ .

Fig.3.9 illustrates the profile of time-averaged gas temperatures in the reactor with different superficial gas velocity. The chemical reaction is endothermic gasification reaction suggesting that the system absorbs energy from its surroundings. Consequently, the temperature of system should decreases with function of time. For  $T_r = 1100\text{K}$ , there is no obvious change of the gas temperature with the increase of superficial gas velocity. The dominant temperature in the entire domain is  $1099\text{K}$ . However, the distribution of gas temperature is significantly affected by the gas velocity at  $T_r = 1500\text{K}$ . The high temperature within the range [1310-1318]K is distributed at  $U = 0.38\text{m/s}$  while low temperature  $1308\text{ K}$  is distributed

at  $U = 0.9m/s$ . From Fig.3.7, we know that the carbon monoxide is produced immediately at the bottom of the reactor with  $T_r = 1500K$ . The produced carbon monoxide will move up faster and exit from the outlet with the increase of the inlet gas velocity. In the same time, the fast motion of carbon monoxide leads less heat absorption from wall( $T_w = 1500K$ ), and Consequently the temperature in the domain is lower.

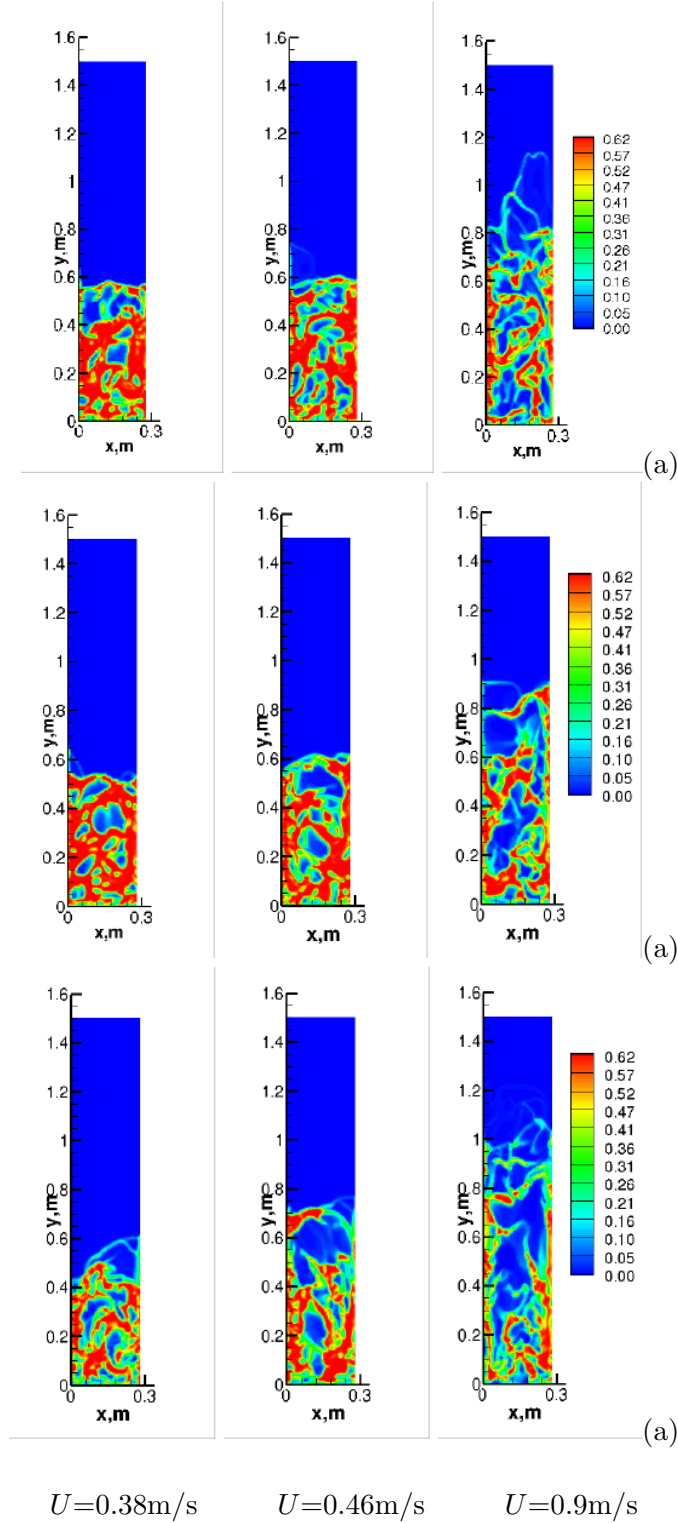


Figure 3.4: 2D-RANS: Solid volume fraction calculated using unsteady E-E model at different inflow velocities  $U$ : Grid 1, (S-O),  $K=0.1$ ,  $e_{ss}=0.9$ , (a) Cold case,  $t=20$  s, (b) Gasification case,  $T=1100\text{ K}$ ,  $t=20$  s, (c) Gasification case,  $T=1500\text{ K}$ ,  $t=40$  s.

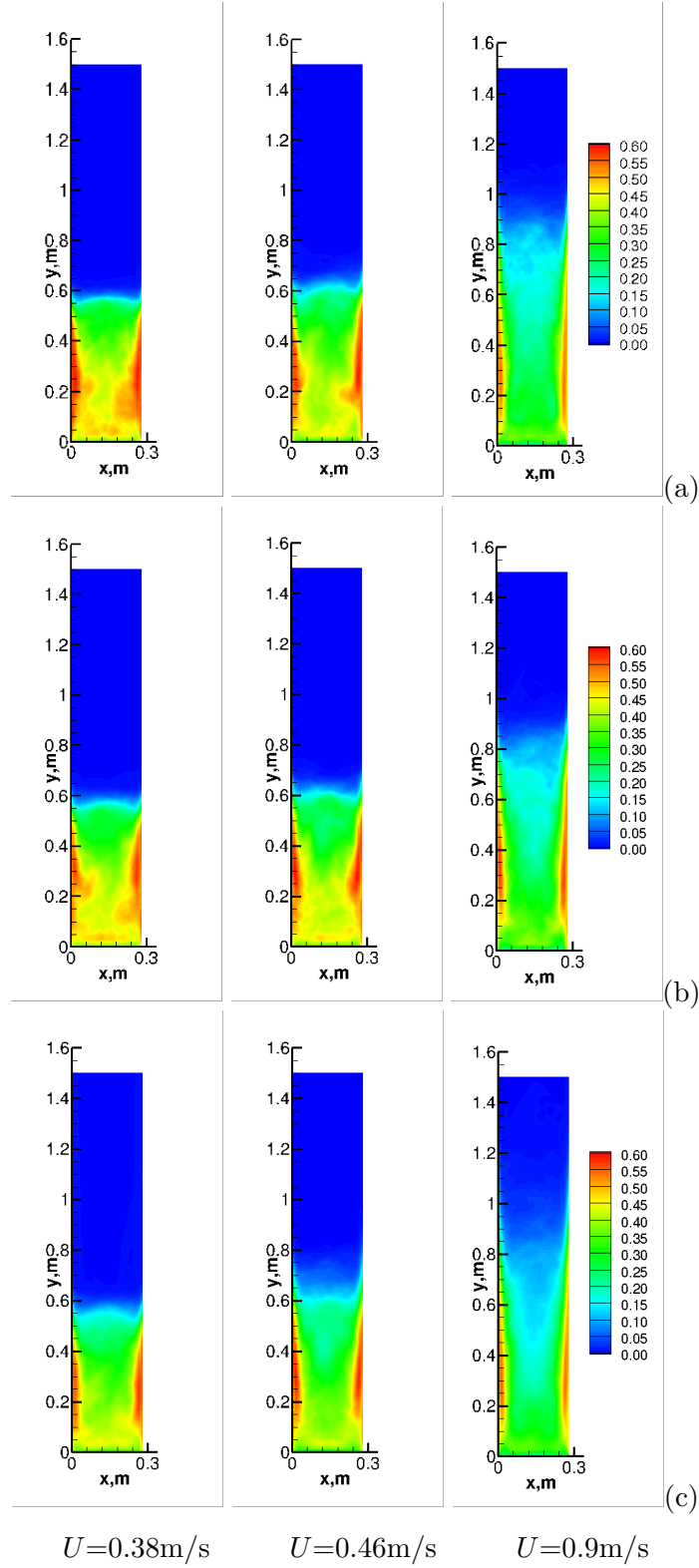


Figure 3.5: 2D-RANS: Time averaged solid volume fraction calculated using unsteady E-E model at different inflow velocities  $U$ : Grid 1, (S-O),  $K=0.1$ ,  $e_{ss}=0.9$ , (a) Cold case, (b) Gasification case,  $T=1100$  K (c) Gasification case,  $T=1500$  K

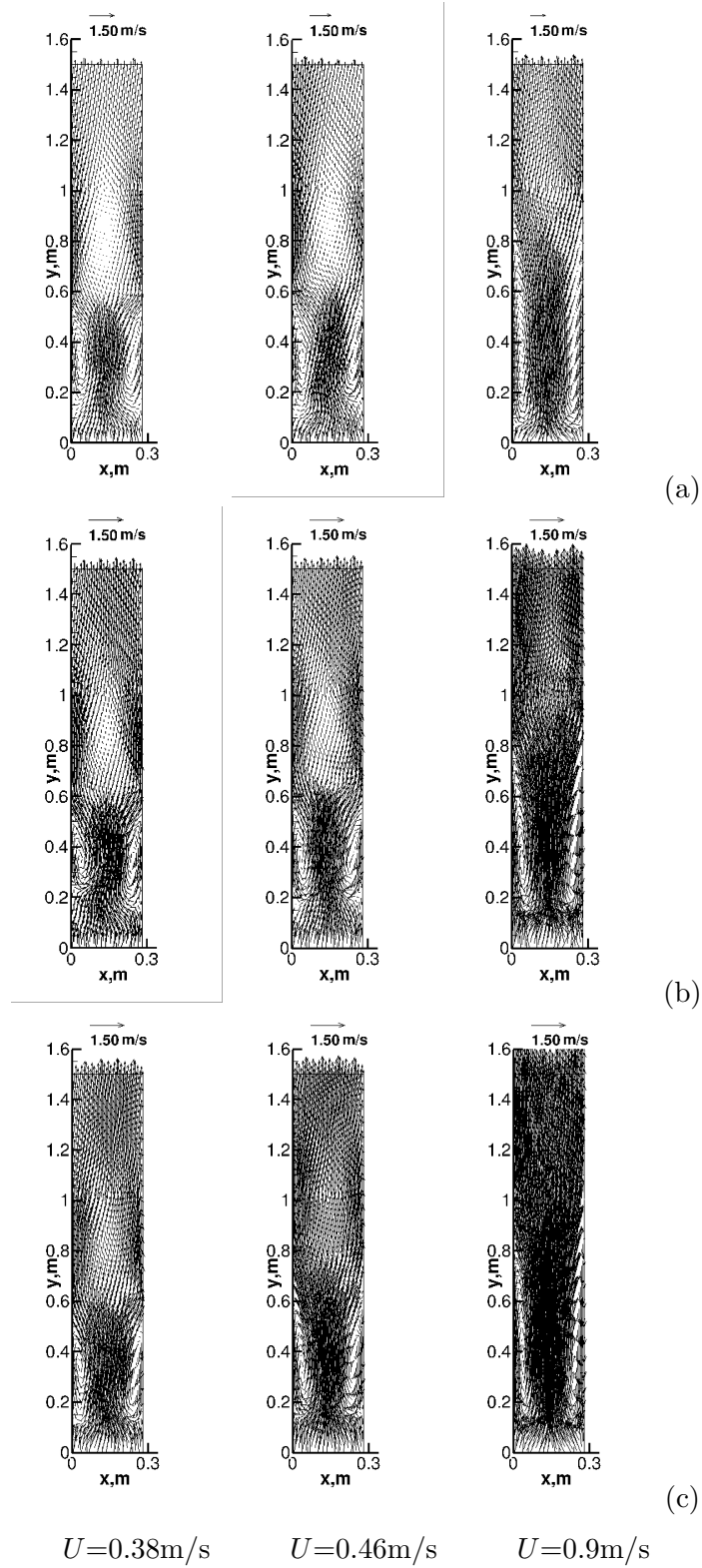


Figure 3.6: 2D-RANS: Time-averaged gas velocity vector calculated using unsteady E-E model at different inflow velocities  $U$ : Grid 1, (S-O),  $K=0.1$ ,  $e_{ss}=0.9$ , (a) Cold case (b) Gasification case,  $T=1100$  K (c) Gasification case,  $T=1500$  K

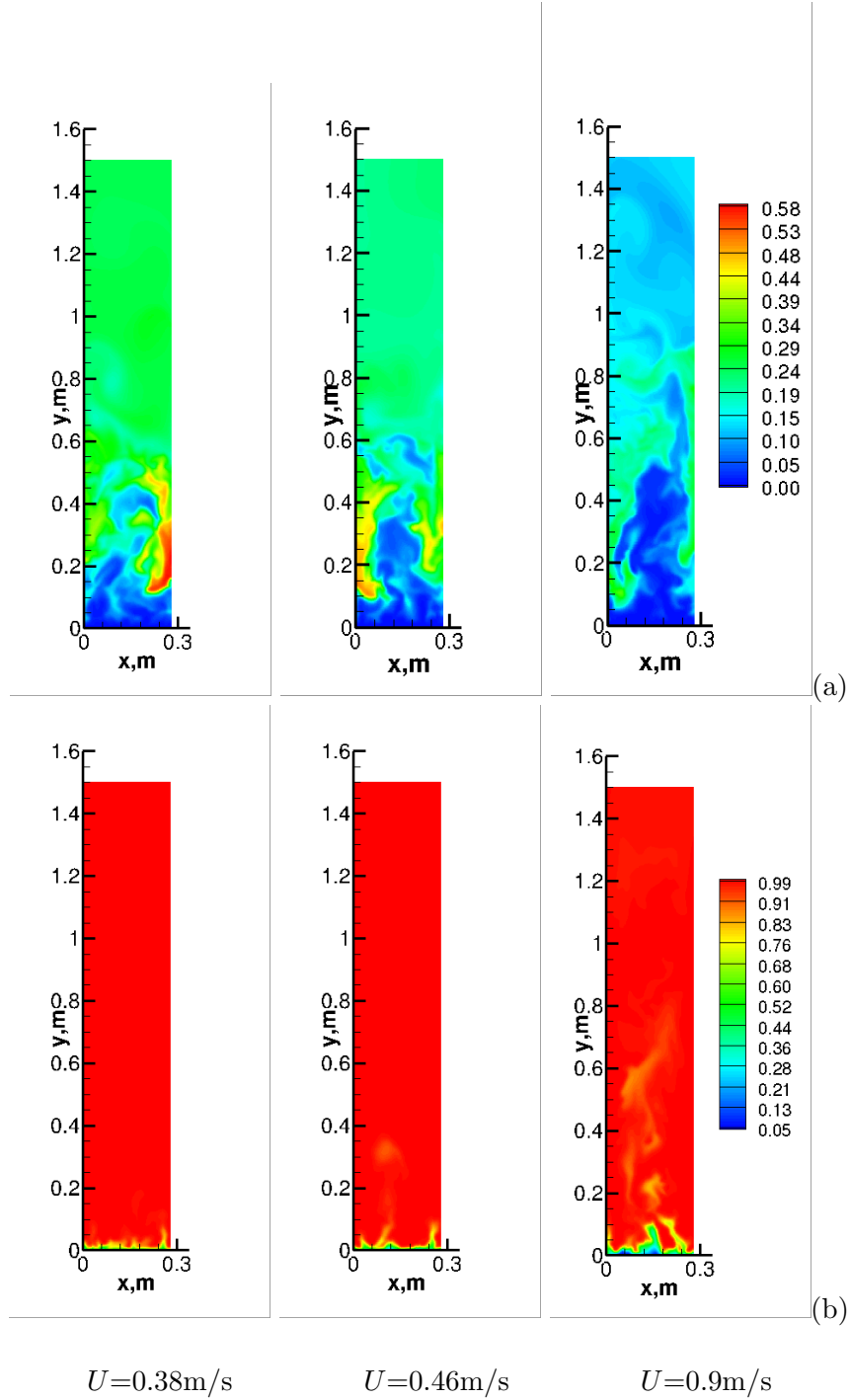


Figure 3.7: 2D-RANS: Mass fraction of  $CO$  calculated using unsteady E-E model at different inflow velocities  $U$ : Grid 1, (S-O),  $K=0.1$ ,  $e_{ss}=0.9$ , (a)  $T=1100$  K,  $t=20$  s, (b)  $T=1500$  K,  $t=40$  s.

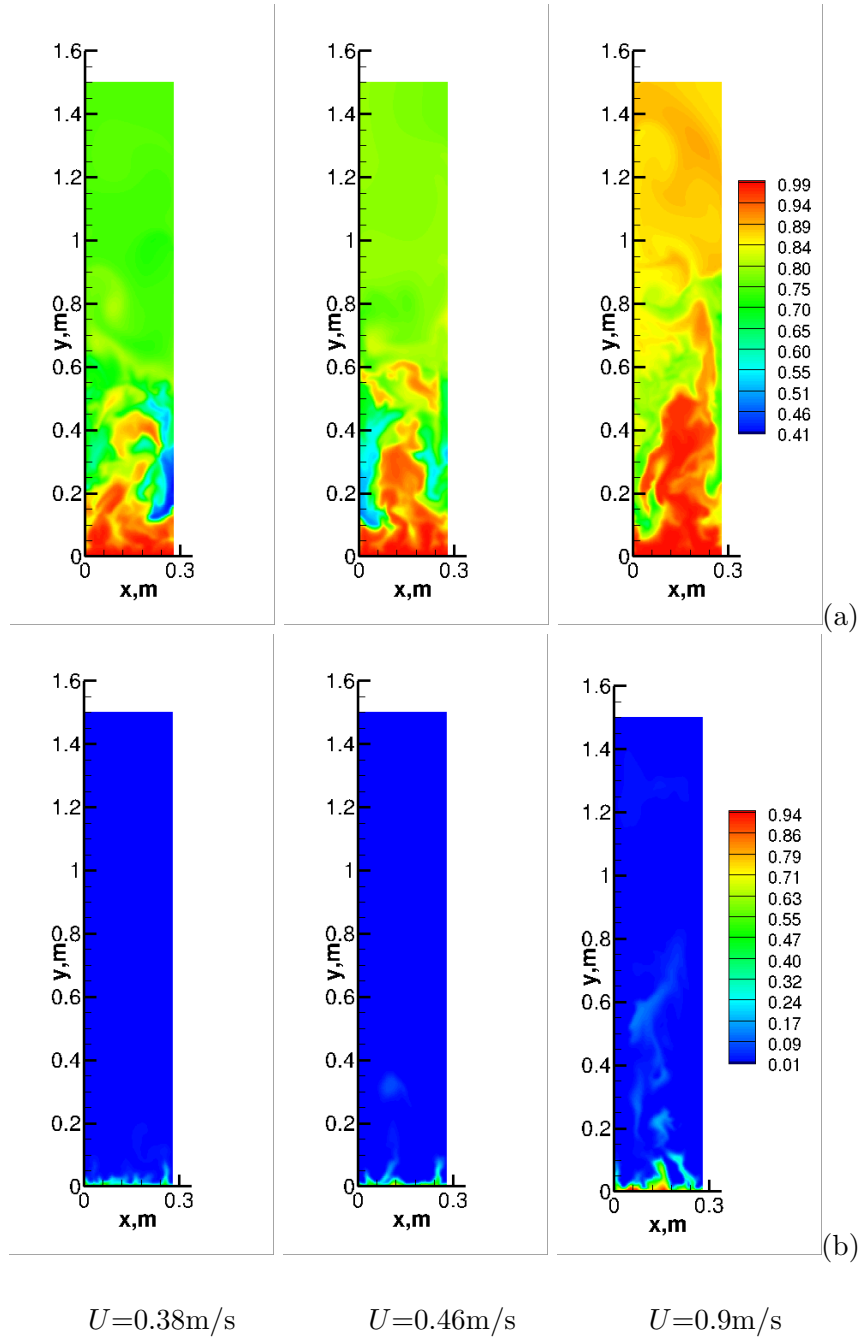


Figure 3.8: 2D-RANS: Mass fraction of  $CO_2$  calculated using unsteady E-E model at different inflow velocities  $U$ : Grid 1, (S-O),  $K=0.1$ ,  $e_{ss}=0.9$ , (a)  $T=1100$  K,  $t=20$  s, (b)  $T=1500$  K,  $t=40$  s.

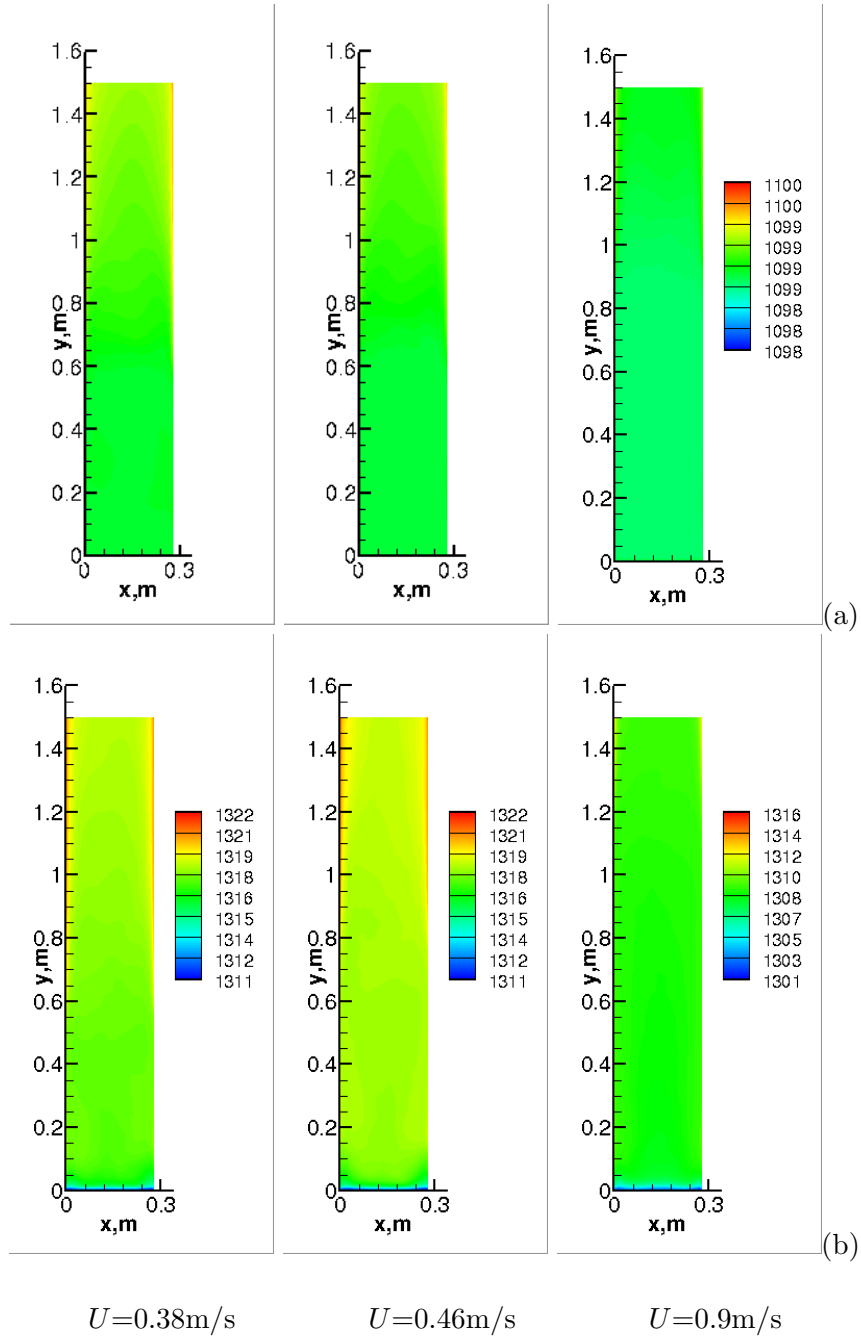


Figure 3.9: 2D-RANS: Time averaged temperature calculated using unsteady E-E model at different inflow velocities  $U$ : Grid 1, (S-O),  $K=0.1$ ,  $e_{ss}=0.9$ , (a)  $T=1100$  K, (b)  $T=1500$  K.

### 3.4 Conclusions

The influence of heterogeneous reactions has been investigated between gas phase and solid phase inside a fluidized bed using E-E model. Increase in the inflow velocity value causes the shift of fluidization regime to the entrainment of the solid phase, which does not guarantee a linear increase in the mass transfer rate between gas phase and solid phase. In addition, heterogeneous chemical reactions leads to significant changing of the fluidized regime due to local increase in the gas flow rate. This influence should be taken into account by design of chemical reactors with heterogeneous chemical reactions.

## Chapter 4

# Conclusions and Future Work

### 4.1 Conclusions

In the present project, the commercial computational fluid dynamics (CFD) software ANSYS Fluent 16.2 was validated by multi-phase modeling of fluidized beds. A gas-solid phase Eulerian-Eulerian based model is used to replicate the experimental of Taghipour[8]. The influence of model dimension (2D & 3D), flow regimes models (Laminar & turbulent), model parameters (restitution coefficient responsible for particle-particle interaction and specular coefficient responsible for wall-particle interaction) and computational grids were studied. The Syamlal-O'Brien and Gidaspow gas-solid drag models were tested. Based on the estimated model, the minimum fluidization velocity was predicted and different fluidization regimes (minimum fluidization, bubbling fluidization, and turbulent fluidization) were presented. In addition, the influence of heterogeneous reactions has been investigated between gas phase and solid phase inside a fluidized bed using E-E model. Following are the main conclusions that can be drawn from this study:

- The Euler-Euler model available by ANSYS Fluent 16.2 has been validated against experimental data[8] using 2D and 3D approaches.
- 3D and 2D approaches showed a deviation of time-averaged void fraction within [4.01-6.50]% and [4.48-13.08]%, respectively.
- We showed that 2D approach does not give a good agreement with experimental data. However, some combination of grid resolution, specular coefficient and restitution coefficients can give results close to experimental points.

- It was shown that the turbulence does not play a significant role inside the FB. However, the use of RANS model provides slightly better agreement with experimental data in comparison with results given by a Laminar model.
- Taking into account the Frictional Viscosity provides better agreement with experiment data.
- The specularity coefficient has more significant influence on the voidage distribution inside the bed in comparison to the restitution coefficient.
- Increase in the inflow velocity value does not guarantee a linear increase in the mass transfer rate between the solid phase and gaseous phase. This fact is explained by the shift of fluidization regime to the entrainment of the solid phase.
- Heterogeneous chemical reactions lead to significant modifications of the fluidization regime due to the increase in the gas flow rate. This effect should be considered by design of chemical reactors with heterogeneous chemical reactions, e.g. fluidized bed combustors, boilers and gasifiers.

## 4.2 Future Work

- Gasification modeling should be done using more adequate submodels for solid phase conversion taking into account particle shrinking and particle porosity tracking.
- Modeling of gasification with 3D approach and compare the numerical results from 2D and 3D models.
- Modeling of polydisperse particles in fluidized bed using population balance.
- Investigate the species transport in the solid phase.

# Bibliography

- [1] Christopher Higman and Maarten Van der Burgt. *Gasification*. Gulf professional publishing, 2011.
- [2] Petr A Nikrityuk and Bernd Meyer. *Gasification Processes: Modeling and Simulation*. John Wiley & Sons, 2014.
- [3] Inc Ansys. Ansys fluent theory guide. *Canonsburg, Pennsylvania*, page 794, 2011.
- [4] Wei Du, Xiaojun Bao, Jian Xu, and Weisheng Wei. Computational fluid dynamics (cfd) modeling of spouted bed: Assessment of drag coefficient correlations. *Chemical Engineering Science*, 61(5):1401–1420, 2006.
- [5] Wen-ching Yang. *Handbook of fluidization and fluid-particle systems*. CRC press, 2003.
- [6] Martin Gräbner. *Industrial coal gasification technologies covering baseline and high-ash coal*. John Wiley & Sons, 2014.
- [7] Alexander Stroh, Falah Alobaid, Max Thomas Hasenzahl, Jochen Hilz, Jochen Ströhle, and Bernd Epple. Comparison of three different cfd methods for dense fluidized beds and validation by a cold flow experiment. *Particuology*, 2016.
- [8] Fariborz Taghipour, Naoko Ellis, and Clayton Wong. Experimental and computational study of gas–solid fluidized bed hydrodynamics. *Chemical Engineering Science*, 60(24):6857–6867, 2005.
- [9] JM Link, LA Cuypers, NG Deen, and JAM Kuipers. Flow regimes in a spout–fluid bed: A combined experimental and simulation study. *Chemical Engineering Science*, 60(13):3425–3442, 2005.
- [10] Leina Hua, Junwu Wang, and Jinghai Li. Cfd simulation of solids residence time distribution in a cfb riser. *Chemical Engineering Science*, 117:264–282, 2014.

- [11] Kun Luo, Mingming Fang, Shiliang Yang, Ke Zhang, and Jianren Fan. Les–dem investigation of an internally circulating fluidized bed: effects of gas and solid properties. *Chemical engineering journal*, 228:583–595, 2013.
- [12] Shiliang Yang, Kun Luo, Jianren Fan, and Kefa Cen. Particle-scale investigation of the solid dispersion and residence properties in a 3-d spout-fluid bed. *AIChE Journal*, 60(8):2788–2804, 2014.
- [13] Zhongyi Deng, Rui Xiao, Baosheng Jin, He Huang, Laihong Shen, Qilei Song, and Qianjun Li. Computational fluid dynamics modeling of coal gasification in a pressurized spout-fluid bed. *Energy & Fuels*, 22(3):1560–1569, 2008.
- [14] Chanchal Loha, Himadri Chattopadhyay, and Pradip K Chatterjee. Three dimensional kinetic modeling of fluidized bed biomass gasification. *Chemical Engineering Science*, 109:53–64, 2014.
- [15] Jun Xie, Wenqi Zhong, and Baosheng Jin. Les-lagrangian modelling on gasification of combustible solid waste in a spouted bed. *The Canadian Journal of Chemical Engineering*, 92(7):1325–1333, 2014.
- [16] Andrew J Minchener. Coal gasification for advanced power generation. *Fuel*, 84(17):2222–2235, 2005.
- [17] D Vamvuka. Gasification of coal. *Energy exploration & exploitation*, 17(6): 515–581, 1999.
- [18] HD Schilling, B Bonn, and U Krauss. Coal gasification. 1976.
- [19] L Douglas Smoot and Philip J Smith. *Coal combustion and gasification*. Springer Science & Business Media, 2013.
- [20] Chanchal Loha, Himadri Chattopadhyay, and Pradip K Chatterjee. Euler-euler cfd modeling of fluidized bed: Influence of specularly coefficient on hydrodynamic behavior. *Particuology*, 11(6):673–680, 2013.
- [21] Chanchal Loha, Himadri Chattopadhyay, and Pradip K Chatterjee. Effect of coefficient of restitution in euler–euler cfd simulation of fluidized-bed hydrodynamics. *Particuology*, 15:170–177, 2014.
- [22] David G Schaeffer. Instability in the evolution equations describing incompressible granular flow. *Journal of differential equations*, 66(1):19–50, 1987.

- [23] Sascha Reiner Aldegonda Kersten. *Biomass gasification in circulating fluidized beds*. Twente University Press, 2002.
- [24] Kunii Daizo and Octave Levenspiel. *Fluidization engineering*. 1991.
- [25] Wolfgang Adlhoch, H Sato, J Wolff, and K Radtke. High-temperature winkler gasification of municipal solid waste. In *Gasification Technology Conference*, volume 8, 2000.
- [26] Hans Teggers and Karl A Theis. *The Rheinbraun High-temperature Winkler and Hydrogasification Processes*. International Gas Union, 1982.
- [27] Prabir Basu and Scott A Fraser. *Circulating fluidized bed boilers*. Springer, 1991.
- [28] David A Bell, Brian F Towler, Maohong Fan, et al. *Coal gasification and its applications*. William Andrew, 2010.
- [29] Ronald W Breault. Gasification processes old and new: a basic review of the major technologies. *Energies*, 3(2):216–240, 2010.
- [30] Emil Raymond Riegel. Kent and riegel’s handbook of industrial chemistry and biotechnology, vol. 1, 2007.
- [31] John R Grace and Fariborz Taghipour. Verification and validation of cfd models and dynamic similarity for fluidized beds. *Powder technology*, 139(2):99–110, 2004.
- [32] Naser Almohammed, Falah Alobaid, Michael Breuer, and Bernd Epple. A comparative study on the influence of the gas flow rate on the hydrodynamics of a gas–solid spouted fluidized bed using euler–euler and euler–lagrange/dem models. *Powder Technology*, 264:343–364, 2014.
- [33] Jack T Cornelissen, Fariborz Taghipour, Renaud Escudié, Naoko Ellis, and John R Grace. Cfd modelling of a liquid–solid fluidized bed. *Chemical Engineering Science*, 62(22):6334–6348, 2007.
- [34] Mehran Ehsani, Salman Movahedirad, and Shahrokh Shahhosseini. The effect of particle properties on the heat transfer characteristics of a liquid–solid fluidized bed heat exchanger. *International Journal of Thermal Sciences*, 102: 111–121, 2016.

- [35] Adnan Almuttahir and Fariborz Taghipour. Computational fluid dynamics of a circulating fluidized bed under various fluidization conditions. *Chemical Engineering Science*, 63(6):1696–1709, 2008.
- [36] A Bakshi, C Altantzis, RB Bates, and AF Ghoniem. Eulerian–eulerian simulation of dense solid–gas cylindrical fluidized beds: Impact of wall boundary condition and drag model on fluidization. *Powder Technology*, 277:47–62, 2015.
- [37] Mohsen Hamidipour, Jinwen Chen, and Faical Larachi. Cfd study on hydrodynamics in three-phase fluidized beds—application of turbulence models and experimental validation. *Chemical engineering science*, 78:167–180, 2012.
- [38] Tingwen Li, Aytakin Gel, Sreekanth Pannala, Mehrdad Shahnam, and Madhava Syamlal. Reprint of “cfd simulations of circulating fluidized bed risers, part i: Grid study”. *Powder Technology*, 265:2–12, 2014.
- [39] Kun Luo, Shiliang Yang, Junhua Tan, and Jianren Fan. Les-dem investigation of dense flow in circulating fluidized beds. *Procedia Engineering*, 102:1446–1455, 2015.
- [40] CR Müller, DJ Holland, AJ Sederman, SA Scott, JS Dennis, and LF Gladden. Granular temperature: comparison of magnetic resonance measurements with discrete element model simulations. *Powder Technology*, 184(2):241–253, 2008.
- [41] Christoph R Müller, Stuart A Scott, Daniel J Holland, Belinda C Clarke, Andrew J Sederman, John S Dennis, and Lynn F Gladden. Validation of a discrete element model using magnetic resonance measurements. *Particuology*, 7(4):297–306, 2009.
- [42] Thanh DB Nguyen, Myung Won Seo, Young-II Lim, Byung-Ho Song, and Sang-Done Kim. Cfd simulation with experiments in a dual circulating fluidized bed gasifier. *Computers & Chemical Engineering*, 36:48–56, 2012.
- [43] Madhava Syamlal and Thomas J O’Brien. Computer simulation of bubbles in a fluidized bed. In *AIChE Symp. Ser.*, volume 85, pages 22–31, 1989.
- [44] Dimitri Gidaspow. *Multiphase flow and fluidization: continuum and kinetic theory descriptions*. Academic press, 1994.
- [45] CY Wen and Y Yu. Mechanics of fluidization. In *Chem. Eng. Prog. Symp. Ser.*, volume 62, page 100, 2013.

- [46] Jinzhong Liu. *Particle and gas dynamics of high density circulating fluidized beds*. PhD thesis, University of British Columbia, 2001.
- [47] Baosheng Jin, Xiaofang Wang, Wenqi Zhong, He Tao, Bing Ren, and Rui Xiao. Modeling on high-flux circulating fluidized bed with geldart group b particles by kinetic theory of granular flow. *Energy & fuels*, 24(MAJUN):3159–3172, 2010.
- [48] Sabri Ergun. Fluid flow through packed columns. *Chem. Eng. Prog.*, 48:89–94, 1952.
- [49] Donald L Koch and Reghan J Hill. Inertial effects in suspension and porous-media flows. *Annual Review of Fluid Mechanics*, 33(1):619–647, 2001.
- [50] Tingwen Li, Sreekanth Pannala, and Mehrdad Shahnam. Reprint of” cfd simulations of circulating fluidized bed risers, part ii, evaluation of differences between 2d and 3d simulations. *Powder Technology*, 265:13–22, 2014.
- [51] R Di Felice. The voidage function for fluid-particle interaction systems. *International Journal of Multiphase Flow*, 20(1):153–159, 1994.
- [52] R Beetstra, MA Van der Hoef, and JAM Kuipers. Drag force of intermediate reynolds number flow past mono-and bidisperse arrays of spheres. *AIChE Journal*, 53(2):489–501, 2007.
- [53] Xiaogang Shi, Renjin Sun, Xingying Lan, Feng Liu, Yinghui Zhang, and Jinsen Gao. Cpdf simulation of solids residence time and back-mixing in cfb risers. *Powder Technology*, 271:16–25, 2015.
- [54] C Simonin and PL Viollet. Predictions of an oxygen droplet pulverization in a compressible subsonic coflowing hydrogen flow. *Numerical Methods for Multiphase Flows, FED91*, pages 65–82, 1990.
- [55] JO Hinze. *Turbulence*, mcgraw-hill publishing co. *New York, NY*, 1975.
- [56] Sebastian Zimmermann and Fariborz Taghipour. Cfd modeling of the hydrodynamics and reaction kinetics of fcc fluidized-bed reactors. *Industrial & engineering chemistry research*, 44(26):9818–9827, 2005.
- [57] Ling Zhou, Lingjie Zhang, Ling Bai, Weidong Shi, Wei Li, Chuan Wang, and Ramesh Agarwal. Experimental study and transient cfd/dem simulation in a fluidized bed based on different drag models. *RSC Advances*, 7(21):12764–12774, 2017.

- [58] Brian P Leonard. A stable and accurate convective modelling procedure based on quadratic upstream interpolation. *Computer methods in applied mechanics and engineering*, 19(1):59–98, 1979.
- [59] S Muzaferija, M Peric, P Sames, and T Schellin. A two-fluid navier-stokes solver to simulate water entry. In *Proceedings of the 22nd symposium on naval hydrodynamics, Washington, DC*, pages 277–289, 1998.
- [60] CKK Lun, S Br Savage, DJ Jeffrey, and N Chepurdiy. Kinetic theories for granular flow: inelastic particles in couette flow and slightly inelastic particles in a general flowfield. *Journal of fluid mechanics*, 140:223–256, 1984.
- [61] Paul C Johnson and Roy Jackson. Frictional–collisional constitutive relations for granular materials, with application to plane shearing. *Journal of fluid Mechanics*, 176:67–93, 1987.
- [62] Jianmin Ding and Dimitri Gidaspow. A bubbling fluidization model using kinetic theory of granular flow. *AIChE journal*, 36(4):523–538, 1990.
- [63] P. Nikrityuk, M. Ungarish, K. Eckert, and R. Grundmann. Spin-up of a liquid metal flow driven by a rotating magnetic field in a finite cylinder: A numerical and an analytical study. *Phys. Fluids*, 17:067101, 2005.
- [64] Derek Geldart. Types of gas fluidization. *Powder technology*, 7(5):285–292, 1973.
- [65] Jun Xie, Wenqi Zhong, Baosheng Jin, Yingjuan Shao, and Yaji Huang. Eulerian–lagrangian method for three-dimensional simulation of fluidized bed coal gasification. *Advanced Powder Technology*, 24(1):382–392, 2013.
- [66] Xiaofang Wang, Baosheng Jin, and Wenqi Zhong. Three-dimensional simulation of fluidized bed coal gasification. *Chemical Engineering and Processing: Process Intensification*, 48(2):695–705, 2009.
- [67] Qianjun Li, Mingyao Zhang, Wenqi Zhong, Xiaofang Wang, Rui Xiao, and Baosheng Jin. Simulation of coal gasification in a pressurized spout-fluid bed gasifier. *The Canadian Journal of Chemical Engineering*, 87(2):169–176, 2009.
- [68] Xiaoke Ku, Tian Li, and Terese Løvås. Cfd–dem simulation of biomass gasification with steam in a fluidized bed reactor. *Chemical Engineering Science*, 122:270–283, 2015.

- [69] CFD Multi-fluid. modeling of biomass gasification in polydisperse fluidized-bed gasifiers xue, q.; fox, ro. *Powder Technology*, 254:187–198, 2014.
- [70] Jun Xie, Wenqi Zhong, Baosheng Jin, Yingjuan Shao, and Hao Liu. Simulation on gasification of forestry residues in fluidized beds by eulerian–lagrangian approach. *Bioresource technology*, 121:36–46, 2012.